Title
QUENCHING OF METASTABLE RARE GASES BY CALCIUM ATOMS AND METAL CARBONYLS

Author
Hartman, Dennis C.

Publication Date
1979-10-01

Lawrence Berkeley Laboratory
UNIVERSITY OF CALIFORNIA

Materials & Molecular Research Division

QUENCHING OF METASTABLE RARE GASES BY CALCIUM ATOMS AND METAL CARBONYLS

Dennis C. Hartman
(Ph.D. thesis)

October 1979

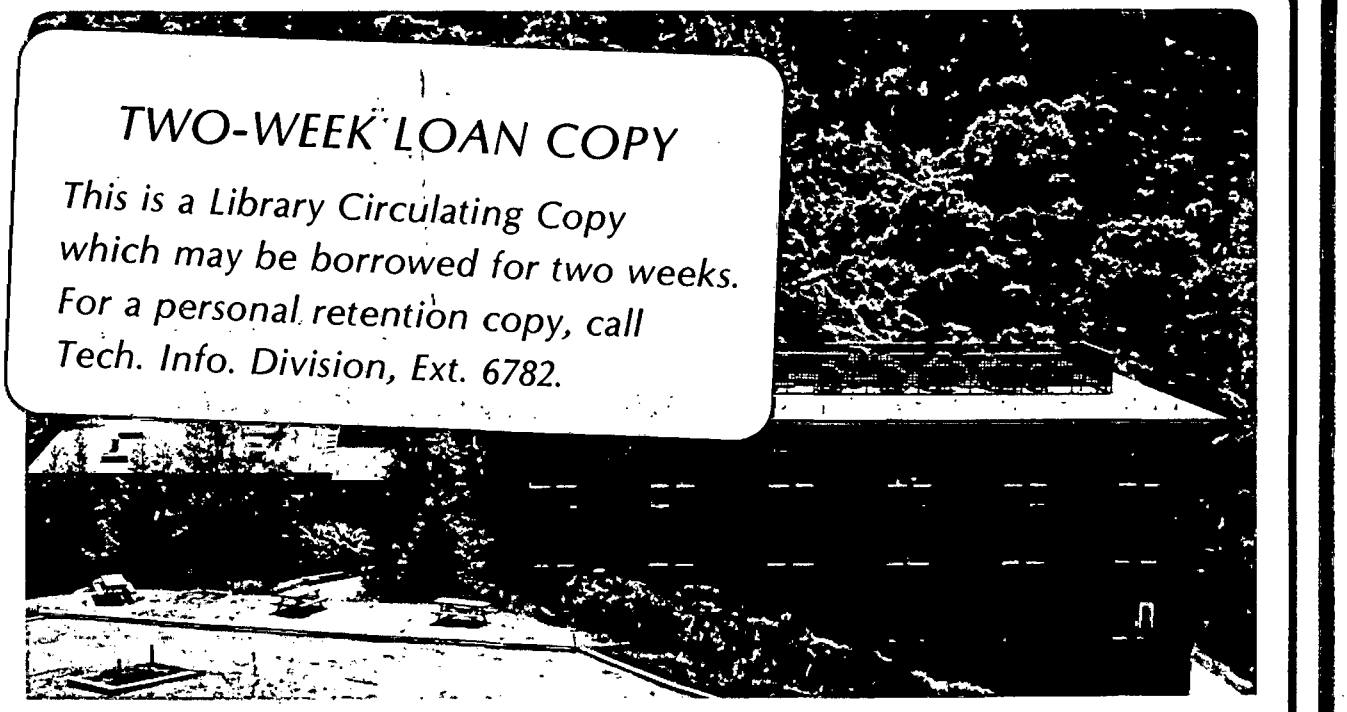

Prepared for the U.S. Department of Energy under Contract W-7405-ENG-48

DISCLAIMER

QUENCHING OF METASTABLE RARE GASES BY CALCIUM ATOMS AND METAL CARBONYLS

Dennis C. Hartman

Materials and Molecular Research Division
Lawrence Berkeley Laboratory
and
Department of Chemistry, University of California
Berkeley, California 94720

ABSTRACT

A flowing afterglow chemiluminescence apparatus was used to study three important processes, associative ionization, Penning ionization, and collisional dissociation. The metastable rare gases Ar^*, Ne^* and He^* were used as energy donors.

In the interaction of calcium atoms with metastable argon, excitive Penning and associative ionization reactions were observed, with emission from calcium ions formed in the $^2P^\circ_{3/2,1/2}$ states, and emission from the associative ion $CaAr^+$ formed in the A $^2\Pi$ state. The non-statistical populations in the $Ca^+(^2P^\circ_{3/2,1/2})$ states were explained as a propensity for conservation of both orbital and total electronic angular momentum. Thermal rate constants for formation of $Ca^+(^2P^\circ_{3/2})$, $Ca^+(^2P^\circ_{1/2})$ and $CaAr^+(^2\Pi)$ were measured to be 1.6×10^{-10}, 3.2×10^{-11} and 3.1×10^{-11} cm^3 $molecule^{-1}$ sec^{-1}, respectively. The branching ratio of excitive associative ionization (AI^*) to excitive Penning ionization (PI^*) was measured to be AI^* : PI^* = 14% : 86%. The rate constants and branching ratios are typical of many associative and

Penning reactions. The AI^* product, $CaAr^+$ ($^2\Pi$), was found to be highly vibrationally excited, ~1000 cm^{-1} below the dissociation limit.

$Ni(CO)_4$ and $Fe(CO)_5$ were found to dissociate during bimolecular collisions with Ar^*, Ne^* and He^*, yielding electronically excited free Ni and Fe atoms. The unique nature of the metal excitations is evidenced by the fact that the strongest Ni line in the $Ar^* + Ni(CO)_4$ interaction has not been previously reported in absorption or emission. Excitation of high-spin states of the metal atoms is strong. Relative populations and rates of the various metal states have been measured, along with absolute rates for $Ar^* + Fe(CO)_5$. A J-dependence is observed in the relative rates of formation of long-lived septet levels of iron, indicating J-changing collisions may be important. A statistical model, with restricted degrees of freedom in the exiting products, gives good agreement with experimental rate distributions. A two electron exchange model predicts the experimentally observed electron configurations quite well.

QUENCHING OF METASTABLE RARE GASES BY

CALCIUM ATOMS AND METAL CARBONYLS

Table of Contents

QUENCHING OF METASTABLE RARE GASES BY CALCIUM ATOMS AND METAL CARBONYLS

Dennis C. Hartman

Materials and Molecular Research Division
Lawrence Berkeley Laboratory
and
Department of Chemistry, University of California
Berkeley, California 94720

ABSTRACT

A flowing afterglow chemiluminescence apparatus was used to study three important processes, associative ionization, Penning ionization, and collisional dissociation. The metastable rare gases Ar^*, Ne^* and He^* were used as energy donors.

In the interaction of calcium atoms with metastable argon, excitive Penning and associative ionization reactions were observed, with emission from calcium ions formed in the $^2P°_{3/2,1/2}$ states, and emission from the associative ion $CaAr^+$ formed in the $A\ ^2\Pi$ state. The non-statistical populations in the $Ca^+(^2P°_{3/2,1/2})$ states were explained as a propensity for conservation of both orbital and total electronic angular momentum. Thermal rate constants for formation of $Ca^+(^2P°_{3/2})$, $Ca^+(^2P°_{1/2})$ and $CaAr^+(^2\Pi)$ were measured to be 1.6×10^{-10}, 3.2×10^{-11} and 3.1×10^{-11} cm^3 $molecule^{-1}$ sec^{-1}, respectively. The branching ratio of excitive associative ionization (AI^*) to excitive Penning ionization (PI^*) was measured to be AI^* : PI^* = 14% : 86%. The rate constants and branching ratios are typical of many associative and

Penning reactions. The AI^* product, $CaAr^+$ ($^2\Pi$), was found to be highly vibrationally excited, $\sim$1000 cm^{-1} below the dissociation limit.

$Ni(CO)_4$ and $Fe(CO)_5$ were found to dissociate during bimolecular collisions with Ar^*, Ne^* and He^*, yielding electronically excited free Ni and Fe atoms. The unique nature of the metal excitations is evidenced by the fact that the strongest Ni line in the $Ar^* + Ni(CO)_4$ interaction has not been previously reported in absorption or emission. Excitation of high-spin states of the metal atoms is strong. Relative populations and rates of the various metal states have been measured, along with absolute rates for $Ar^* + Fe(CO)_5$. A J-dependence is observed in the relative rates of formation of long-lived septet levels of iron, indicating J-changing collisions may be important. A statistical model, with restricted degrees of freedom in the exiting products, gives good agreement with experimental rate distributions. A two electron exchange model predicts the experimentally observed electron configurations quite well.

I. INTRODUCTION

The metastable rare gases are convenient energy carriers of reasonably high energy. For He, the metastables are the $2\,^1S$ and $2\,^3S$ states, forbidden to radiate due to the electric dipole selection rule that $S \nrightarrow S$ transitions are forbidden. In addition the $2\,^3S$ state is forbidden to radiate due to the $\Delta S = 0$ selection rule, valid for such a small atom. For Ne through Xe, the metastables are the $^3P_{2,0}$ states (of the lowest triplet manifold) which are forbidden to radiate due to the $\Delta J = 0, \pm 1$; $J = 0 \nleftrightarrow J = 0$ electric dipole selection rules. The energies of the metastable rare gases are listed in Table I.

Although all these metastables have radiative lifetimes greater than 1 sec, under typical 1 torr flow conditions, collisions with photons, atoms or molecules, electrons and walls are the ultimate controlling factor of the lifetimes of these metastable states. Lifetimes are in the 10 msec range, but this is plenty of time for a newly created metastable atom to flow and interact with another species. Metastable rare gases interact with many atomic and molecular species, and reviews by Fontijn[1] and Stedman and Setser[2] discuss the reaction chemistry. Table II lists the most common reactions that can occur. The possibility that there is no reaction at all is experimentally rare. The only species which exhibit no chemical interaction at all with a given metastable rare gas, according to Stedman and Setser, are the parent and lighter rare gas atoms.

Using the metastable rare gases Ar^*, Ne^* and He^*, three important collision processes were studied in this work, Penning ionization, associative ionization, and collisional dissociation. The reaction products and their internal energy distributions were detected by observing the chemiluminescence resulting from a reactive collision.

In Chapter II, the flowing afterglow chemiluminescence apparatus is discussed. Chapter III discusses the theory of Penning and associative ionization and the experimental results for the Ar^* + Ca system, in which chemiluminescence is observed from Penning and associative ions resulting from the reactions

$$Ar^* + Ca \rightarrow Ar + Ca^{+*} + e^-$$

and

$$Ar^* + Ca \rightarrow CaAr^{+*} + e^-.$$

Finally, Chapter IV discusses experimental results and plausible dissociation mechanisms for observed collisional dissociation of metal carbonyls by metastable rare gas atoms, e.g.

$$Ar^* + Fe(CO)_5 \rightarrow Ar + Fe^* + 5\,CO.$$

II. EXPERIMENTAL

The reactions of the metastable rare gases Ar^*, Ne^* and He^* were studied by observing the resulting chemiluminescence when these species interacted with a gaseous reagent. A block diagram of the flowing afterglow chemiluminescence apparatus is shown in Fig. 1.

Briefly, the metastable rare gas is created in a D.C. discharge and flows into the interaction region. The reagent of interest enters the interaction region through a gas inlet port, or if the reagent is a low vapor pressure liquid or a solid, via an oven heater. The interaction light is dispersed by a monochromator and detected by a photomultiplier tube. The output is fed to a multi-channel analyzer or a computer, and finally plotted as a spectrum of intensity versus wavelength. A more detailed discussion of the apparatus will follow.

The rare gases argon, neon and helium were purified by a variety of methods. The most annoying impurity in the tank Ar (Liquid Carbonic, > 99,998 %) was molecular nitrogen, because the C $^3\Pi_u$ state of nitrogen is resonant with $Ar^*(^3P_2)$ atoms and energy transfer is very efficient. N_2 can easily deplete the already low Ar^* concentration. A commercial titanium oven (R. D. Mathis inert gas purifier) was used to remove the residual N_2 from tank Ar with poor results. The beneficial removal of N_2 was outweighed by the constricting effect on the argon flow. A liquid nitrogen cooled molecular sieve trap was also tried, but the best results were obtained using no purification other than

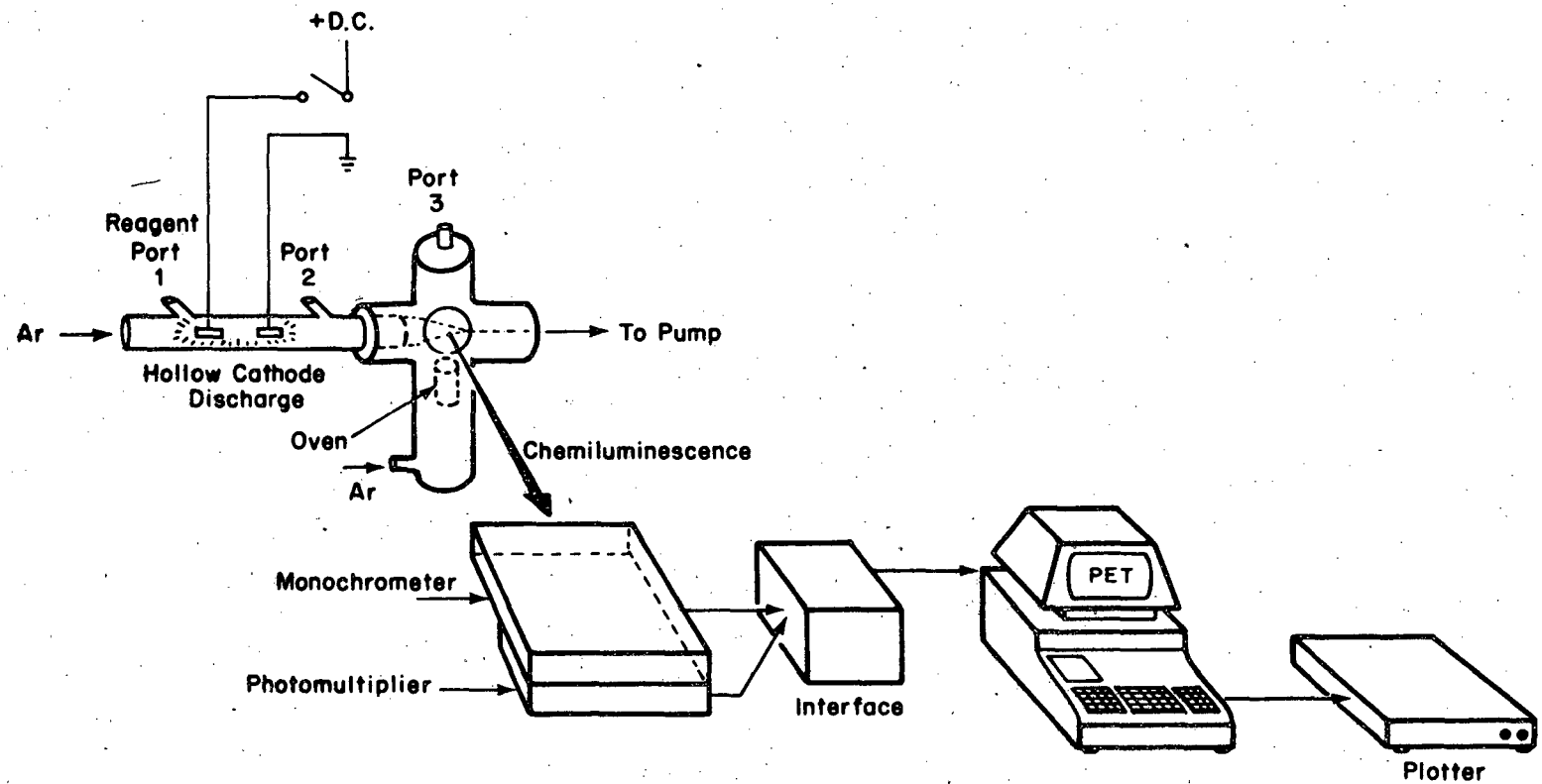

Fig. 1. A block diagram of the flowing afterglow chemiluminescence apparatus.

$CaSO_4$ desiccant to remove tank H_2O. Neon (Airco, 99.99 %) and helium (commercial grade of unknown purity) were purified through $CaSO_4$ and a liquid nitrogen cooled molecular sieve.

The source of the metastable rare gases was a flowing hollow cathode discharge tube patterned after Stedman and Setser.[2] Two cylindrical electrodes spaced ~1" apart were mounted in a 19 mm diameter pyrex tube. The electrodes were made of rolled 0.004" thick tantalum or stainless steel sheet with typical dimensions of 1" long by 3/8" diameter. The potential across the electrodes was 275 volts d.c. with the negative electrode downstream. The greatest metastable concentrations were obtained with neither electrode grounded. The discharge current was 1 ma.

The metastable rare gases created in the discharge flowed through a bent pyrex tube equipped with a Wood's horn to shield the interaction region from the discharge light. After flowing ~ 35 cm, they entered the interaction region, a stainless steel chamber with an interaction volume of ~8 cubic inches or ~ 130 cm^3. The chamber was equipped with six side-arms for flexible placement of windows, the discharge tube, reagent inlets, the pump foreline, pressure gauges, etc. The whole system was pumped by a Welch 1375 1000 ℓ/min mechanical pump with a vented exhaust.

The rare gas flow was measured to be 1400 μmole/sec which yields a flow velocity of 7.3×10^3 cm/sec. The Ar^* ($^3P_2$) concentration was estimated with atomic absorption of the 8115 Å Ar line (see Appendix A) to be $\sim 10^9 - 10^{10}$ atoms/cm^3. Ne^* ($^3P_2$) and He^* ($2\ ^3S$) concentrations

were not measured, but emission intensities when interacting with metal carbonyls were comparable (within a factor of 10). The cross-sections for the Ar^*, Ne^* and He^* reactions may be different, however, and comparable emission intensities may not necessarily mean comparable concentrations. Nevertheless, the concentrations of Ne^* and He^* are probably around the 10^9 - 10^{10} atoms/cm^3 range, also.

Gas pressures in the 0.1 μ - 1 torr range were measured with an MKS Baratron capacitance manometer, while pressures in the 1-5 torr range were measured with a mercury Macleod gauge. Both gauges read identically at 1 torr of pressure. The total rare gas pressure in the interaction region was typically in the 1 torr region.

A plot of [Ar^*] (as measured by 8115Å absorption) versus Ar pressure in the interaction region is shown in Fig. 2. At pressures much below 0.2 torr, the Ar discharge cannot be maintained, as is also the case for pressures much above 1.2 torr. The peak in [Ar^*] occurs around 0.9 torr, the pressure at which optimal hollow cathode discharge conditions exist.

The gaseous reagent of interest was metered through a stainless steel injection tube into the interaction region and collided with the metastable rare gas. Typical reagent gas pressures were 10-100 microns. Non-volatile liquids or solids were admitted from a stainless steel oven.

The oven heating unit consisted of a 0.010" thick tantalum sheet clamped between two concentric stainless steel rings. Each ring is hard-soldered to a water-cooled copper buss bar, the buss bars traveling through an aluminum flange and electrically isolated from the flange

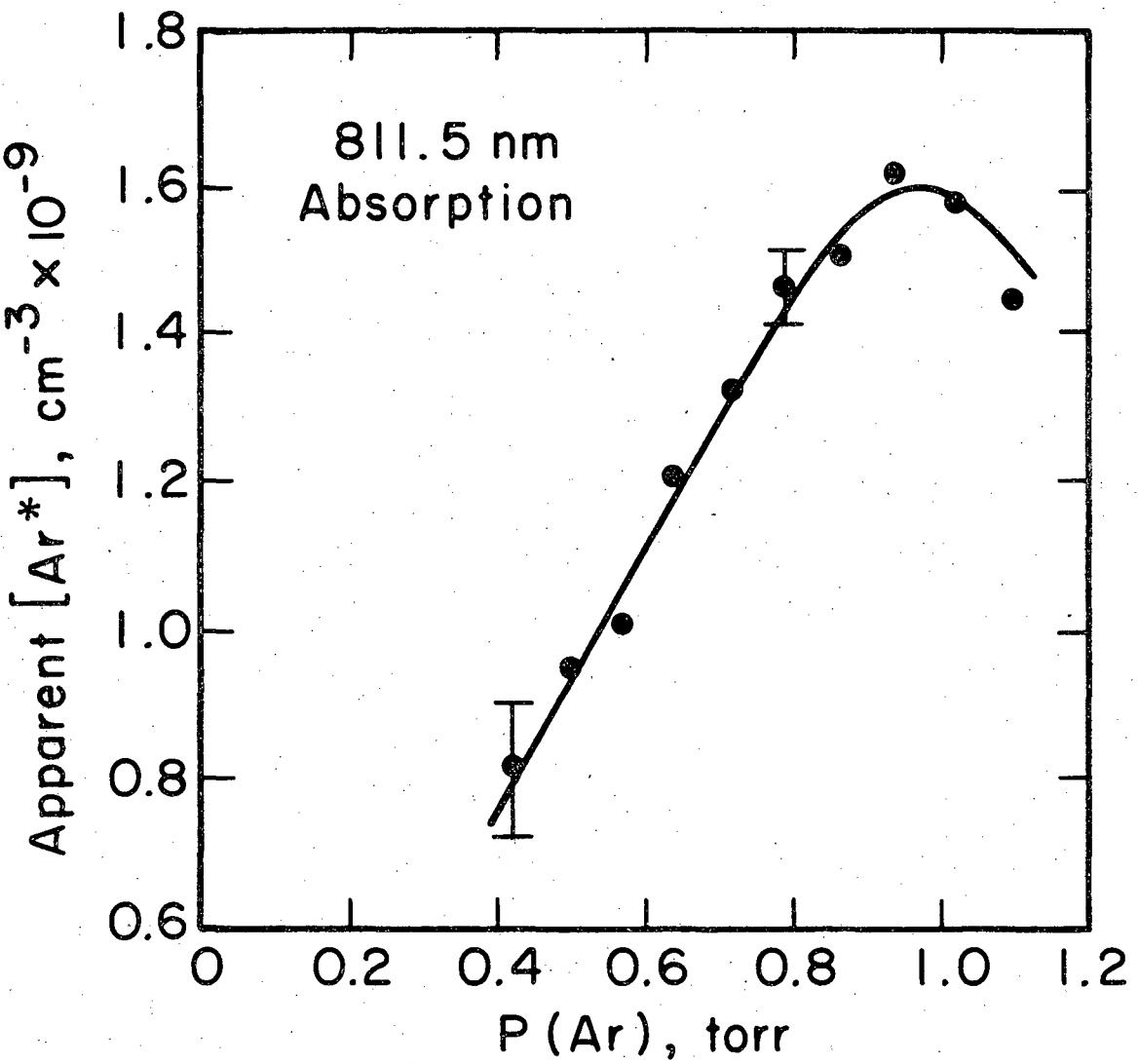

XBL 7910-12390

Fig. 2. $Ar^{*}\ ^{3}P_{2}$ concentration measurements via atomic absorption as a function of total Ar pressure in the interaction region.

with teflon spacers. The interaction chamber is bolted to the top of a larger stainless oven chamber (with a volume of ~ 3 liters) and the aluminum flange is bolted to the bottom. Thus the tantalum heater is directly below the interaction region, and the distance between the interaction region and the heater can be varied by adjusting the vertical buss bars through their Cajon "Ultra-Torr" connections to the aluminum flange. Typical distances between heater and interaction region were 5-10 cm.

The power source used to heat the tantulum was a large variable transformer (Superior Electric Powerstat) with a maximum secondary coil rating of 230 V. a.c. and 22 amps. Three turns of 4/0 welding cable are wound around the secondary coil (with ~240 turns) of the transformer, thus there is an eighty-fold voltage decrease across the ends of the cable when compared to the secondary voltage; but power in the transformer is conserved, thus the cable is capable of carrying enormous currents. The ends of the cable are clamped to the water-cooled buss bars with a shunt in series with the circuit, the shunt being calibrated to experience a 50 mV a.c. voltage drop across it when an a.c. current of 480 amps flows through it.

With the secondary transformer at 80 volts a.c. the current through the tantalum foil was typically 400 amps with a potential drop of ~ 1 volt a.c. The stainless steel oven rested inside the tantalum and was radiatively heated to temperatures as high as 1000 C, as measured by an optical pyrometer and a chromel-alumel thermocouple. Originally, thinner tantalum was used with poorer results. The resistance

of the tantalum is inversely proportional to its thickness; thus the thicker tantalum with less resistance dissipated more heat because of the power relation $P = V^2/R$.

Other methods of heating the oven proved less successful. Tantalum windings and commercial ceramic heaters (Mellon Co.) both suffered from the fact that high voltages ($\sim$120 volts a.c.) were required for heating. The oven was used primarily to vaporize calcium metal, and the $Ca + Ar^*$ mixture discharged and arced at these high voltages, destroying fuses, wires and creating unwanted light. Even though the ceramic heaters had no exposed wires at the oven top, violent discharges were still obtained. The low voltage heating was by far the superior method. No discharging was observed and electrons from thermionic emission experienced negligible accelerations, thus unwanted secondary excitations from these electrons, as well as any reaction electrons produced, were minimized.

Light from the interaction of the reagent of interest with the metastable rare gas traveled through a 2" diameter quartz window and entered the entrance slit of a high resolution Jovan-Yvon 1.5 m scanning holographic grating monochromator. Lenses aimed at focussing the light onto the slit did not appreciably raise the signal due to the diffuse nature of the interaction flame, and in most cases were not used. If intensities permitted, the monochromator had a resolution of better than 0.01 Å; and with large 1 mm slits the width of an atomic line (FWHM) was a respectable 2 Å.

Light leaving the exit slit hit the gallium arsenide photocathode of an RCA C31034 photomultiplier tube wired as in Fig. 3 for pulse-counting applications. The tube has an excellent response range from 2000-8500 Å. The potential of the photocathode was - 1600 volts and the anode was at ground potential. A mu-metal shield connected through a 9.1 MΩ resistor to the negative high voltage served as a Faraday cage, protecting the tube from stray electromagnetic waves. With the tube at room temperature the dark-count rate was ~ 3000 counts/sec. Cooling to dry-ice temperatures (- 57C) reduced the dark-count rate to less than 1 count/sec.

Pulses from the photomultiplier tube (widths of ~ 10 ns) were fed into a preamp counting head (Extranuclear Model 032-3). Here the pulses were discriminated, amplified and finally converted to low-going TTL pulses 0.2 μsec long suitable for scaling equipment. Two data collection systems were employed.

The first was a 4096 channel Fabri-Tek multichannel analyzer with an internal dwell ranging from 1 μsec/channel to 10 sec/channel and channel capacities of 130,000 counts. A spectrum was obtained by slewing the grating and simultaneously stepping the Fabri-Tek from channel to channel at a specified rate. Each channel thus had a fixed wavelength interval in which photons were counted, this interval determined by the monochromator slew speed (Å/min) and the Fabri-Tek dwell (sec/channel). The spectrum of intensity versus wavelength was plotted on an X-Y recorder. In addition, the Fabri-Tek was capable of direct channel readout of any interesting emission feature.

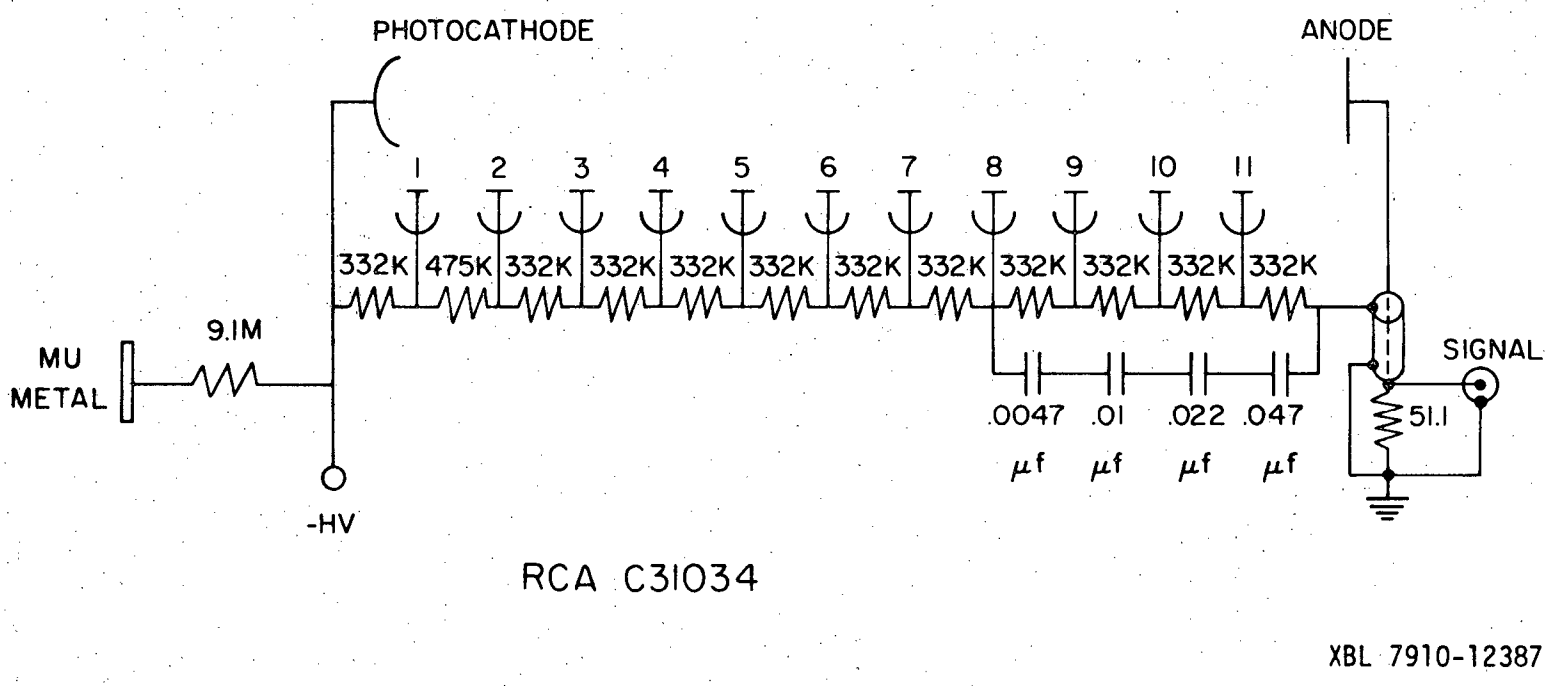

Fig. 3. Dynode chain wiring diagram of the pulse-counting photomultiplier tube.

The second was a computer interface built by the chemistry department electronic shop. The monochromator had two useful features, a control module and an optical encoder. By sending pulses to appropriate pins on the computer plug of the control module, one could start or stop the grating stepping motor, open or close the stepping motor clutch and change the stepping motor direction. The optical encoder was coupled directly to the wavelength drive and provided an extremely accurate 100 pulses/Å.

An Intel 8253 programmable interval timer was made part of the memory of a Commodore 8K PET computer. The 8253 is a set of 3 independent 16-bit counters with a maxiumum data acquisition rate of 2 MHZ. Two of the counters were used, one to count optical encoder pulses and the other to count photons.

A spectrum was obtained in the following manner. The scan speed was set in the normal manner with the push-button controls on the control module. The following scan parameters were input into the PET:

(1) Å/channel

(2) number of channels

(3) scan direction (red or blue)

(4) number of scans

The PET zeroed the counters and commanded the monochromator to scan in the specified direction. When the accumulated encoder pulses reached the value set by (1) above, the PET:

(1) Simultaneously commanded the stepping motor to stop and the clutch to open.

(2) Read the photon counter and dumped the result into memory.

(3) Displayed the photon counts and a histogram on the screen.

(4) Repeated the whole process for the desired number of channels.

When one scan was done, the PET reversed the scan direction and repetitively scanned back and forth over the desired wavelength region, adding the photon counts to those already accumulated. This method of data acquisition was particularly useful for weak emission systems, in that it afforded long counting times and changes in emission intensity were averaged out because in general they occur on a longer time scale than that for a single scan. The clutch is crucial to the system, because it was found that without it the stepping motor momentum caused the grating to overshoot its desired stopping point after the stepping motor was stopped.

Finally, the spectrum was plotted on a Tektronix 4662 plotter connected to the PET through an IEEE buss connection.

The relative spectral response of the spectrometer (J-Y monochromator + cooled RCA C31034 photomultiplier tube) was obtained from 3500 Å to 8200 Å by using a tungsten-filament incandescent lamp. A lamp spectrum was taken, with the brightness kept constant by a photodiode connected to the lamp power supply through a feedback loop. A calibrated 6500 Å optical pyrometer gave a brightness temperature T_b = 1889 ± 5 K both before and after the scan. Appropriate filters were used to avoid interference from second order light.

The relative spectral intensity of a blackbody radiator is given by St. John[3] as

$$I(\lambda, T) = \frac{C_1}{\lambda^5} \frac{1}{\exp(hc/\lambda kT) - 1}$$

where I is power per unit area per unit wavelength, T is the cavity temperature, h is Planck's constant, c is the speed of light, k is Boltzmann's constant and C_1 is a relative proportionality constant.

As discussed by Rutgers and De Vos,[4] the color temperature of a radiator (in this case a hot tungsten filament) is the temperature of a blackbody having the same spectral distribution of energy in the visible region of the spectrum. Using their table one converts the measured brightness temperature (1889 K) to a color temperature of 2070 ± 5 K. Substituting T(color) for T, $I(\lambda)$ for the tungsten filament lamp can be calculated with the above formula, the applicable ranges being 1400 to 3200 K and 3500 to 10,000 Å for use of the formula. The relative efficiency, E, of the spectrometer can be calculated by the formula

$$E(\lambda) = \frac{\text{observed lamp intensity at } \lambda}{\text{theoretical lamp intensity at } \lambda} .$$

A plot of relative spectral response of the spectrometer from 3500 Å to 8200 Å is shown in Fig. 4.

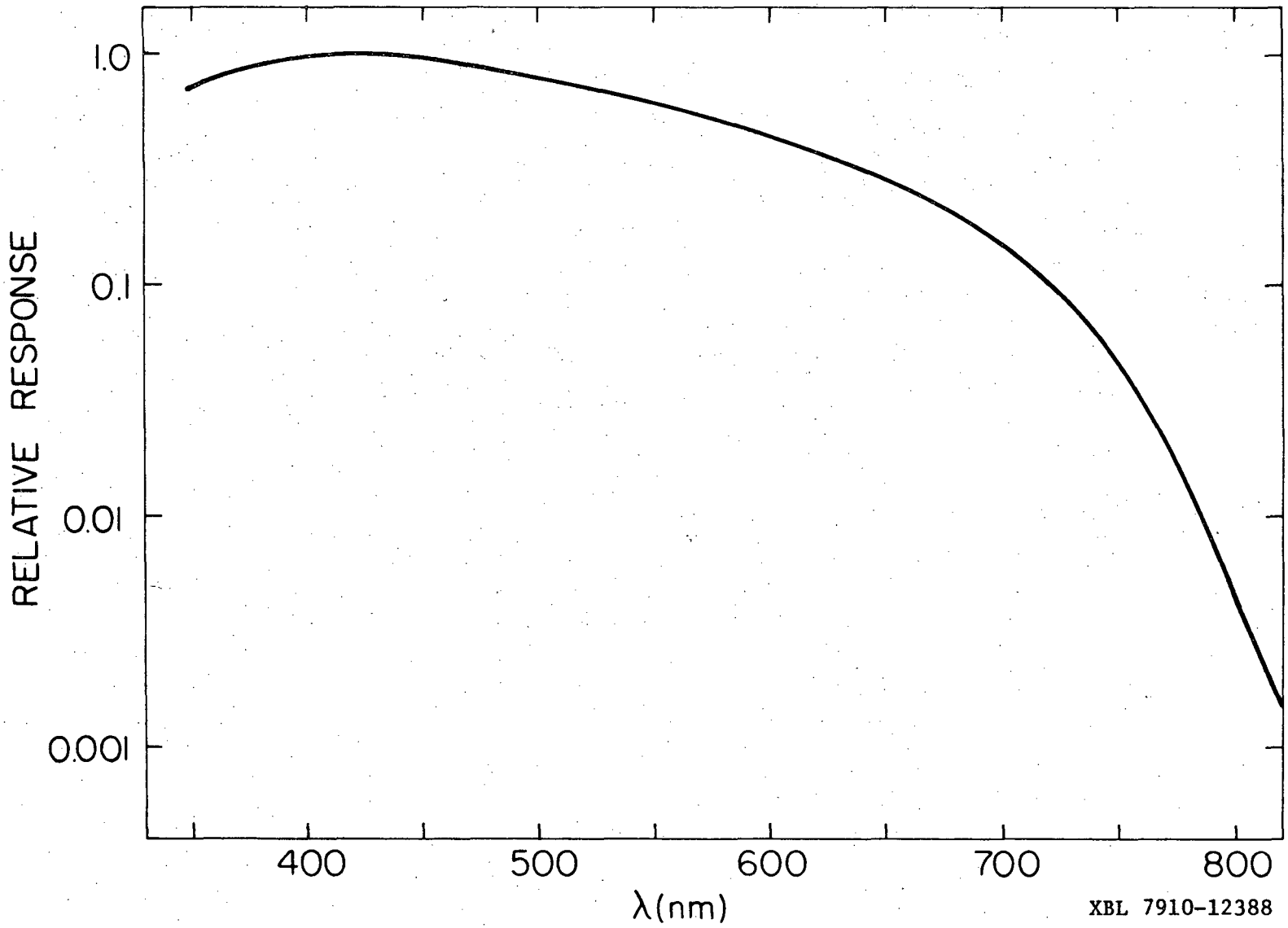

Fig. 4. Relative response function for the Jovan-Yvon 1.5 meter monochromator + dry-ice cooled RCA C31034 photomultiplier tube.

III. CHEMILUMINESCENT ASSOCIATIVE AND PENNING IONIZATION

A. Introduction

Associative ionization (AI)

$$A^* + B \rightarrow (AB)^* \rightarrow AB^+ + e^-$$

and Penning ionization (PI)

$$A^* + B \rightarrow (AB)^* \rightarrow A + B^+ + e^-$$

are important ionization mechanisms under plasma, discharge and combustion conditions. As an elementary process, AI is extraordinary because of the enormous difference in reduced mass between reactants and products.

AI is closely related to radiative association (RA)

$$A^* + B \rightarrow (AB)^* \rightarrow AB + h\nu,$$

although there is an important kinetic difference between the two processes. In RA, the collision complex $(AB)^*$ has a typical lifetime before dissociation of 10^{-13} sec, whereas its radiative lifetime is typically $\geqslant 10^{-8}$ sec. Thus the formation of a stable, bound AB molecule occurs with an efficiency no greater than 10^{-5}. Many associative ionization reactions proceed with collision efficiencies between 0.01 and 0.1. Thus, if energetics permit, ejection of an electron will dominate over ejection of a photon.

The majority of AI and PI reactions studied, and probably the majority occurring in nature, involve an electronically excited A atom or molecule with a ground state B atom or molecule. For exothermic reactions, typical rate constants are in the range of 10^{-9} to 10^{-11} cm^3 $molecule^{-1}$ sec^{-1} at room temperature.

Historically, AI was known before PI and was discovered between 1926 and 1928. Mohler, Foote, and Chenault[5] found that Cs vapor could be ionized with light of less energy than the atomic ionization potential. The ionization occurs at wavelengths corresponding to the principal series in Cs. Franck[6] attributed the experimental observations to the process

$$Cs^*(mP) + Cs \rightarrow Cs_2^+ + e^-$$

where the extra energy needed to ionize the gas comes from the formation of a diatomic bond. Arnot and Milligan[7] were the first to mass spectrometrically observe an AI product, Hg_2^+, formed by Hg^* + Hg. Hornbeck and Molnar[8] have done extensive studies on AI reactions between noble gas atoms, studying the appearance potentials of He_2^+, Ne_2^+ and Ar_2^+. The PI process was first described by Kruithoff and Penning[9] in 1937.

AI and PI reactions are the most important ionization mechanisms in many systems. Ionization due to metastable He($2\,^1S$, $2\,^3S$) atoms must certainly occur in stellar environments, e.g. $He^*(2\,^3S) + H \rightarrow He + H^+ + e^-$, although its importance is unknown. The primary chemi-ion in hydrocarbon-oxygen flames is CHO^+ from the AI reaction[10]

$$CH + O \rightarrow CHO^+ + e^-.$$

This reaction can occur with CH and O in the ground state, although in general this is a rarity due to the fact that the ionization potentials exceed the bond energies for most compounds. Another set of reactions[11] that proceed with ground state species are:

$$U + O \rightarrow UO^+ + e^- \qquad \Delta H = -2.0 \text{ eV}$$

$$U + O_2 \rightarrow UO_2^+ + e^- \qquad \Delta H = -4.1 \text{ eV};$$

these reactions possibly having use in uranium purification and isotope enrichment.

Most of the early studies of PI and AI involved flow experiments. In recent years, there have been many single collision experiments involving molecular beams, particularly involving metastable rare gas atoms as one of the collision partners. Haberland, Lee and Siska[12] have a recent comprehensive review in this area. Beam scattering studies are notable for their ability to determine the interaction potentials between colliding pairs, and in some cases can determine ionization transition rates, ionization cross-sections, and branching ratios between competing channels. Beam studies do not measure AI internal energy distributions, because only product angular and velocity distributions are detected.

Electron spectroscopy methods can yield branching ratios of various PI products and some information on the internal energy distribution of the AI product. The AI information is generally in the high energy tail of the electron distribution, and yields the vibrational energy below the dissociation limit in the AI product. Niehaus[13] reviews the method as applied to Penning ionization.

The experimental approach in this work has been to study the chemiluminescence of product PI and AI ions in an argon flowing afterglow. The resulting electronic spectrum can in principle give detailed information on the product branching ratios, rate constants and internal

energy distributions.

Thus, PI and AI are important elementary reactions, and more studies of these processes are needed. In particular, detailed studies of the internal energy distribution in the AI product, i.e., the electronic, vibrational, rotational and translational states that are produced, are needed. The work in this laboratory has started to make strides in this direction.

B. Associative and Penning Ionization Theory

This section will cover some of the qualitative aspects of PI and AI, a brief discussion of the calculation of transition rates, and finally the classical theory of PI and AI for atoms.

Associative ionization

$$A^* + B \rightarrow AB^+ + e^- \qquad \text{(AI)}$$

and Penning ionization

$$A^* + B \rightarrow A + B^+ + e^- \qquad \text{(PI)}$$

are very similar processes, AI producing the product in the bound portion of the AB^+ potential and PI producing the product in the unbound portion of the AB^+ potential.

Figure 5(a) depicts a set of potential curves favorable for AI. The energy of A^* is greater than the ionization potential of B. The colliding reactants initially ride on the AB^* potential surface with total energy E_T. In their simplest description, both AI and PI can be considered Franck-Condon type autoionization processes, where the

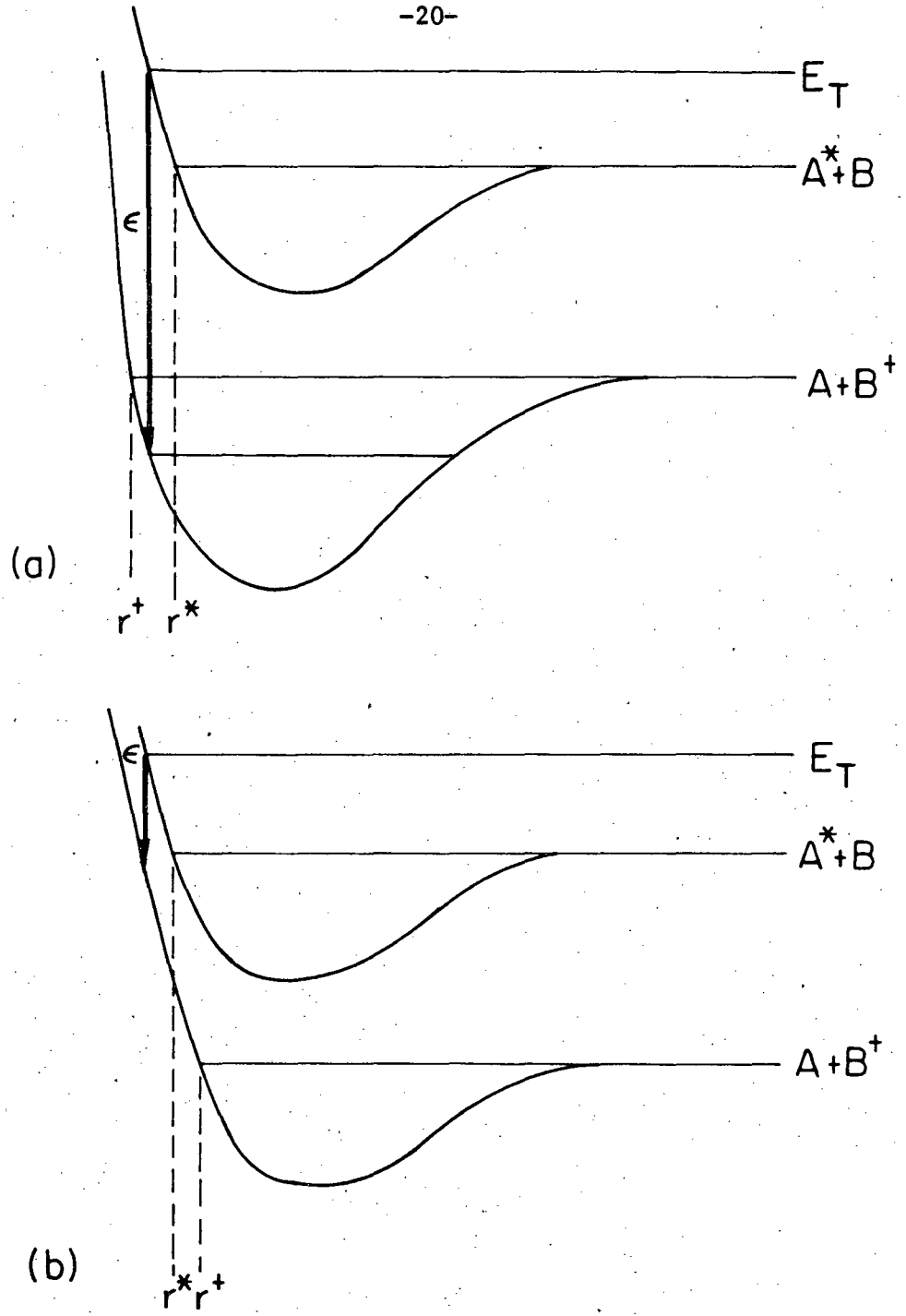

XBL 7910-12399

Fig. 5. Typical sets of ionization potential curves. E_T is the total energy, ϵ is the ejected electron energy, and r^+ and r^* are the classical turning points at zero kinetic energy. (a) Curves favorable for associative ionization with $r^+ < r^*$, (b) Curves unfavorable for associative ionization, with $r^+ > r^*$.

maximum probability for a transition from the neutral to the ionic state occurs around the classical turning point and the transition is faster than the relative motion of A^* and B, so that there is no change in internuclear distance. The arrow shows a Franck-Condon transition to a bound state of AB^+, with ε being the length of the arrow and equal to the kinetic energy of the ejected electron. r^* and r^+ are the classical turning points for zero kinetic energy particles for the neutral and ionic atom pairs. With $r^+ < r^*$, the greater the difference in these two quantities, the greater is the number of bound levels of AB^+ that can be formed. Hence AI becomes more favored.

It can also be seen that increasing E_T (i.e. increasing the relative translational energy of the colliding pair) favors PI over AI because more of the unbound portion of the AB^+ potential becomes sampled.

Figure 5(b) depicts a set of potential curves where $r^+ > r^*$. If transitions only occurred at the classical turning points, AI would be completely impossible. As we will see shortly, the transition rate is given by $\Gamma(r)/\hbar$, where $\Gamma(r)$ is the autoionization width. $\Gamma(r)$ monotonically decreases with increasing r, and $\Gamma(r) \to 0$ as $r \to \infty$; but for reasonable values of r there is always a finite probability for a transition to the ionic state. Nevertheless, with $r^+ > r^*$, AI should be extremely unfavorable.

Thus r^* and r^+ are very important parameters in determining the branching ratios for AI and PI. With one less electron than AB^* to screen the repulsion between the two nuclei, the repulsive wall of AB^+ should set in at least as rapidly as that for AB^*. Thus r^+ should be pretty

much equal to r^* and turning point transitions for the most part should lead to PI. The ionic curve is expected to have a greater long-range potential than the neutral, due to the ion-induced dipole interaction with a potential going as r^{-4}.

As mentioned before, $\Gamma(r)$ (units of energy) is the autoionization width and $\Gamma(r)/\hbar$ (units of sec^{-1}) is the rate of leakage from the discrete A^*-B state into the continuum state $AB^+ + e^-$ at a particular internuclear distance r. How is $\Gamma(r)$ calculated?

W. H. Miller and coworkers have been instrumental to the theoretical understanding of Penning and associative ionization reactions. As discussed by Miller[14], $\Gamma(r)$ can be described by a golden rule formula

$$\Gamma(r) = 2\pi\rho \; |< \phi_i | H_{el} - E | \phi_j >|^2, \qquad (1)$$

where ρ is the density of final continuum states, E is the electronic energy of the discrete state, H_{el} is the electronic Hamiltonian (kinetic energy of all electrons + Coulomb interactions among all electrons and nuclei), $|\phi_i>$ is the initial discrete state and $|\phi_j>$ is the final continuum state. Bellum and George[15] have recently presented a quantum mechanical theory of collisional ionization in the presence of intense laser radiation. In the field-free case (laser off), the only major coupling between initial and final states is the Coulomb interaction

$$V^c_{\varepsilon,r}(r) = < \phi_\varepsilon | H_{el} | \phi_d > \qquad (2)$$

where ϕ_d is the initial bound (in the sense that the e^- is bound) state and ϕ_ε is the final continuum state. Figure 1 of Ref. 15 shows that $V^c_{\varepsilon,d}(r)$ attains appreciable magnitude near the classical turning point

for heavy particle motion and rapidly goes to zero as $r \to \infty$.

Most studies of PI and AI result from the interaction of an electronically excited atom with a ground state atom or molecule. Many studies have been done using the metastable rare gases. Here the Coulomb interactions can be easily seen. The metastable rare gas has an orbital vacancy, a p-shell vacancy for Ne^*, Ar^*, Kr^* and Xe^*, all with the configuration $np^5(n+1)s^1$; and an s-shell vacancy for He^*, with a configuration $1s^1 2s^1$. When these metastable rare gases interact with an atom or molecule, an electron on the atom or molecule experiences a Coulombic force due to the orbital hole and is eventually stripped away causing ionization. The rare gas negative ions are not bound, and a strong Coulomb repulsion quickly ejects the outer s electron. This two-step process of an electron filling an orbital vacancy and the negative ion formed ejecting an electron should depend strongly on r, occurring only at distances where the potential on the transferred electron is greater than the ionization potential of the reactant species.

Recently Hickman, Isaacson and Miller[16] have used Feshbach projection operators to calculate autoionization widths. The details of the method are involved, but the dominant term in the Hamiltonian is still the Coulombic interaction. Calculations of $\Gamma(r)$ for the He ($2\,^3S$—H) system with this method are compared to golden rule calculations of $\Gamma(r)$ by Miller, Slocomb and Schaefer.[17] The agreement between the two calculations is reasonable. It is also worth pointing out that $\Gamma(r)$ changes by four orders of magnitude over just a 3 Å internuclear distance.

Thus, with a knowledge of the potential curves and wavefunctions for the initial and final states, $\Gamma(r)$ can be calculated. Calculating $\Gamma(r)$ is not trivial, and accurate calculations have only been done on systems with small numbers of particles. Advances in computer speed should eventually move these calculations of $\Gamma(r)$ out to the heavier particle regime.

Assume that we are armed with three quantities, $\Gamma(r)$, the neutral potential $V_o(r)$ which dissociates into $A^* + B$, and the ionic potential $V_+(r)$ which dissociates into $A + B^+$. How do we go about getting reaction cross sections and electron distributions for PI and AI? Miller's[18] classical theory of PI and AI for atoms has been extensively used, and provides an intuitive description of the salient features of the reaction mechanism and product states. The classical theory will be outlined below.

Since $V_o(r)$ and $V_+(r)$ are assumed to be spherically symmetric, the radial motion problem can be solved for each value of orbital angular momentum $\ell\hbar$. One wishes to find the probability $P_\ell(r)$ such that $P_\ell(r)dr$ is the probability that leakage into the continuum has occurred between the internuclear distances r and r + dr.

On the inward phase of the trajectory

$$P_\ell^{in}(r)dr = \left[1 - \int_r^\infty dr' P_\ell^{in}(r')\right]\left(\frac{\Gamma(r)}{\hbar}\right)\left(\frac{dr}{v_\ell(r)}\right). \qquad (3)$$

The quantity in brackets is called the survival factor, and is the probability that leakage has not already occurred over the region of ∞ to r. The next term is the leakage rate at r, and the final term is the time

spent in the interval $(r, r+dr)$; $V_\ell(r)$ is the radial velocity given by

$$V_\ell(r) = \left(\frac{2[E - V_o(r) - (\hbar^2 \ell^2 / 2\mu r^2)]^{1/2}}{\mu} \right)^{1/2} \tag{4}$$

where μ is the reduced mass of the system.

Equation (3) is solved to yield

$$P_\ell^{in}(r) = \frac{\Gamma(r)}{\hbar V_\ell(r)} \exp\left(- \int_r^\infty dr' \frac{\Gamma(r')}{\hbar V_\ell(r')} \right). \tag{5}$$

Also

$$\int_{r_o}^\infty dr \; P_\ell^{in}(r) = 1 - \exp\left(- \int_{r_o}^\infty dr \; \frac{\Gamma(r)}{\hbar V_\ell(r)} \right) \tag{6}$$

where r_o is the classical turning point. Thus equation (6) gives the probability that leakage has occurred on the transversal of $r = \infty$ to $r = r_o$.

For the outward part of the trajectory

$$P_\ell^{out}(r)\, dr = \left[1 - \int_{r_o}^\infty dr' P_\ell^{in}(r') - \int_{r_o}^r dr' P_\ell^{out}(r') \right] \left(\frac{\Gamma(r)}{\hbar} \right) \left(\frac{dr}{V_\ell(r)} \right) \tag{7}$$

where now the quantity in brackets is the probability that leakage has not occurred on the inward path from $r = \infty$ to $r = r_o$ or on the outward path from $r = r_o$ to $r = r$. Solution of equation (7) gives

$$P_\ell^{out}(r) = \frac{\Gamma(r)}{\hbar V_\ell(r)} \exp\left(- \int_{r_o}^\infty dr' \frac{\Gamma(r')}{\hbar V_\ell(r')} - \int_{r_o}^r dr' \frac{\Gamma(r')}{\hbar V_\ell(r')} \right). \tag{8}$$

Also

$$\int_{r_o}^{\infty} dr\ P_\ell^{out}(r) = \exp\left(-\int_{r_o}^{\infty} dr\ \frac{\Gamma(r)}{\hbar V_\ell(r)}\right)\left[1 - \exp\left(-\int_{r_o}^{\infty} dr\ \frac{\Gamma(r)}{\hbar V_\ell(r)}\right)\right]. \tag{9}$$

Now the probability density $P_\ell(r)$,

$$P_\ell(r) \equiv P_\ell^{in}(r) + P_\ell^{out}(r) \tag{10}$$

is the probability that leakage occurs at r on the inward or outward part of the collision. The probability of a transition during the entire collision, P_ℓ, is given by

$$P_\ell \equiv \int_{r_o}^{\infty} dr\ P_\ell(r). \tag{11}$$

Substituting equations (6), (9), and (10) into (11) yields

$$P_\ell = 1 - \exp\left(-2\int_{r_o}^{\infty} dr\ \frac{\Gamma(r)}{\hbar V_\ell(r)}\right). \tag{12}$$

The total cross section is given by

$$\sigma_o^{tot}(E) = (\pi/k_o^2)\sum_\ell (2\ell + 1)\ P_\ell \tag{13}$$

where $k_o = \{2u[E - V_o(\infty)]/\hbar^2\}^{1/2}$. The form of equation (13) requires a little explanation. The classical impact parameter is $b(\ell) = \ell/k_o$, and the classical orbital angular momentum of a particle with impact parameter b is $bk_o\hbar$. Particles which pass through an inner and outer ring with radii $b(\ell)$ and $b(\ell+1)$ will have angular momenta $\ell\hbar$ and $(\ell+1)\hbar$ respectively. The probability of hitting the ring is proportional to its area A, which is

$$A = \pi[b(\ell+1)^2 - b(\ell)^2] = \frac{\pi}{k_o^2}[(\ell+1)^2 - \ell^2]$$

$$A = \frac{\pi}{k_o^2}(2\ell+1) . \tag{14}$$

Thus, the total cross-section in equation (13) is seen as the sum over all partial waves ℓ of the probability of being in a certain ring between $b(\ell)$ and $b(\ell+1)$. The $2\ell + 1$ factor comes about because higher ℓ partial-waves are more probable. Finally, each term in the sum is multiplied by P_ℓ, because in each ring there is a separate probability for leakage into the continuum.

Now, how is the distribution in energy ε of the ejected electron, $P_\ell(\varepsilon)$ calculated? $P_\ell(\varepsilon)d\varepsilon$ is the probability that the energy of the electron is in the interval $(\varepsilon, \varepsilon + d\varepsilon)$. At distance r, the following must be true

$$\varepsilon(r) = V_o(r) - V_+(r). \tag{15}$$

$P_\ell(\varepsilon)$ and $P_\ell(r)$ (from equation (10)) are related, since if a transition occurs at r with probability $P_\ell(r)$, then $\varepsilon(r)$ is uniquely defined by equation (15) and $P_\ell(\varepsilon)$ is the mirror probability of $P_\ell(r)$ in energy coordinates rather than distance coordinates. Thus

$$P_\ell(\varepsilon)\, d\varepsilon = P_\ell(r)\, dr \tag{16}$$

or rearranging

$$P_\ell(\varepsilon) = P_\ell(r)/|\varepsilon'(r)|, \quad r = r(\varepsilon) \tag{17}$$

where the prime denotes differentiation with respect to r and $r(\varepsilon)$ is the inverse function of $\varepsilon(r)$. Substituting $\varepsilon'(r) = V_o'(r) - V_+'(r)$ into equation (17) yields

$$P_\ell(\varepsilon) = P_\ell(r)/|V_o'(r) - V_+'(r)|, \quad r = r(\varepsilon). \tag{18}$$

There may be several values of r at which

$$\varepsilon = V_o(r) - V_+(r),$$

thus equation (18) should be modified to the form

$$P_\ell(\varepsilon) = \sum_i P_\ell(r)/|V_o'(r) - V_+'(r)|, \quad r = r_i(\varepsilon). \tag{19}$$

$P(\varepsilon)$ is found by summing over partial waves

$$P(\varepsilon) = \sum_\ell (2\ell+1)\, P_\ell(\varepsilon) \tag{20}$$

where again $2\ell+1$ is a weighting factor for partial wave ℓ.

The final translational energy in V_+ is given by $E - \varepsilon$. If $E - \varepsilon > 0$, V_+ is unbound and PI occurs. If $E - \varepsilon < 0$, V_+ is bound and AI occurs. A problem arises in deciding whether an AI product is actually bound. In both $V_o(r)$ and $V_+(r)$, the centrifugal term $\hbar^2\ell^2/2\mu r^2$ must be added, and for an attractive potential $V(r) = C_n r^{-n}$ with $n > 2$, a hump appears in the effective potential. An AI product AB^+ may be classically bound if to the left of this hump, but may quantum mechanically tunnel with a characteristic lifetime. Deciding whether a product is associated or not depends on the detection time scale of the experiment. More discussion of these quasibound AI species will appear later. Since Miller's theory is classical, he considers these quasibound molecules to be solely AI products. Thus for a transition occurring at distance r: It is AI if $E - \varepsilon < \max V_+^\ell$ and $r < r_{max}^\ell$, where V_+^ℓ is the effective potential including centrifugal energy and r_{max}^ℓ is the maximum in V_+^ℓ, and it is PI otherwise. The probabilities for PI and AI are

$$P_\ell^{PI} = \int_{r_o}^{\infty} dr\, P_\ell(r) \left\{ 1 - h(r_{max}^{\ell} - r)\, h[\max V_+^{\ell} - E + V_o(r) - V_+(r)] \right\} \tag{21}$$

$$P_\ell^{AI} = \int_{r_o}^{r_{max}^{\ell}} dr\, P_\ell(r)\, h[\max V_+^{\ell} - E + V_o(r) - V_+(r)] \tag{22}$$

where $h(x) = 1 \qquad x > 0$

$h(x) = 0 \qquad x < 0.$

Cross sections are again obtained by summing over partial waves

$$\sigma_{PI} = (\pi/k_o^2) \sum_\ell (2\ell+1)\, P_\ell^{PI}. \tag{23}$$

$$\sigma_{AI} = (\pi/k_o^2) \sum_\ell (2\ell+1)\, P_\ell^{AI}. \tag{24}$$

The final part of Miller's classical theory deals with the probability of an AI product in vibrational state n and rotational state ℓ, $P_{n,\ell}$. It is obvious that

$$P_\ell^{AI} = \sum_n P_{n,\ell}. \tag{25}$$

The loss of energy ε to the electron leaves a product energy $E - \varepsilon = W_{n,\ell}$, the vibrational-rotational energy of AB^+, thus

$$P_{n,\ell}\, dn = P_\ell(\varepsilon)\, d\varepsilon, \tag{26}$$

and

$$P_{n,\ell} = |\partial\, W_{n,\ell}/\partial n|\, P_\ell(\varepsilon) \tag{27}$$

with $\varepsilon = E - W_{n,\ell}$. Using the WKB eigenvalue equation

$$(n + \tfrac{1}{2})\pi = \int dr \left\{ (2\mu/\hbar^2) [W_{n,\ell} - V_+^{\ell}(r)] \right\}^{1/2}. \tag{28}$$

one finds that

$$\left|\frac{\partial W_{n,\ell}}{\partial n}\right| = \frac{\pi\hbar^2}{\mu} \Big/ \int dr\left(\frac{2\mu}{\hbar^2}\left[W_{n,\ell} - V_+^{\ell}(r)\right]\right)^{-1/2}. \tag{29}$$

Using equation (19) one finds

$$P_{n,\ell} = \left|\partial W_{n,\ell}/\partial n\right| \sum_i P_\ell(r)/\left|V_o'(r) - V_+'(r)\right|, \quad r = r_i(n,\ell) \tag{30}$$

where $r_i(n,\ell)$ must satisfy

$$E - W_{n,\ell} = V_o(r) - V_+(r). \tag{31}$$

If there are no values of r which satisfy equation (31), then no AI can classically occur.

The conclusions that can be drawn from Miller's theory are:

(i) The probabilities P_ℓ given by equations (3) and (7) for a transition should be greatest at the classical turning point of the trajectory for two reasons. $\Gamma(r)$ is larger at smaller distances and the time spent in a small segment (r,r+dr), $dr/V_\ell(r)$, should be large because the radial velocity is small at the turning point. This may be complicated by the survival factor however, which for systems with large overall $\Gamma(r)$'s may make larger r transitions more likely.

(ii) Total ionization probabilities should decrease with increasing relative kinetic energy, because P_ℓ depends inversely on $V_\ell(r)$ in equation (12). Physically, this is due to the fact that the collision occurs more rapidly, thus there is less time for a transition.

(iii) For some sets of potential curves (see Fig. 2 of Ref. 18), as discussed by Miller, $\varepsilon(r)$ should have a minimum at a certain value of r, say $r = r^*$, where $\varepsilon'(r) = V_o'(r) - V_+'(r) = 0$. From equation (18), $P_\ell(\varepsilon)$ becomes infinite. Thus the electron energy distribution should sharply peak at $\varepsilon(r^*)$ and products should be predominantly formed at $r = r^*$. This phenomenon (called the "edge effect" by Miller) will make classical turning point transitions less favorable.

(iv) For a given partial wave ℓ, increasing E (i.e. increasing the relative kinetic energy of the collision) favors PI over AI as predicted by equations (21) and (22). This agrees with qualitative arguments given earlier.

Miller also derives semiclassical and quantum theories for PI and AI. In the semiclassical theory, in-going and out-going phases are important, leading to interferences between transitions on the inward and outward part of the trajectory at the same value of R. The derived cross-sections differ from the classical result by interference terms only. In the quantum theory, in addition to interference effects, an additional coupling term is needed beyond $V_o(R)$, $V_+(r)$ and $\Gamma(r)$. Also, a more accurate radial velocity term that depends on $\Gamma(r)$ is derived, and can be used in the classical and semiclassical calculations as well.

The classical theory has to be modified somewhat if multiple ionization channels are open. If A^* can excite B^+ electronically, there are at least two V_+ curves in whose continuum the $(AB)^*$ collision complex is imbedded. Different J states may make the number of ionic curves

greater than two. $\Gamma(r)$ between $V_o(r)$ and each $V_+(r)$ must be calculated, and are in general not the same. $P_\ell(r)dr$ must include all possible transitions, and the survival factor must reflect the fact that the $(AB)^*$ collision complex has survived all open ionization channels. Thus with many channels, the long range behavior of $\Gamma(r)$ becomes more important and there is a good possibility the collision complex makes a transition before reaching the classical turning point. Theoretical calculations to test these conclusions would be interesting. Also, ejected electrons from the different processes could overlap in energy, making the electron spectrum complicated but extremely interesting. Investigations of this sort have been performed by Niehaus[19] and workers and Čermák[20] and workers using $He^*(2\ ^1S,\ 2\ ^3S)$, with the electron energy distributions in general sharply peaked with little overlap.

The next section will discuss the system chosen for study, the interaction of Ca atoms with Ar^*. It will be shown why the system is ideal for chemiluminescence studies.

C. Why Ca + Ar^*?

The system chosen to study associative and Penning ionization was the metastable argon ($^3P_2$) atom—calcium atom interaction. The energies of several metastable rare gases in relation to the singly-charged ionic states of several alkaline earth atoms are shown in Fig. 6. The zero of energy is taken to be the ground state $^1S_0$ atoms of both the rare gas and alkaline earth. Not only do the alkaline earths have low ionization potentials, they have low-lying electronic states in their

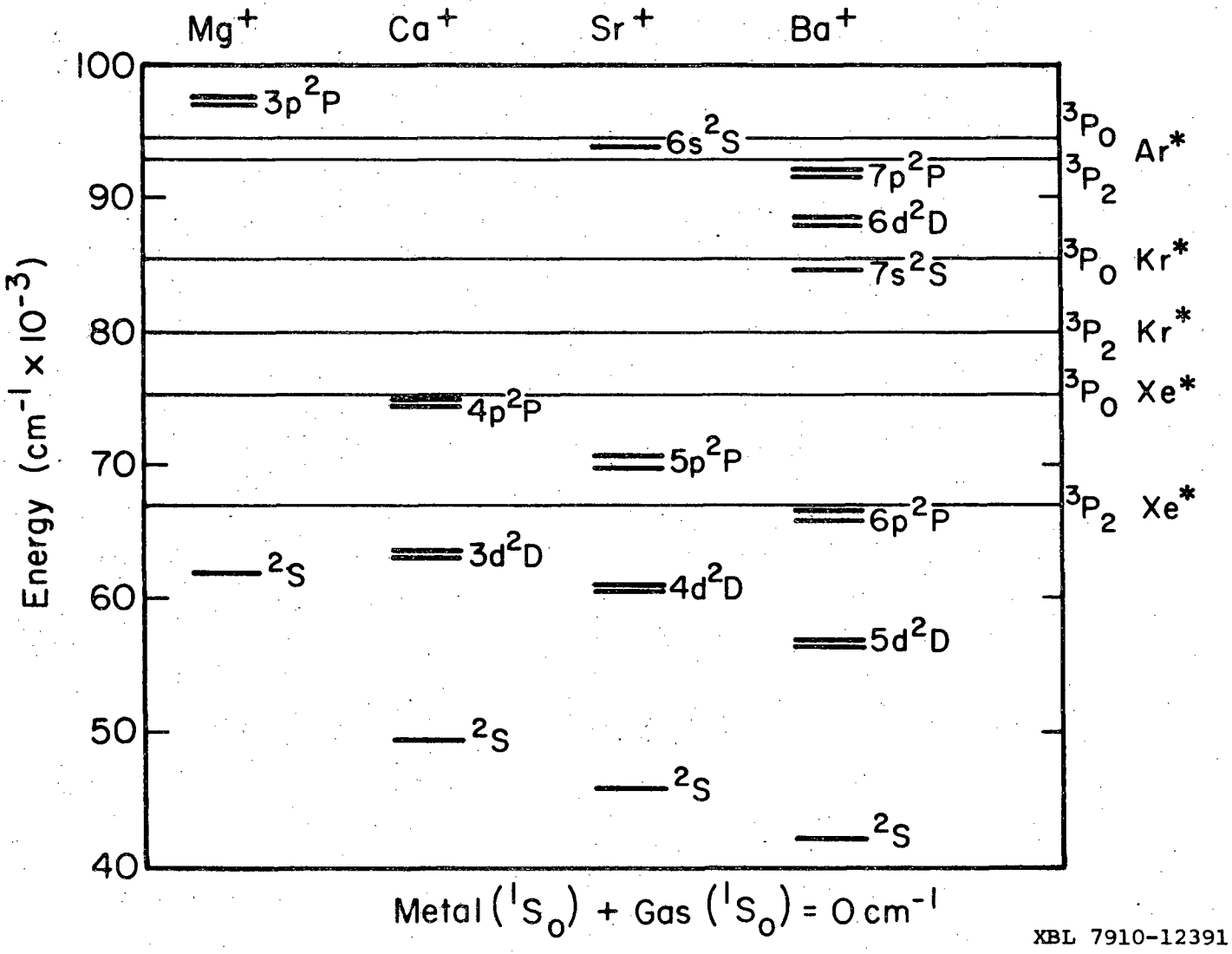

Fig. 6. Electronic energies of some alkaline earth monovalent ions in comparison to energies of the heavier metastable rare gases.

+ 1 ions. Thus, several different reactant combinations with metastable rare gases can lead to chemiluminescence of the resulting electronically excited product ion. Excitive Penning ionization (PI^*)

$$A^* + B \rightarrow A + B^{+*} + e^-$$

and excitive associative ionization (AI^*)

$$A^* + B \rightarrow AB^{+*} + e^-$$

are two energetically feasible kinetic channels, where A^* is the metastable rare gas and B the alkaline earth. PI^* and AI^* are of course in competition with other reaction channels, notably neutral excitation

$$A^* + B \rightarrow A + B^*$$

and PI and AI forming products in their ground states.

The Ca + Ar^* system was chosen for several reasons. First, the energetics are favorable, and are listed in Table III. The ionization potential of Ca $^1S_0$ atoms is 49306 cm^{-1} (6.11 eV). Excitation of Ca^+ to the $^2P^o_{1/2}$ and $^2P^o_{3/2}$ states requires 25192 cm^{-1} (3.12 eV) and 25414 cm^{-1} (3.15 eV) respectively; or upon adding in the ionization potential of Ca requires 74498 cm^{-1} (9.24 eV) for formation of Ca^+ $^2P^o_{1/2}$ and 74720 cm^{-1} (9.26 eV) for formation of Ca^+ $^2P^o_{3/2}$. The energy of Ar^* $^3P_2$ is 93144 cm^{-1} (11.5 eV), therefore PI^* and AI^* are exoergic by about 18,000 cm^{-1} or 2.2 eV. Second, the wavelengths of the Ca^+ $^2P^o \rightarrow {}^2S$ doublets are both around 4000 Å, at the peak of our spectral response curve. Third, the attractive potential holding $CaAr^+$ together is the ion-induced dipole potential

$$V(r) = - \frac{Z^2\alpha}{2r^4} ,$$

where Z is the charge on the ion and α is the polarizability of the rare gas atom. The polarizability[22] of Ar (1.64 $Å^3$) is much greater than that for He (0.2051 $Å^3$) or Ne (0.395 $Å^3$) and comparable to that for Kr (2.48 $Å^3$) and Xe (4.04 $Å^3$). Thus, larger well depths are expected for AI products with Ar than with He or Ne. The greater the well depth, the greater the likelihood of forming a bound AI product. With the polarizabilities in mind, Ar^* is cheaper and easier to make than Kr^* or Xe^*. Finally, the $Ca^+ {}^2P^o_{3/2,1/2}$ doublets at 3933.6 Å and 3968.47 Å are of astrophysical interest, and any mechanisms for their formation may help in the study of stellar and interstellar plasmas.

The ionization selection rules for the Ca + Ar^* system are important. During the collision, the $Ca(^1S)$ and $Ar^*(^3P)$ atoms correlate to $^3\Pi$ and $^3\Sigma^+$ electronic states. If the ejected electron carries away no orbital electronic angular momentum (i.e. is an S-wave), $^3\Pi$ gives rise to $^2\Pi$ ionic states while $^3\Sigma^+$ gives rise to $^2\Sigma^+$ ionic states. Thus $^2\Pi$ ionic states may be formed, and these are just the molecular states formed when an excited $Ca^+ {}^2P$ atom unites with a ground state Ar ^1S atom, although a $^2\Sigma$ state is also possible. Examination of Table III reveals a $Ca^+ {}^2D$ level can be formed on energetic grounds, but it is metastable and its emission around 7300 Å is not experimentally observed in this work.

D. $BeAr^+$ and a Model Potential

What are the bonding characteristics and spectral constants for $CaAr^+$? It is hard to guess, but fortunately a good deal of information is known about the closely related ions $BeAr^+$ and $BeKr^+$. Recently, Subbaram, Coxon, and Jones[23] reported the high resolution analyses of both the $A^2\Pi_r \rightarrow X^2\Sigma^+$ system of $BeAr^+$ and the $A^2\Pi_r \rightarrow X^2\Sigma^+$ system of $BeKr^+$. Both spectra were excited by a microwave discharge through $BeCl_2$ vapor with 200 torr of the appropriate rare gas. It was hypothesized that the formation of $BeAr^+$ or $BeKr^+$ was due to three-body collisions between Be^+ and two rare gas atoms. We have suggested another possibility,[24] that the formation of these molecules may be due to AI between two excited reactants, e.g.

$$Ar^*(^3P) + Be^*(^3P) \rightarrow BeAr^{+*}(^2\Pi) + e^-.$$

More kinetic studies are needed to determine the mechanism for molecule formation.

Nonetheless, the spectral constants for these molecules are known and are listed in Table IV for $BeAr^+$. The bonding in $BeAr^+$ and $BeKr^+$ stems from the ion-induced dipole interaction, the ion distorting the polarizable rare gas electron cloud toward the ion and the resulting induced dipole attracting the Be^+ positive charge. The separated atoms limit of the $X^2\Sigma^+$ state is $Be^+(^2S_{1/2})$ and ground state argon, while in the $A^2\Pi_r$ state it is $Be^+(^2P^o_{3/2,1/2})$ and ground state argon. Thus the single Be^+ valence electron is either in the 2s orbital or the 2p orbital for the X and A states, respectively. Examination of Table IV shows the bond dissociation energy of ground state $BeAr^+$ to be 4000-4500 cm^{-1} and

the excited state to be 11000-12000 cm^{-1}. Also, the upper state has a 0.15 Å shorter bond distance. Thus, although the net charge on the Be ion is always + 1, the orbital occupancy of the valence electron plays a large role in the bonding.

We have devised a model potential[25] which explains the aforementioned bonding characteristics. The form of the potential is:

$$V(r) = A\, e^{-Br} - (Z^2e^2\alpha/2r^4) \tag{32}$$

where Z is the unitless charge on the ion, e is the electron charge, α is the polarizability of the rare gas, and A and B are adjustable parameters. Ae^{-Br} is a common choice for repulsive potentials, since the repulsion is due in part to unfavorable overlap between atomic orbitals, whose long-range characteristics are exponential in character.

The parameters A and B can be related to the harmonic force constant k_e and the equilibrium bond distance r_e by first noting that:

$$\left(\frac{dV(r)}{dr}\right)_{r=r_e} = 0 \tag{33}$$

$$-BA\exp(-Br_e) + (2Z^2e^2\alpha/r_e^5) = 0$$

$$A = (2Z^2e^2\alpha/Br_e^5)\exp(Br_e). \tag{34}$$

It is also true that

$$\left(\frac{d^2V(r)}{dr^2}\right)_{r=r_e} = k_e \tag{35}$$

$$B^2A\exp(-Br_e) - 10Z^2e^2\alpha/r_e^6 = k_e.$$

Substituting for A yields:

$$B^2[(2Z^2e^2\alpha/Br_e^5)\exp(Br_e)]\exp(-Br_e) - 10Z^2e^2\alpha/r_e^6 = k_e$$

$$B = (k_e r_e^5/2Z^2e^2\alpha) + (5/r_e). \qquad (36)$$

We have shown[25] that a potential inversion of spectroscopic constants using a multi-parameter Thakkar potential leads to an ion-induced dipole interaction at long range, even though the potential was derived from only the first five vibrational levels. This lends credence to the use of the model potential in the analysis of related ions, most interest of which is $CaAr^+$.

Using the model potential, the charge Z can be considered a variable parameter and can be fixed by the dissociation energy. For the $X^2\Sigma^+$ state of $BeAr^+$, using ω_e (determined from k_e), r_e and the multiparameter Thakkar potential D_e of 4536 cm^{-1}, Z_Σ is calculated to be 1.29. From T_e, D_e of the $X^2\Sigma^+$, and the Be^+ $^2P^o_{1/2} \rightarrow {}^2S_{1/2}$ transition energy,[21] the dissociation energy of the $^2\Pi_r$ state is found to be 11,888 cm^{-1}. This yields a value for Z_π of 1.88.

The values of $Z_\Sigma = 1.29$ and $Z_\pi = 1.88$ are physically satisfying. In the Σ state, the valence electron of Be^+ is in a 2s orbital which should effectively shield the $1s^2 + 2$ core. Thus, argon experiences a charge of close to one. In the Π state however, the electron is in a $2p_x$ or $2p_y$ orbital, with the z-axis the bond axis. Having little electron density along the bond, the p-orbitals barely shield the core, and argon experiences a charge of close to two. Figure 7 is a schematic representation of the bonding, showing the van der Waals radius of Ar

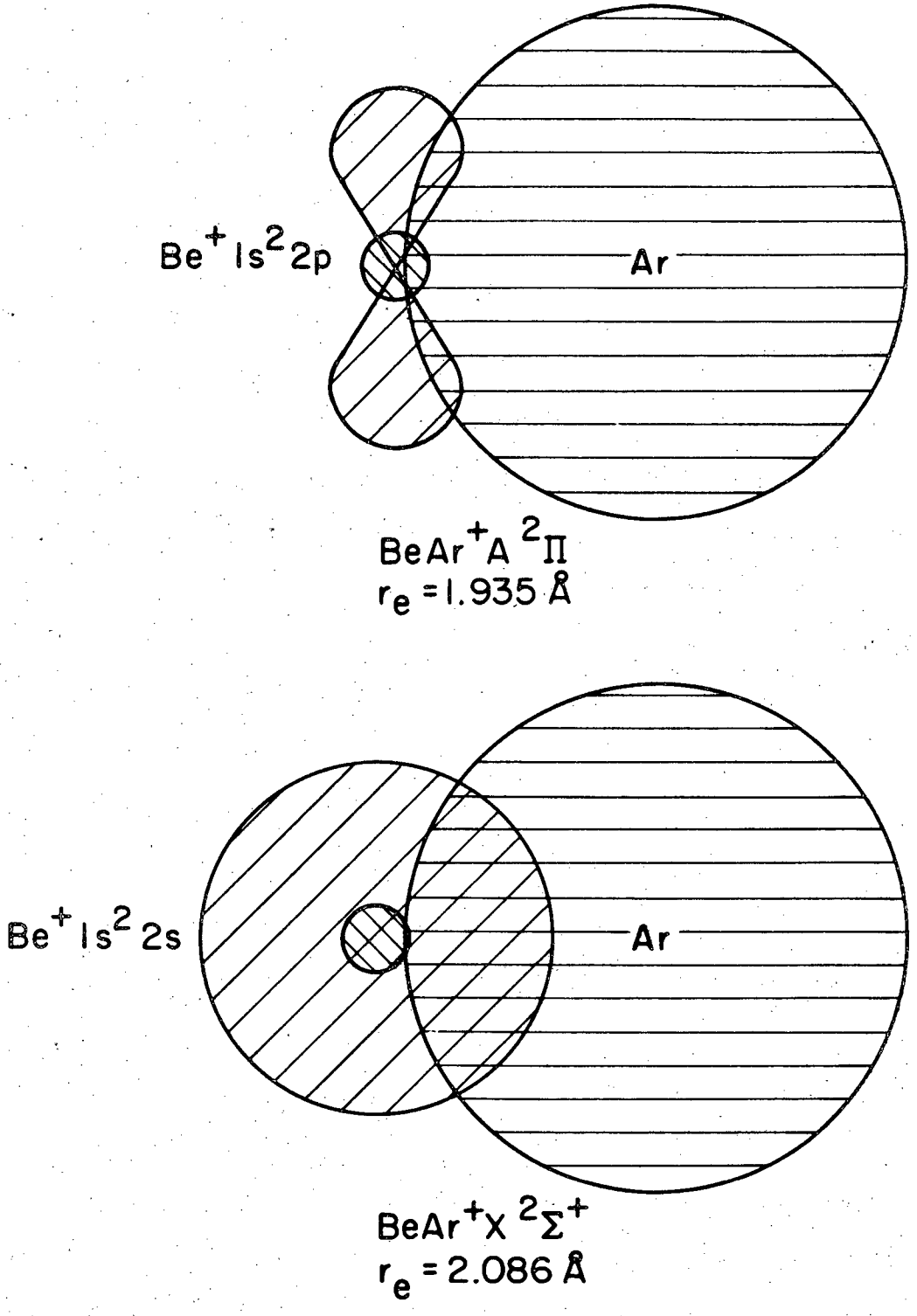

Fig. 7. Schematic of the atomic orbitals in $BeAr^{+}$ $^{2}\Sigma^{+}$ and $^{2}\Pi$.

and the 2s and 2p orbitals of Be^+. The smaller bond distance and greater dissociation energy of the excited A state are seen as natural consequences of the orbital occupancy of the electron.

If one assumes $Z_\Sigma = 1.29$ and $Z_\pi = 1.88$ to be invariant to a change in rare gas, application of the model potential to $BeKr^+$ yields $D_e(X^2\Sigma^+) = 5511\ cm^{-1}$ and $D_e(A^2\Pi_r) = 13656\ cm^{-1}$. The difference between these values ($8145\ cm^{-1}$) should equal the difference between the $Be^+\ ^2P^o_{1/2} \rightarrow {}^2S_{1/2}$ transition energy and T_e. This latter difference is $8146.6\ cm^{-1}$, which is in very good agreement, although the $2\ cm^{-1}$ accuracy is somewhat fortuitous.

Another important property of these molecular ions is their reduced curvature K, given by

$$K = \frac{r_e^2}{D_e}\left[\frac{d^2V(r)}{dr^2}\right]_{r=r_e} = \frac{\omega_e^2}{2B_eD_e}\ . \qquad (37)$$

For the X state of $BeAr^+$, K = 27.5, and for the A state K = 23.4, indicating a somewhat softer repulsion near the potential minimum for the A state. Many chemically bound diatomics have K in the range 10-20. Two molecular ions with extremely large K's are $HeNe^+$ with K = 51 and $HgAr^+$ with K = 50. All other diatomic ions in Huber and Herzberg[26] have K's in the range 9 - 28; one exception is H_2^+ for which K = 4.2.

Thus the bonding in $BeAr^+$ is well understood, being an attractive ion-induced dipole potential with an effective charge on the ion caused by valence electron screening (or lack of it) of the +2 core. Knowledge of $BeAr^+$ will prove useful in determining the properties of the closely related molecular ion, $CaAr^+$.

E. Experimental Results

Upon heating the stainless steel oven to 800-900 C filled with Ca shot (Alfa-Ventron 99.5%) and using Ar to help sweep the Ca atoms up into the interaction region, the reaction of Ar^* + Ca produced a bright violet flame easily visible by eye. The four strongest emission features were the 4226.73Å $^1P^o \rightarrow {}^1S$ Ca resonance line, the 6572.78Å $^3P^o \rightarrow {}^1S$ Ca intercombination line, and the 3933.66Å and 3968.47Å $Ca^+ {}^2P^o \rightarrow {}^2S$ resonance lines. All these lines had intensities in the range $1\text{-}5\times10^5$ counts/sec with 1 mm slit widths (a 2Å FWHM bandwidth). The excitations of the neutral Ca atoms are probably due to excitation from electrons by the following two processes

$$Ca + e^- \rightarrow Ca^* + e^-$$
$$Ca^+ + e^- + M \rightarrow Ca^* + M,$$

the electrons coming from PI and AI processes. Although at 1 torr total pressure three-body reaction rates are small, the second process is essentially two-body due to the large Coulombic attraction between Ca^+ and the electron.

The Ca^+ resonance doublets at 3934 Å and 3968Å are due to the excitive Penning ionization process

$$Ar^*(^3P_2{}^o) + Ca(^1S_o) \rightarrow Ar(^1S_o) + Ca^{+*}(^2P^o_{3/2,1/2}) + e^-(^2\ ).$$

In addition to these $^2P^o \rightarrow {}^2S$ transitions, with a Jarrel-Ash 1/4 meter monochromator the $^2P^o \rightarrow {}^2D$ Ca^+ transitions were also seen around 8500 Å. This emission is much weaker than the resonance lines, the branching ratios being 6%:94% for radiating to the ^2D and ^2S states. Of course,

Penning ionization forming ground state $^2S_{1/2}$ Ca^+ goes undetected, since only excited products can be observed with the apparatus. The two $^2P^o$ Ca^+ resonance lines have the intensity ratio (J = 3/2):(J = 1/2) of 5:1, and since they both have equal spontaneous emission rates, A_{ki}, of 1.5×10^8 sec^{-1},[27] this means that the upper J = 3/2 level of the $^2P^o$ manifold of Ca^+ is formed at five times the rate of the lower J = 1/2 level. The implications of this will be discussed later.

Absolute bimolecular rate constants for formation of these ion states upon collision with Ar^* ($^3P_2{}^o$) can be measured using the method described in Appendix B. The rate constants are measured by comparing the emission intensities to those of the 7602Å Kr line, an emission with a known rate constant. The [Kr] was measured by direct pressure determination, and the [Ca] was measured by atomic absorption, as described in Appendix A. The path length was chosen to be 5 cm, the dimension of the interaction region. Care was taken to insure that Kr and Ca had similar flow environments; thus Kr was swept up past the oven with Ar flows identical to that used to sweep the Ca. The temperatures of all gases were assumed to be 298 K, since the Ar should rapidly thermalize the initially hot Ca atoms. The results of two determinations yield the following rate constants:

$$Ar^*(^3P_2{}^o) + Ca(^1S_o) \rightarrow Ar(^1S_o) + Ca^{+*}(^2P^o_{3/2}) + e^-(^2\ )$$

$$k_{3/2} = 1.6 \pm 0.3 \times 10^{-10}\ cm^3\ molecule^{-1}\ sec^{-1}$$

$$Ar^*(^3P_2{}^o) + Ca(^1S_o) \rightarrow Ar(^1S_o) + Ca^{+*}(^2P^o_{1/2}) + e^-(^2\ )$$

$$k_{1/2} = 3.2 \pm 0.6 \times 10^{-11}\ cm^3\ molecule^{-1}\ sec^{-1}.$$

The error limits are purely statistical, and do not include any other errors which may be present. Dividing k by the relative velocity of the collision pair, $(8kT/\pi\mu)^{1/2}$, yields thermal cross-sections of 28 $Å^2$ and 6 $Å^2$ for the 3/2 and 1/2 states, respectively. These rate constants and cross-sections are in the typical range for Penning ionization reactions. For example, Riseberg, Parks, and Schearer[28] have measured Penning cross-sections for Ar^* + Zn and Ar^* + Cd of 52.8 $Å^2$ and 64.4 $Å^2$ respectively, using pulsed afterglow techniques.

An estimate of the mean reactive collision distance can be gotten by relating the thermal cross-section to the geometrical cross-section, πd^2. This yields d = 3.0 Å for formation of $^2P^o_{3/2}$ and d = 1.4 Å for formation of $^2P^o_{1/2}$.

Red-shifted from the Ca^+ resonance lines, a molecular band system is observed in the 4000-4500 Å region. Its intensity scales with the Ca^+ lines, and is attributed to the diatomic molecular ion $CaAr^+$, produced in the excitive associative ionization reaction

$$Ar^*(^3P_2^o) + Ca(^1S_o) \rightarrow CaAr^{+*}\ (^2\Pi_{3/2,1/2}) + e^-(^2\ ).$$

The spectrum is shown in Figs. 8 and 9. In the shorter wavelength region of the spectrum, there are extremely overlapping vibrational bands followed at longer wavelengths by four resolved continuum bands. The maximum intensities are around 200 counts/sec with 1 mm slits. The area under the $CaAr^+$ band was compared to the area under the Ca^+ doublets; and $CaAr^+$ accounted for 14% of the ionic emission. Thus the branching ratio of AI^*: PI^* is measured to be 14%:86%. With this, the AI rate constant is calculated to be $3.1 \pm 0.6 \times 10^{-11}$ cm^3 $molecule^{-1}$ sec^{-1}, and

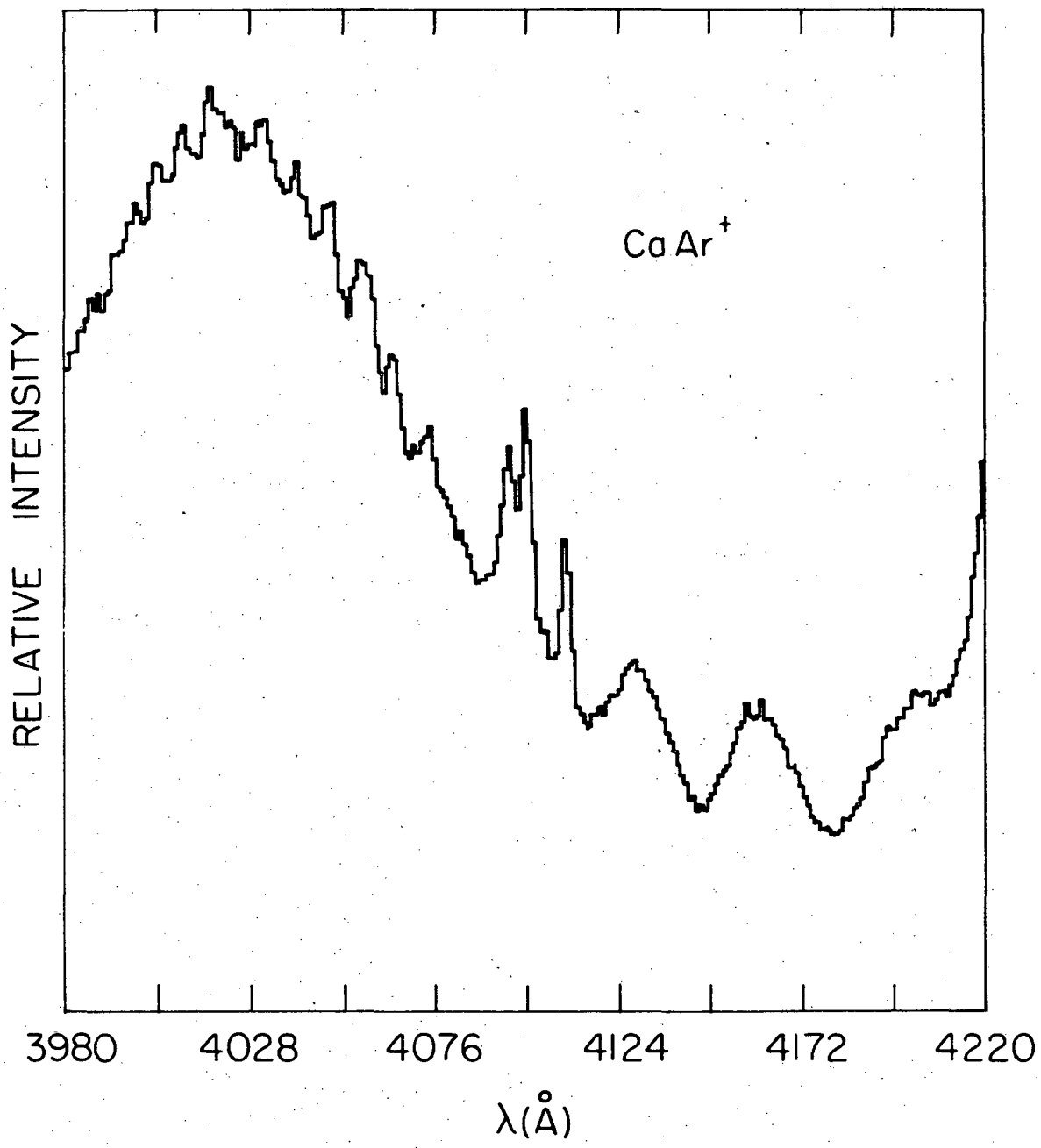

Fig. 8. Spectrum of $CaAr^+$ from 3980 to 4220 Å. The three sharp features in the middle of the spectrum are due to atomic Ca emission, and the rising feature at 4220 Å is due to the tail of the strong 4227 Å Ca resonance line.

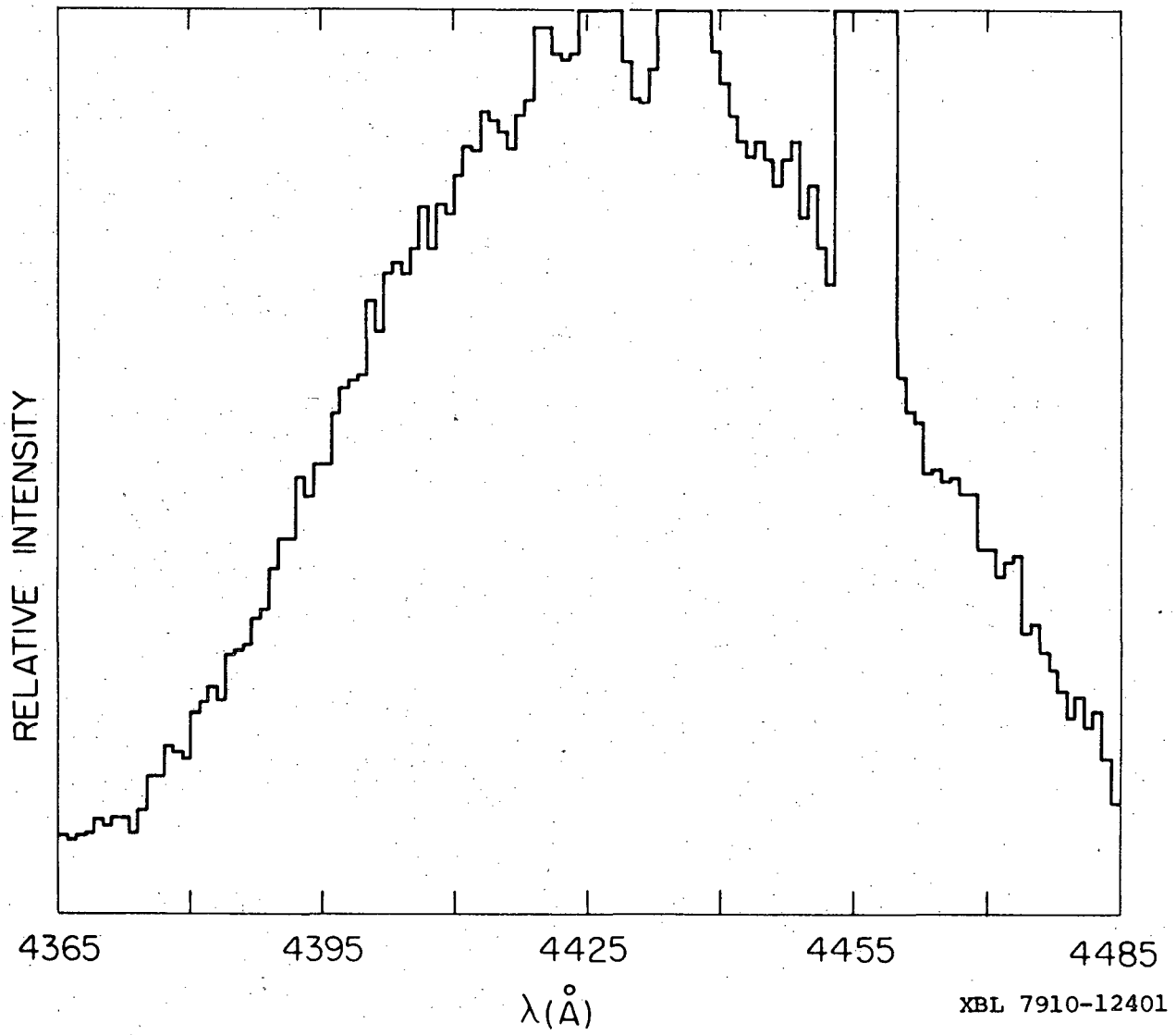

Fig. 9. The lowest energy bound-free continuum band of $CaAr^+$. The features that are off scale are due to atomic Ca lines.

the cross-section is 5.5 $Å^2$. This is a typical AI rate constant, for example Herman and Cermak[29] measured rate constants for the following AI reactions,

$$Ar^* + Na, K, Cs \rightarrow NaAr^+, KAr^+, CsAr^+ + e^- \quad (400K)$$

to be 1×10^{-10}, 1×10^{-10} and 3×10^{-10} cm^3 $molecule^{-1}$ sec^{-1}, respectively.

Table V lists the observed frequencies seen in the spectrum of $CaAr^+$. Absolute wavelengths were easily assigned, using accurately known Ca and Ca^+ atomic line wavelengths as calibration points.

F. Discussion

The mechanism for excitive PI and AI involves several electron transfers and excitations. At a certain distance, a valence Ca 4s electron jumps into the vacant 3p orbital on argon. Two possibilities now exist. One, as the electron transfers to Ar, the other Ca 4s electron transfers to the 3p orbital, and the Ar 4s electron is ejected as the free electron. Or two, after the Ca 4s electron has transferred, the Ar 4s electron jumps to the Ca 4p orbital and the free electron is ejected from the Ca 4s orbital. One cannot label electrons, and it may be hard to tell where the electron came from. There is one approach, though. Hotop and Niehaus[30] measured the laboratory angular distributions of ejected Penning electrons from the reaction $He^* + Ar \rightarrow He + Ar^+ + e^-$. They found forward peaked distributions enhanced in the direction of the He^* beam, with the obvious conclusion that the ejected electron probably came from the He 2s orbital. Similar experiments with $Ar^* + Ca$ may be fruitful, although complications may exist due to several ionization

channels being energetically available.

The 5:1 $^2P^o_{3/2}$: $^2P^o_{1/2}$ ratio for formation of Ca^{+*} with Ar^* is worth discussing. If orbital electronic angular momentum is conserved, the electron must be ejected as an s-wave, because the reactants have one unit of orbital electronic angular momentum (from Ar^* $^3P_2{}^o$) and the products already have one unit (in Ca^+ $^2P^o_{3/2,1/2}$). If the electron is an s-wave, its total electronic angular momentum, J, is due to spin alone, and is equal to $1/2\,\hbar$. Let us assume total electronic angular momentum is conserved in the process. The reactants have two units (due to Ar^* $^3P_2{}^o$), the product $Ar(^1S_0)$ has none, the product electron has one-half a unit, and thus the product ion should have 3/2 units. A propensity for forming $^2P^o_{3/2}$ Ca^+ atoms is seen experimentally, and may be a consequence of conservation of orbital and total electronic angular momentum. Ebding and Niehaus[31] have reacted He^* with Ar, Kr, Xe and Hg, and analyses of Penning electron energies and peak heights indicate that for Ar^+, Kr^+ and Xe^+ the $^2P_{3/2,\ 1/2}$ states are formed in equal amounts, and the same holds true for the Hg^+ $^2S_{1/2}$ and $^2D_{5/2,3/2}$ states. Why there are no differences in the formation of different angular momentum states is unclear. Ar^* and He^* are different, they carry different orbital electronic angular momentum and have different energies.

The $CaAr^+$ $^2\Pi \rightarrow {}^2\Sigma^+$ emission derives its oscillator strength from the Ca^+ resonance lines, and should thus have a similar radiative lifetime. The lifetimes of the $^2P^o$ states of Ca^+ are 6.7 nsec.[27] The collision frequency of Ar at 1 torr is 10^7 sec^{-1}, thus there are 10^{-7} sec between collisions. Collisional deactivation of vibration-rotation

states of $CaAr^+$ should be unimportant. The electronic spectrum can in principle give a detailed knowledge of the energy distribution in the AI product, knowledge of which can be very useful in understanding the reaction dynamics of this important process. This is the first chemiluminescent AI reaction ever studied, other studies measuring ejected AI electrons.

Visual inspection of the $CaAr^+$ spectrum immediately leads one to the conclusion that highly vibrationally excited $^2\Pi$ $CaAr^+$ molecules are formed. The vibrational wavefunction at the inner turning point has good Franck-Condon overlap with the continuum function on the repulsive, unbound wall of the ground $^2\Sigma^+$ state, leading to bound-free continuum oscillations. The vibrational wavefunction at the outer turning point has good overlap with bound levels in the lower state, leading to higher frequency bound-bound transitions. The continuum oscillations occur because the equilibrium bond distance in the Π state is less than in the Σ state, in accord with observations of $BeAr^+$ previously discussed.

Because of the intensity weakness and the considerable overlapping of vibrational bands, rotational constants and populations would be difficult to obtain, most important of which is the equilibrium bond distance, r_e. Also, because high vibrational quantum numbers are excited in the upper state, the important quantity ω_e is difficult to obtain.

To obtain an estimate of the vibrational quantums involved and the potential energy curves, a method was devised for synthesizing theoretical spectra. The method is as follows:

(i) The parameters Z, ω_e and r_e of the previously described model potential were input for both the upper $^2\Pi$ state and the lower $^2\Sigma^+$ state of $CaAr^+$. These parameters defined the potential curves involved.

(ii) The vibrational energy levels were numerically calculated using the Bohr-Sommerfeld quantization rule

$$h(v + \frac{1}{2}) = \oint p_r \, dr = 2\int_{r_-}^{r_+} [2\mu(E - V(r))]^{1/2} \, dr$$

where r_- and r_+ are the inner and outer turning points, respectively, of the vibration. This method did an excellent job in calculating the observed levels in $BeAr^+$.[25]

(iii) Franck-Condon factors were either estimated using vertical transitions or calculated using numerical bound and continuum wavefunctions calculated by the method of Cooley. (See reference 25 and references therein.)

(iv) The spectral frequencies and continuum oscillations were synthesized. The difference between the asymptotic limits of the two potentials was chosen to be the $^2P^o_{3/2} \rightarrow {}^2S_{1/2}$ Ca^+ transition energy at 25414 cm^{-1}, which is equivalent to saying that the $^2\Pi_{3/2}$ state is more populated than the $^2\Pi_{1/2}$ state, valid if orbital and total electronic angular momentum are conserved.

(v) Z, ω_e and r_e are then adjusted to improve the fit.

The blue continuum limit of a transition from a particular $^2\Pi$ vibrational state is an extremely informative number. This limit arises from the fact that successive lobes of the vibrational wavefunction overlap with continuum wavefunctions, the transitions becoming higher in frequency as one moves outward in bond distance along the vibrational wavefunction. Eventually bound-bound transitions appear past the continuum limit. The experimentally observed continuum limit is in the range 24300-24500 cm^{-1}. The difference between the continuum limit and the $^2P^o_{3/2} \rightarrow {}^2S_{1/2}$ transition energy (25414 cm^{-1}) gives the energy below dissociation of the vibrational states in the $^2\Pi$ state. This number is around 1000 cm^{-1}.

The continuum limit is also of value in assessing the $^2\Pi$ potential curve. It determines what vibrational states are involved in the transitions, and if these states are spaced incorrectly, the potential is discarded. The best potentials found are shown in Fig. 10. The parameters for the $^2\Pi$ state were found to be Z = 2, ω_e = 200 cm^{-1} and r_e = 2.6 Å and for the $^2\Sigma$ state were found to be Z = 1, ω_e = 87 and r_e = 2.8 Å. The upper state dissociation energy is estimated to be 4900 cm^{-1} and the lower state dissociation energy is 1000 cm^{-1}. The reduced curvatures, K, are both around 34. Table VI lists the calculated frequencies for v' = 28-31, comparing them to experimental values. The continuum band frequencies were calculated as the maximum in the Franck-Condon factor between the bound upper vibrational level and the lower unbound continuum state. The bound frequencies are calculated as vertical transitions between the outer turning points of both potentials. These bound frequencies for v' = 28-31 are in excellent agreement with experiment, but

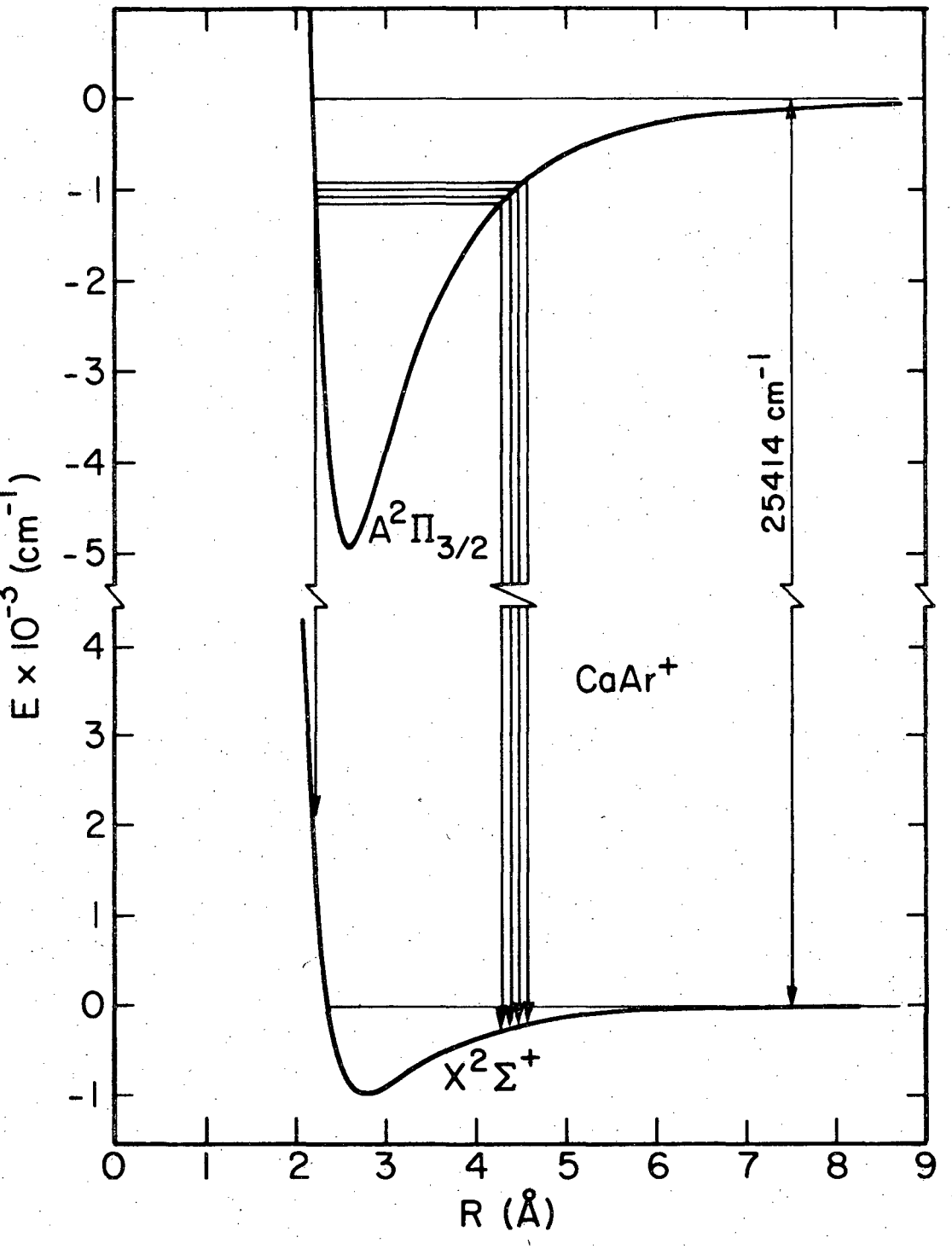

XBL 7910-12397

Fig. 10. The best model potentials that fit the experimental frequencies for $CaAr^+$. Shown are inner turning point bound-free transitions and outer turning point bound-bound transitions for v' = 28 to 31.

are in a sense artificial since transitions between calculated vibrational energy levels cannot duplicate the experimental frequencies using this set of potential curves. These three-parameter potential functions must be considered only rough estimates of the true potential, and since they are based on quantities at r_e, they are expected to be less accurate at high vibrational energies. In particular, the parameter Z has a certain value at r_e, but at large r it must approach 1. Thus holding Z constant is an approximation; it actually varies with distance.

Electron spectroscopy gives detailed information about the vibrational energy below dissociation of associative ions from an analysis of the high energy tail in the electron energy distribution. For $HeKr^+$ and $HeXe^+$, from the reactions of He^* with Kr and Xe, Hotop and Niehaus[19b] have measured values less than 800 cm^{-1}, i.e. on the order of thermal energies. The value of ~1000 cm^{-1} for $CaAr^+ {}^2\Pi$ can be taken as typical of many associative product ions. Somewhat higher values were found[19c] for metal atoms in the reactions He^* + Na, K, Hg, the values being in the range of 1600-6000 cm^{-1}. Electron spectroscopy experiments with Ar^* atoms as energy donors need to be done, and Ar^* + Ca would be a good first choice.

Note in Fig. 8, the $CaAr^+$ spectrum, that the higher energy bound-bound transitions tend to diminish in intensity. This may due to fact that these levels are becoming increasingly centrifugally bound, and can tunnel through the barrier forming Ca^{+*} + Ar. Tunneling rates can compete with radiative rates near the barrier maximum, with Morgner[32] calculating typical lifetimes of less than 10^{-7} sec for centrifugally

bound HeH^+ molecules. The tunnelling rates depend on the mass and the position below the barrier maximum. But in general, higher vibrational quantum states are more susceptible to tunnelling effects.

In light of this work, studies aimed at determining the $CaAr^+$ potentials more accurately are needed. Crossed beam studies of Ca^+ + Ar collisions would be a great help in determining the $^2\Sigma^+$ curve. Ab initio calculations would be interesting, although ionic forces are not well suited to this type calculation. A high-pressure discharge of Ca vapor in Ar may give rise to $CaAr^+$ emission with low vibrational quantum numbers due to collisional deactivation and possibly different mechanisms of formation.

Periodic trends in the related molecules $CaAr^+$, $BeAr^+$, NaAr and CaCl are worth mentioning. They all have $^2\Sigma^+$ ground states with an s-shell valence electron centered mainly on the metal atom. The forces binding $BeAr^+$ and $CaAr^+$ are identical, $BeAr^+$ more strongly bound because the smaller Be^+ atom allows Ar in closer, increasing the ion-induced dipole attraction. NaAr is held together by a weak van der Waals attraction, with a well depth of only ~ 45 cm^{-1}. CaCl is a strongly bound ionic compound, held together by the Coulomb attraction. The vast differences in electrostatic bonding between these electronically similar molecules is an interesting periodic trend.

It has been shown that chemiluminescence studies can determine much information about an ionizing collision, such as rate constants, atomic ion branching ratios, AI to PI branching ratios, and in principle detailed knowledge of the AI internal energy distribution. Studies like

this should be a useful compliment to other methods, in particular molecular beam scattering, mass spectrometry, and electron spectroscopy.

G. Conclusions

The conclusions that can be drawn from the study of both chemiluminescent AI and PI of Ca atoms by Ar^* can be summarized as follows.

(1) The thermal rates for excitive ionization are fast, and quite typical in comparison to other similar reactions.

(2) The branching ratios for AI^* : PI^* of 14%:86% are also quite typical in comparison to other reactions.[1]

(3) The 5:1 branching ratio for $Ca^+ {}^2P^o_{3/2}$: $ {}^2P^o_{1/2}$ formation may be the result of a propensity for conserving both orbital and total electronic angular momentum.

(4) High vibrational quantum numbers of the molecular ion are excited in AI^*, leading to extremely overlapped bands and continuum oscillations.

(5) Model potential parameters that best fit the observed frequencies were for the $ {}^2\Pi$ state Z = 2, ω_e = 200 cm^{-1}. r_e = 2.6 Å and D_e = 4900 cm^{-1} and for the $ {}^2\Sigma$ state Z = 1, ω_e = 87 cm^{-1}, r_e = 2.8 Å and D_e = 1000 cm^{-1}.

(6) The vibrational excitation of the AI ion, $CaAr^{+}\ ^{2}\Pi$, is about 1000 cm^{-1} below the dissociation limit, another indication of high vibrational quantum numbers.

(7) Chemiluminescence studies are an extremely useful tool in the study of product ion energy distributions.

IV. COLLISIONAL DISSOCIATION OF METAL CARBONYLS

A. Introduction

The metal carbonyls have long been recognized as candidates for the generation of gas phase metal atoms without the need for high temperature sources. $Fe(CO)_5$, with a vapor pressure of 30 torr at 25 C, and $Ni(CO)_4$, with a vapor pressure of 400 torr at 25 C, are both volatile, explosive, toxic liquids at room temperature. Many other metal carbonyls, even the solids, are reasonably volatile. This chapter will describe a new and unique method of creating ground and excited state gas phase metals, which involves collisional energy transfer from a metastable rare gas atom to a metal carbonyl. The experimental results and models for the dissociation mechanism will be discussed. Comparisons between this work and other dissociation and metal excitation mechanisms will be discussed, in particular photolysis and arc methods. Finally, future applications of this work will be examined.

B. Experimental Results

The first system studied was $Ar^* + Fe(CO)_5$. Gas phase $Fe(CO)_5$ was admitted from a reservoir of the neat liquid (Alfa-Ventron 99.5%) at room temperature. The interaction with Ar^* produced a bright blue flame observable by eye. The resulting spectrum is shown in Fig. 11. The surprising result is that all the sharp features can be readily assigned to known atomic iron transitions! The molecular bands between 3500 and 4000 Å are the $C \rightarrow B$ system of N_2, and the band around 6300 Å

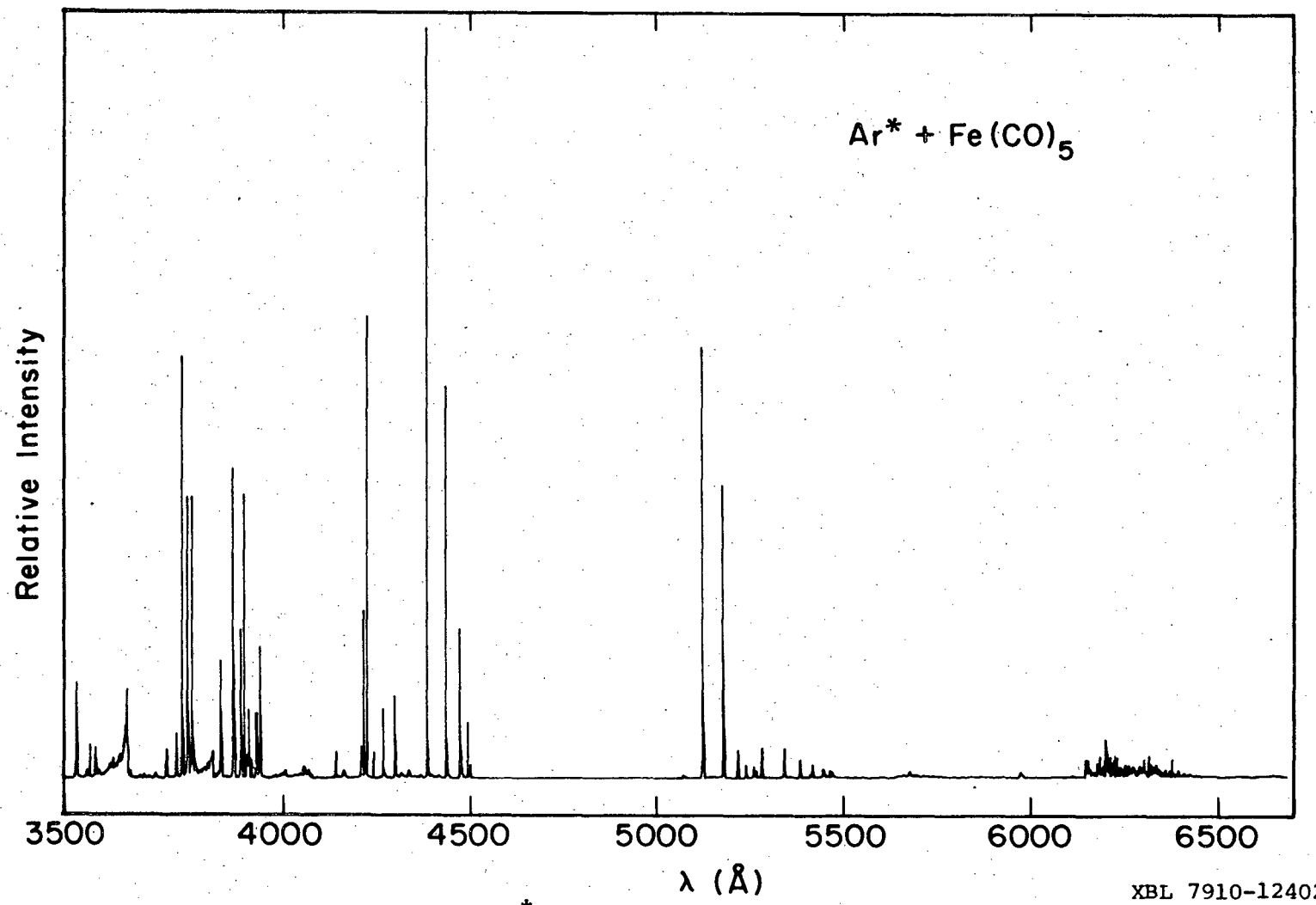

XBL 7910-12402

Fig. 11. The flame spectrum of Ar^* + $Fe(CO)_5$. The molecular emissions between 3500 and 4000 Å are due to N_2, and the band around 6200 Å is OH emission in second order.

is the OH A → X system in second order. These band systems are due to impurities in Ar and $Fe(CO)_5$ and are always observed in any spectrum with Ar^*. There are no observable emissions from $Fe(CO)_5$ or any of its fragments between 2000 and 8200 Å, the scanning range limits. The strongest Fe emissions were on the order of 10^4 counts/sec with 1 mm slit widths (a 2 Å FWHM bandwidth).

The spectra of the remaining five combinations of Ar^*, Ne^* and He^* with $Fe(CO)_5$ and $Ni(CO)_4$ (Matheson 99.9 %) are shown in Figs. 12-16. All $Fe(CO)_5$ flames were blue while all $Ni(CO)_4$ flames were reddish-blue. Again, all the sharp features are due to atomic Fe or Ni transitions. The weak bands between 4500 and 5000 Å (double headed and shaded to the red) in the spectrum of $Ne^* + Ni(CO)_4$ are the (0,0) and (0,1) bands of the A→X comet-tail system of CO^+. The Penning ionization process

$$Ne^*(^3P_2) + CO(X^1\Sigma^+, v=0) \rightarrow Ne + CO^+(A^2\Pi_i, v=0) + e^-$$

is exothermic by 610 cm^{-1}, and these features are attributed to CO impurity in the $Ni(CO)_4$ lecture bottle or secondary Penning ionization of the CO fragments. The absence of CO^+ emission from $Fe(CO)_5$ warrants further investigation. The only feature that could possibly be emission from a molecular carbonyl is in the $Ar^+ + Ni(CO)_4$ spectrum, where a very weak (20 counts/sec maximum with 1 mm slits) featureless continuum was observed from 5300 Å to the limit of our scanning range at 8200 Å. Study of this continuum also warrants further investigation.

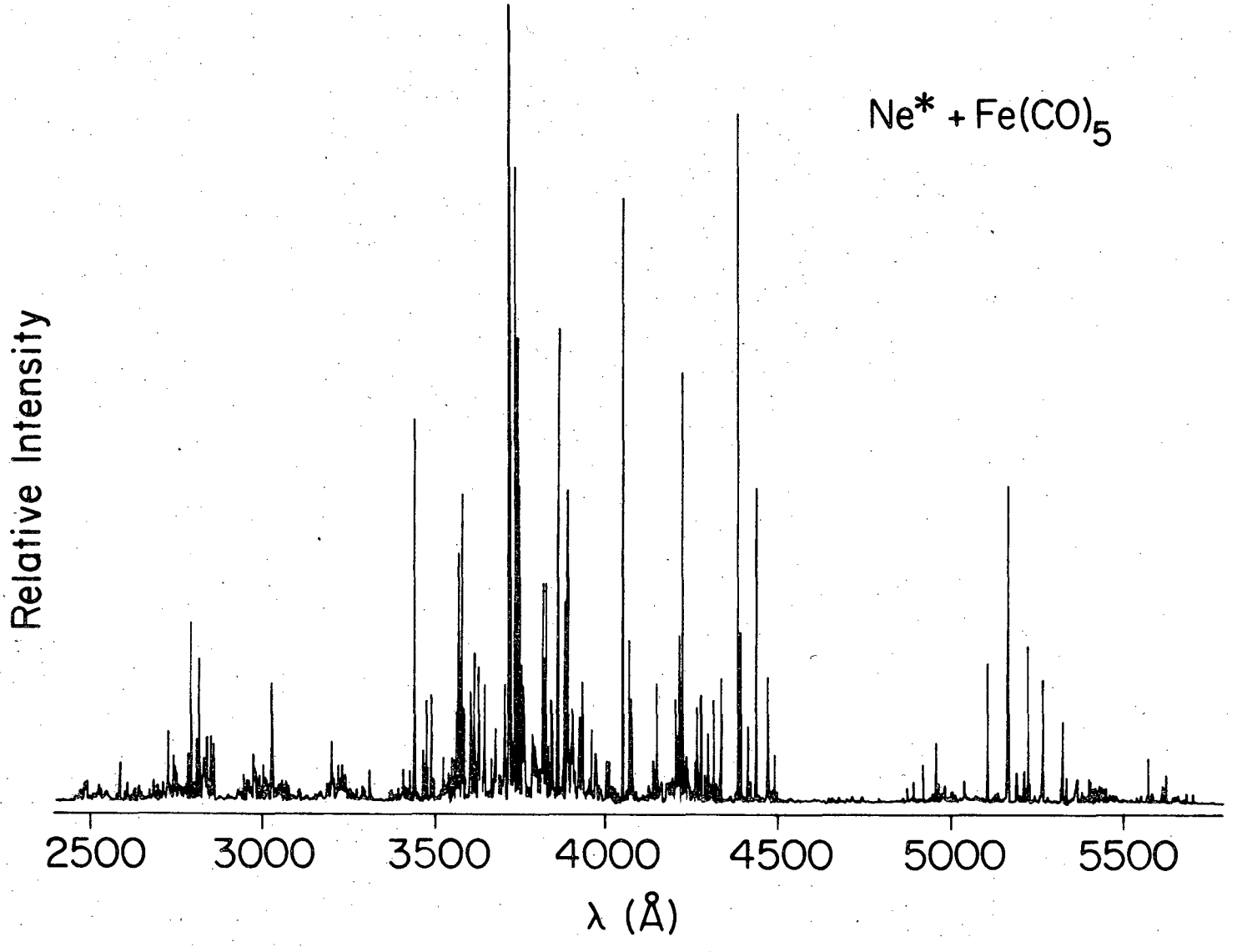

Fig. 12. The flame spectrum of $Ne^{*} + Fe(CO)_5$.

XBL 7910-12379

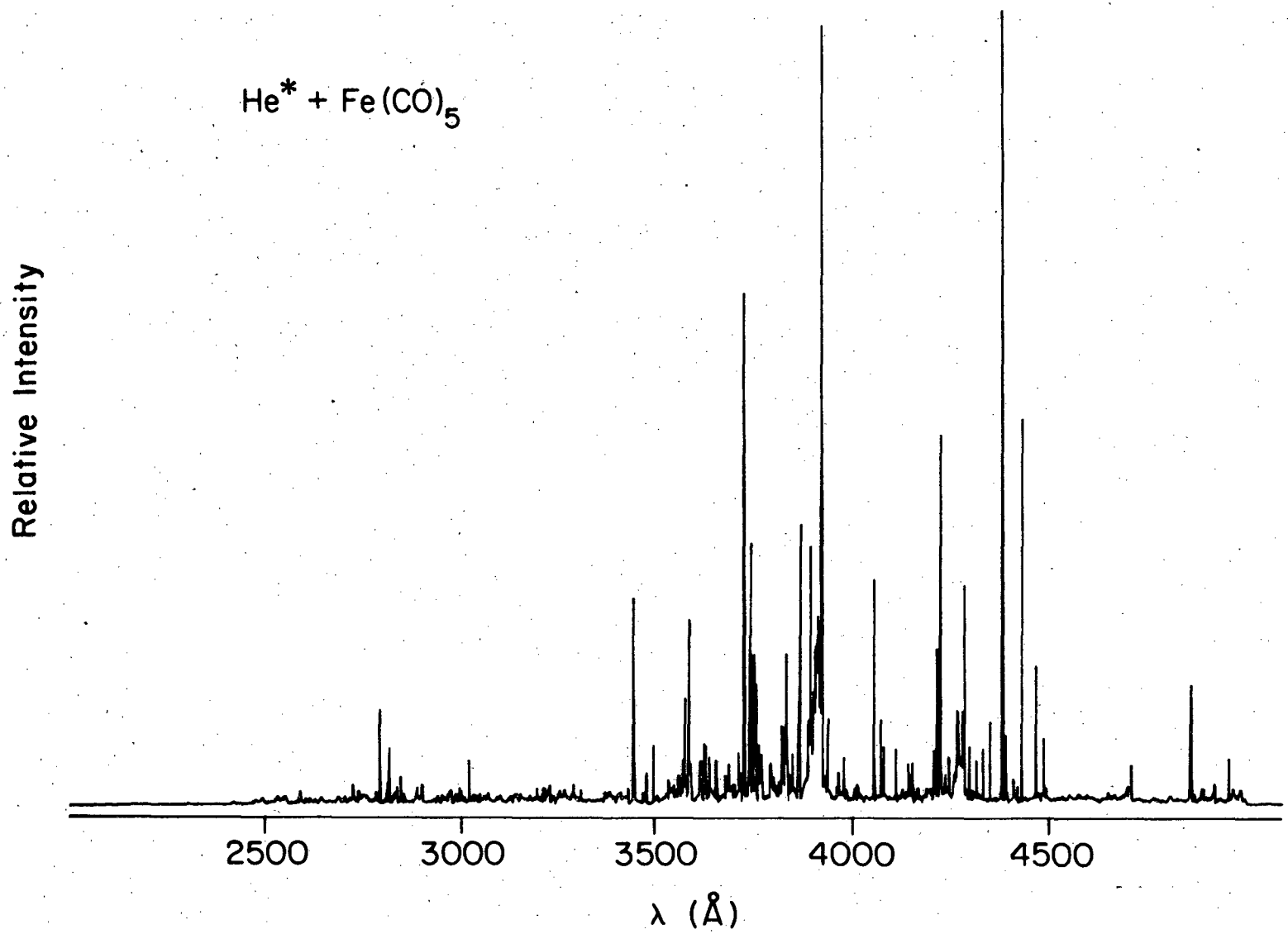

Fig. 13. The flame spectrum of $He^* + Fe(CO)_5$. XBL 7910-12380

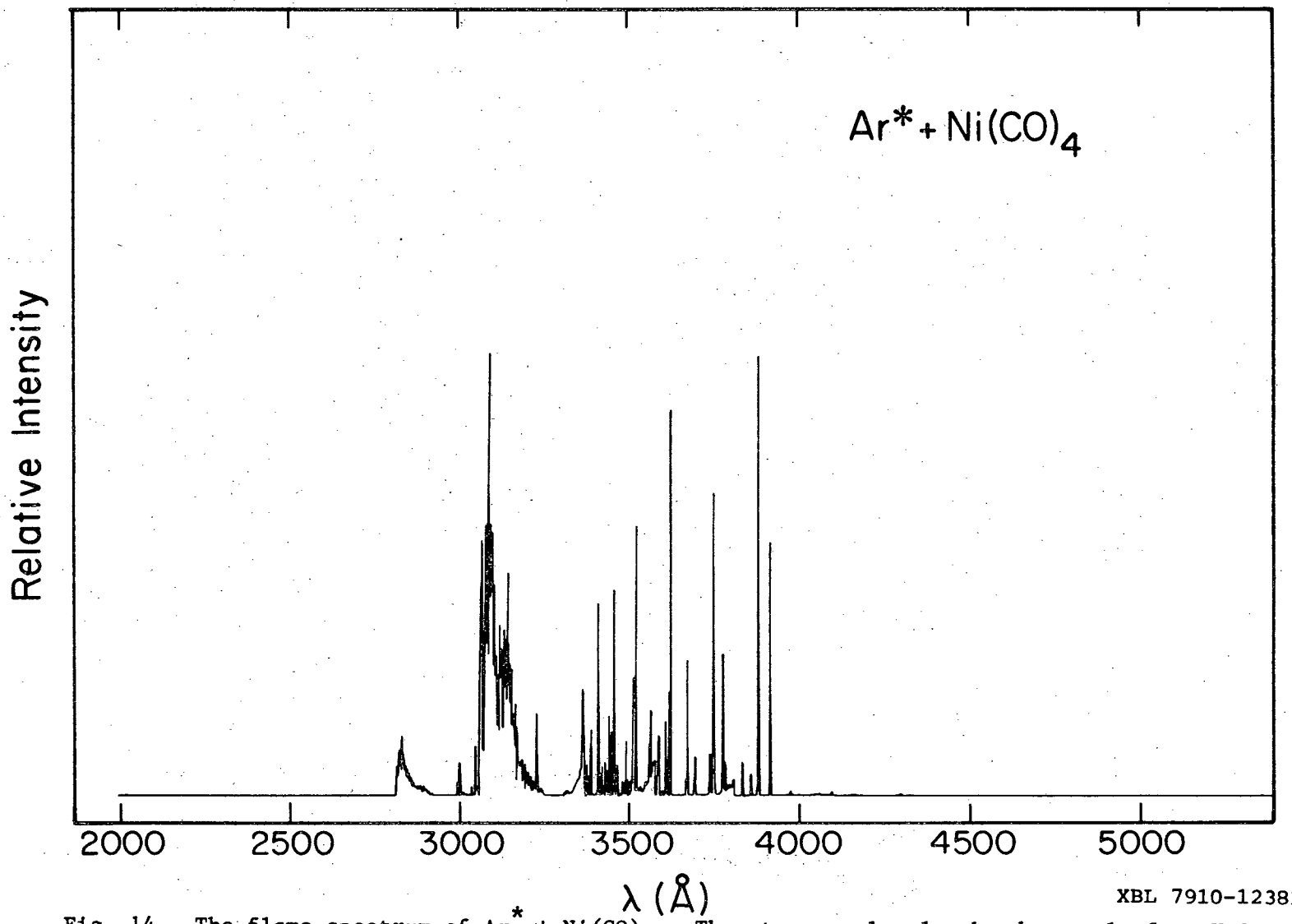

XBL 7910-12381

Fig. 14. The flame spectrum of $Ar^* + Ni(CO)_4$. The strong molecular bands result from H_2O impurities. The weaker bands around 3500 Å are due to N_2.

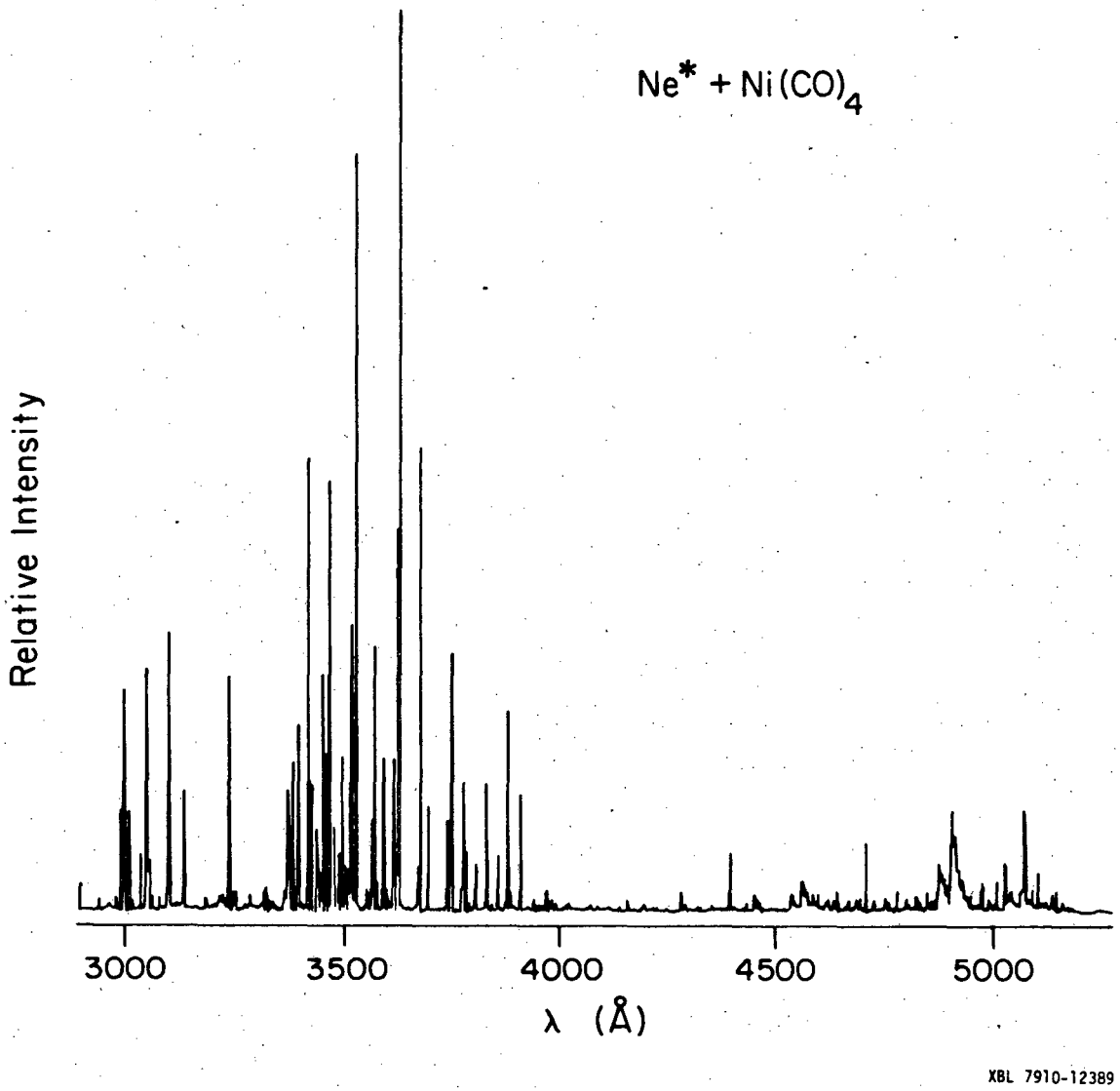

Fig. 15. The flame spectrum of $Ne^* + Ni(CO)_4$. Note the CO^+ bands between 4500 and 5000 Å which are discussed in the text.

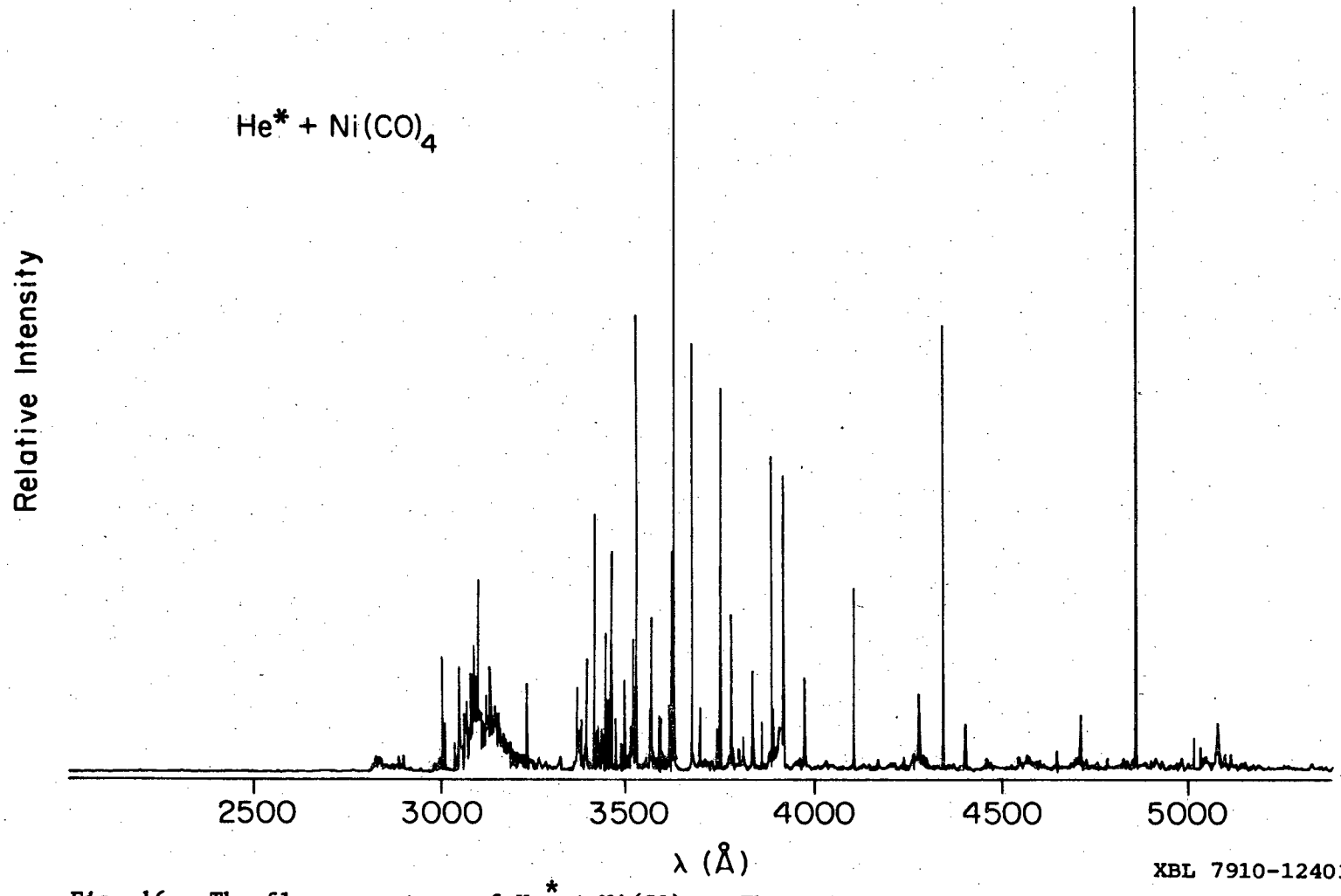

Fig. 16. The flame spectrum of He^* + $Ni(CO)_4$. The molecular band is a result of H_2O impurity.

The strongest emission features for all Ar^* and Ne^* spectra were on the order of 10^4 counts/sec with 1 mm slits. The He^* intensities were down by a factor of 10, probably due to less efficient metastable production. Wavelengths were readily measured to an accuracy of 0.1 Å or better, if such resolution was required.

C. Kinetic Experiments

Several kinetic experiments were performed to determine the dependence of the metal atom emissions upon Ar^* and metal carbonyl concentrations. The emission rate of the strongest Fe line at 4375.93 Å was monitored as a function of total argon pressure (and thus of Ar^* concentration). The result is shown in Fig. 17, along with a separate experiment monitoring the N_2 3370 Å band, an emission known to be first order in Ar^*. The two curves are identical, establishing first-order dependence of the Fe emission rate with Ar^* concentration. A similar experiment monitoring the strongest nickel line at 3881.86 Å is shown in Fig. 18. Here the change in Ar^* concentration was reflected by different argon backing pressures far upstream from the interaction region. As for Fe, the Ni atom emission is first-order in $[Ar^*]$.

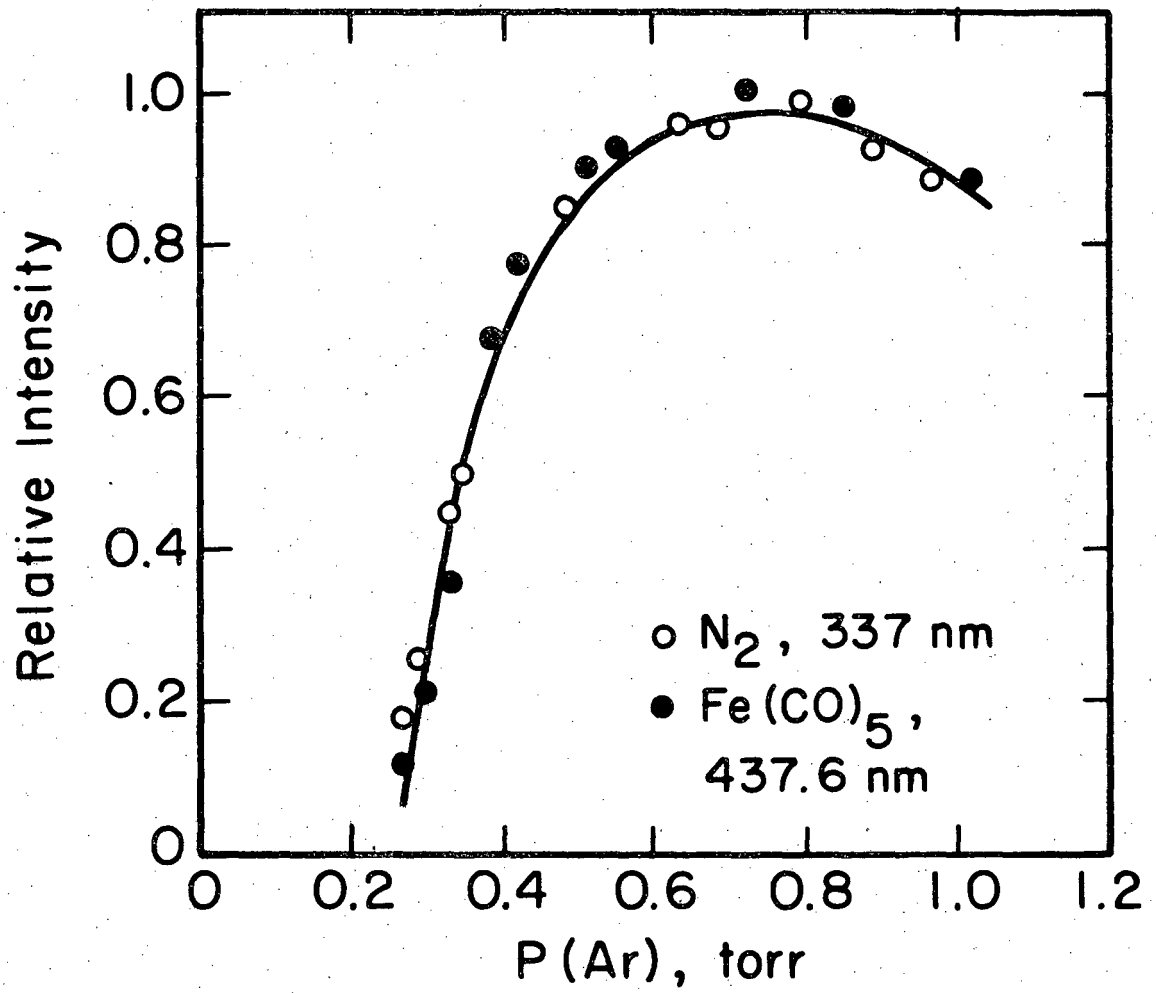

XBL 7910-12398

Fig. 17. The variation in Fe 437.6 nm emission intensity as a function of Ar pressure, and hence Ar^* concentration. The same experiment for N_2 337 nm emission, an excitation process known to be first order in Ar^* concentration.

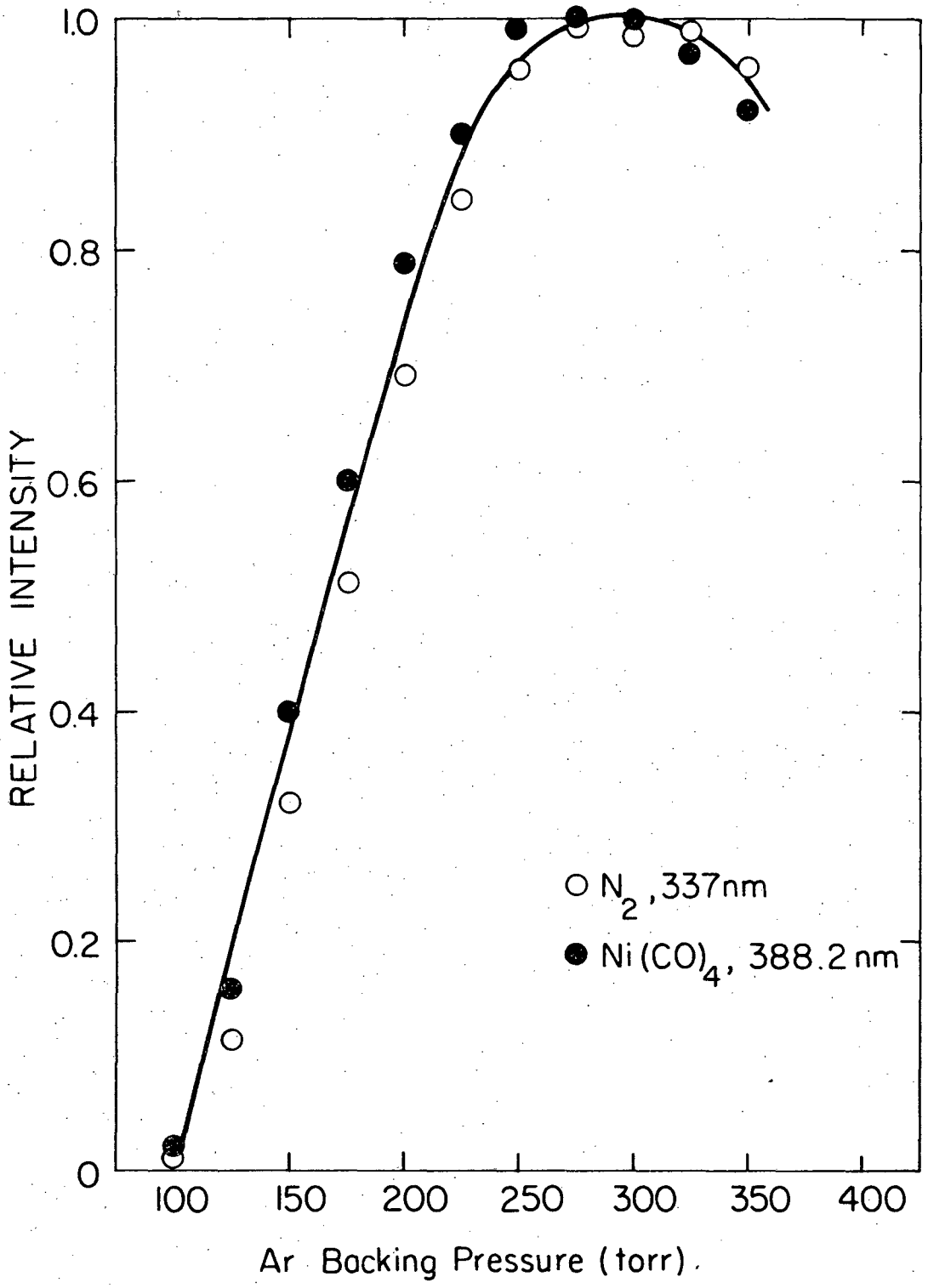

XBL 7910-12404

Fig. 18. The variation in Ni 388.2 nm emission intensity as a function of upstream Ar backing pressure, and hence Ar^* concentration. The same experiment for N_2 337 nm emission, an excitation process known to be first order in Ar^* concentration.

Also, these same emission intensities were monitored as a function of carbonyl pressure, holding $[Ar^*]$ constant. In the 0.1 - 2 micron pressure range, the Fe^* and Ni^* intensities were linear functions of carbonyl pressure, as shown in Figs. 19 and 20. At higher pressures, the emission intensities approach a zero-order dependence on carbonyl pressure, as the carbonyl begins to titrate the metastables.

The most plausible conclusion to draw from the kinetic studies is that we are observing the elementary bimolecular process

$$X^* + M(CO)_n \rightarrow X + M^* + nCO,$$

where X^* is the metastable rare gas, and M is either Ni or Fe. Recent studies[33] in a molecular beam apparatus of $Ar^* + Fe(CO)_5$ and $Ne^* + Fe(CO)_5$ have recorded atomic iron chemiluminescence, unequivocally establishing that the reactions are bimolecular.

D. Comparison With Arc Spectra

The standard arc spectra of Fe and Ni metals, synthesized from published line intensities,[34] are shown in Fig. 21. Visual comparisons of the arc spectra with the carbonyl spectra show marked differences between the two modes of metal atom excitations. Table VII lists the relative intensities of the stronger Fe arc lines and the stronger $Ar^* + Fe(CO)_5$ flame lines. The strongest arc line ($y\ ^5F_5{}^o \rightarrow a\ ^5F_5$ at 3734.87 Å) is missing from the flame; conversely, the strongest flame line ($z\ ^7F_5{}^o \rightarrow a\ ^5D_4$ at 4375.93 Å) is very weak in the arc. In general, the strongest flame features arise from terms derived from the

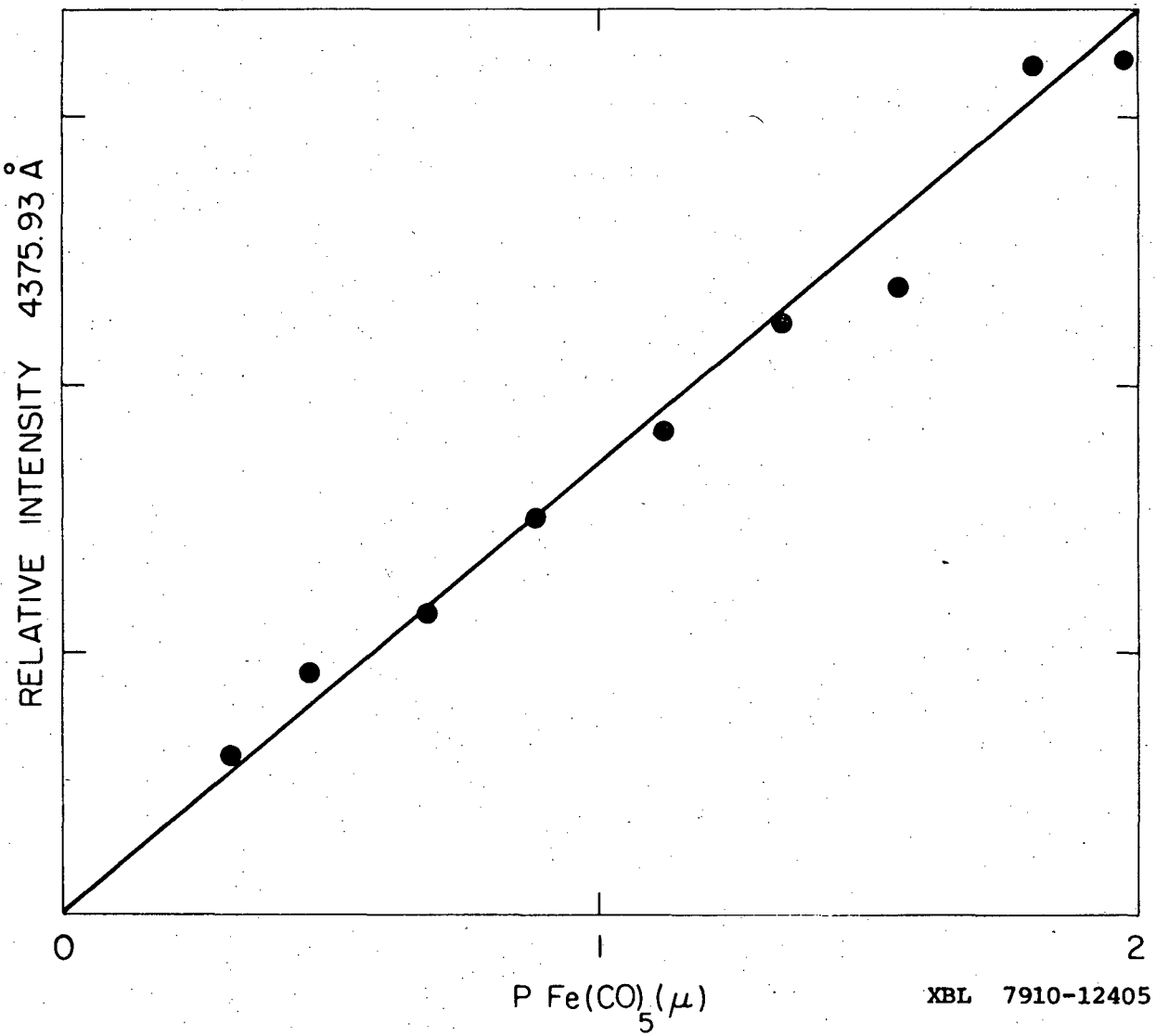

Fig. 19, Relative intensity of Fe 4375.93 Å emission as a function of $Fe(CO)_5$ pressure in the 0-2 μ range. The Ar^* concentration is held constant.

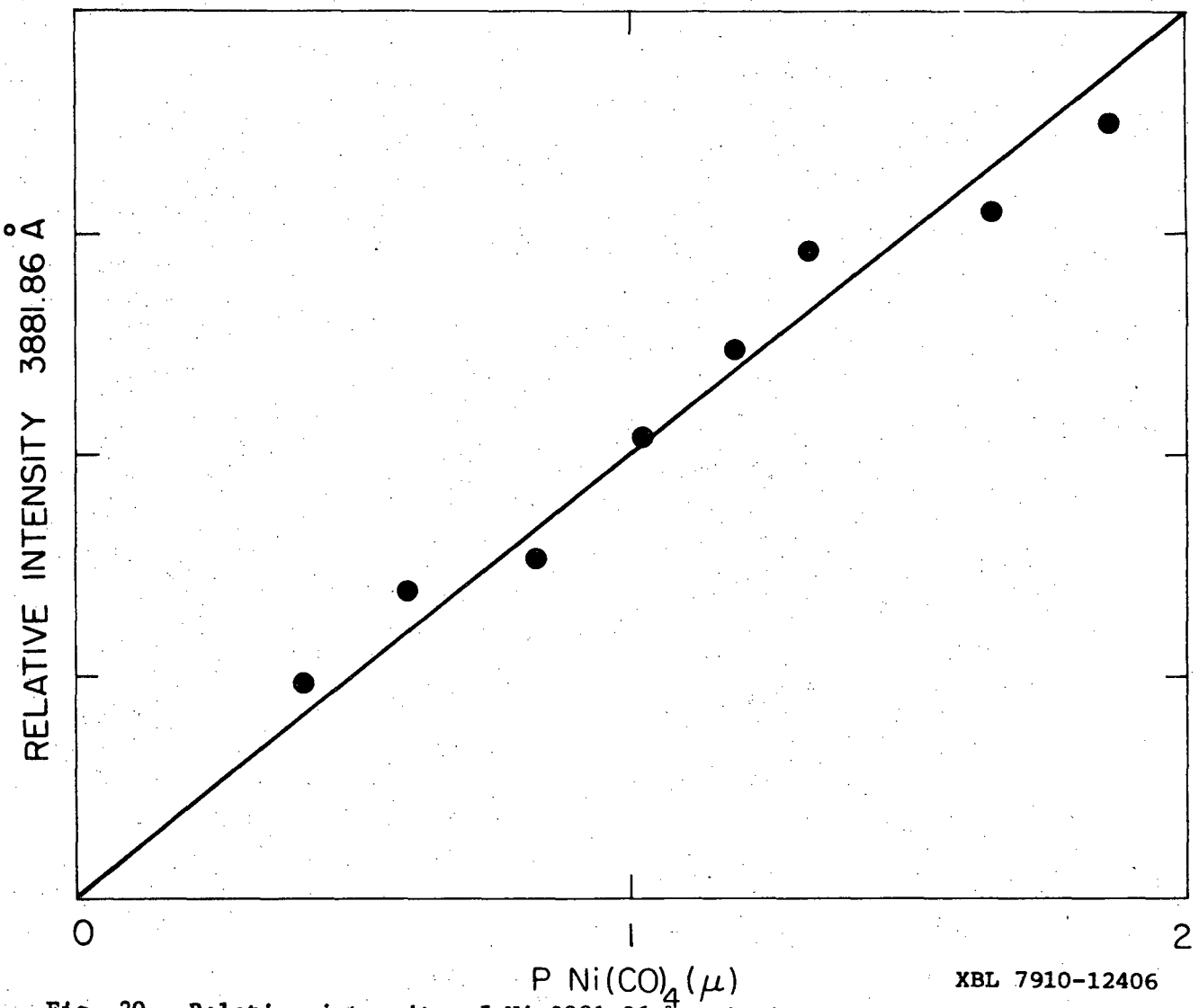

Fig. 20. Relative intensity of Ni 3881.86 Å emission as a function of $Ni(CO)_4$ pressure in the 0-2 μ range. The Ar^* concentration is held constant.

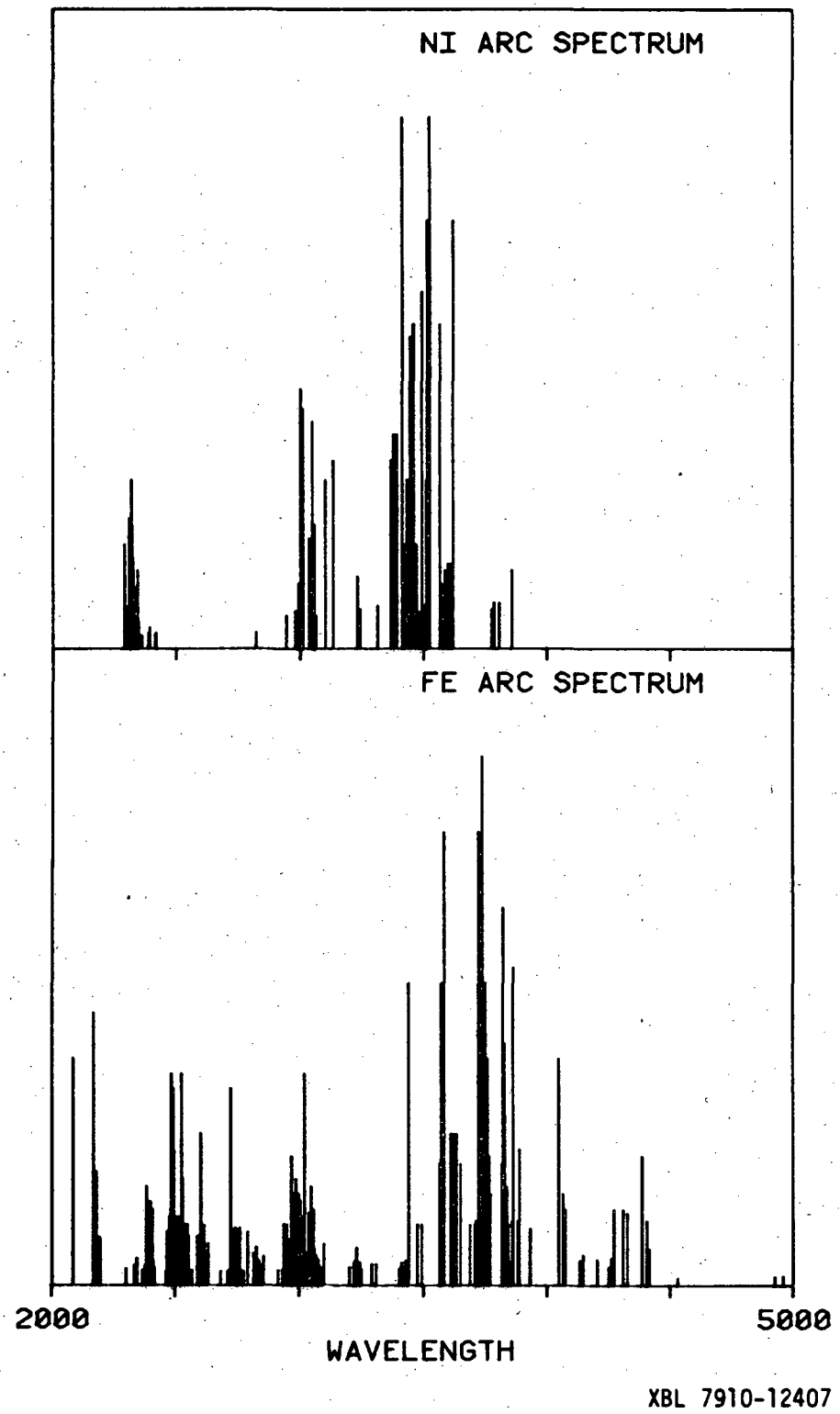

Fig. 21. Simulated pure Ni and Fe arc spectra.

$3d^6 4s\,4p$ configuration (ground state Fe is $3d^6 4s^2$), while in the arc, both this configuration and the $3d^7 4p$ configuration are easily excited. Also, transitions from the highest spin septet terms are extremely strong in the flame, but are very weak in the arc. The converse is true for triplet manifolds, they being strong in the arc but weak in the flame.

Similar data comparing a pure Ni arc and the $Ar^* + Ni(CO)_4$ flame are given in Table VIII. As with Fe, the high-spin manifolds (the quintets in Ni) are extremely strong in the flame, and weak or completely absent in the arc. Not only is the strongest flame line ($z\,^5D_4^o \rightarrow a\,^3F_4$ at 3881.86 Å) not observed in the arc, but as far as is known,[34,35,37,43] this transition has never been reported before in either absorption or emission! Other lines in the flame have not been previously reported; all these lines are listed in Table IX along with their oscillator strengths and spontaneous emission rates as determined by methods described later. Note that the Ni flame emission is not dominated by a single configuration to the extent that the Fe flame is. Terms derived from both the $3d^8 4s4p$ and $3d^9 4p$ (ground state Ni is $3d^8 4s^2$) configurations are important. Thus there are some qualitative differences between the $Ar^* + Ni(CO)_4$ and the $Ar^* + Fe(CO)_5$ flames, but in general, the flame spectra are significantly different from the arc spectra, and emission from low lying states are not spin-differentiated in the flame spectra to the extent they are in the arc spectra.

E. Information From an Atomic Spectrum

What kind of information can be learned from an atomic spectrum? Of course, it can be used to determine energy levels; and fortunately Ni and Fe have been extensively analyzed because of their astrophysical interest. The energy levels are for the most part known quite accurately.

A chemist armed with the intensity and oscillator strength of an atomic line can determine quantities he is interested in: temperatures, relative populations and relative rates. An outline of the important relations follows.

The oscillator strength, $f_{u\ell}$, for spontaneous emission between an upper level, u, and a lower level, ℓ, can be related[36] to the Einstein coefficient for spontaneous emission, $A_{u\ell}$, by

$$A_{u\ell} = 6.67 \times 10^{15} \frac{f_{u\ell}}{\lambda^2} \qquad (1)$$

where λ is the wavelength in Å, $A_{u\ell}$ is in sec^{-1}, and 6.67×10^{15} is a collection of physical constants. The emission intensity of an atomic line (in photons per sec) is given by

$$I = \frac{dN_{u\to\ell}}{dt} = A_{u\ell} N_u \qquad (2)$$

where N_u is the population of the upper state. From equations (1) and (2) it follows that

$$N_u \propto I\lambda^2/f_{u\ell}. \qquad (3)$$

where I is now the counts/sec measured at the photomultiplier tube and is related to I in equation (2) through a proportionality constant.

This expression allows one to calculate the relative population of a given energy level. If one assumes that the population distribution is Maxwell-Boltzmann, such that

$$N_u \propto g_u \exp(-E_u/kT) \tag{4}$$

then it follows that

$$\log_{10}(I\lambda^2/g_u f_{u\ell}) \propto -E_u/2.303\ kT. \tag{5}$$

Thus, if a plot of $\log(I\lambda^2/gf)$ versus E_u for a collection of atomic lines is linear, then the distribution can be characterized by a single parameter, the temperature T. Of course, this electronic temperature may not be equal to any other temperatures (translational, rotational or vibrational) that would exist in a fully equilibrated system.

To calculate the relative rate of formation of a given energy level, E_u, one assumes a steady state in which radiation is the only mode of energy loss by E_u, i.e., one neglects collisional deactivation. The rate of depletion of E_u is proportional to the intensity sum of all lines radiating from this level, i.e.

$$\text{rate of depletion} \propto \sum_j I_{uj} \propto N_u \sum_j A_{uj}. \tag{6}$$

For any single line, $N_u \propto I/A_{u\ell}$, and it follows that the rate of depletion $\propto I\left(\frac{\sum_j A_{uj}}{A_{u\ell}}\right)$. (7)

Under the steady state assumption, the rate of formation of a given level equals its rate of depletion. Thus equation (7) can be used to calculate relative rates of formation for any given atomic line of intensity I, energy E_u, and branching ratio $\Sigma A/A$. Also, application

of equation (7) to an E_u which radiates to more than one lower level provides an internal check on the accuracy of the log(gf) values which are used in the calculations.

F. Populations and Rates

Relative populations and relative rates of formation of various iron and nickel levels can now be calculated. The log(gf) values used in equation (5) and used to determine $A_{u\ell}$ in equation (7) were supplied in part by J. R. Fuhr[37] of the Atomic Transition Probabilities Data Center of the National Bureau of Standards. For Fe, the best log(gf) values are those of Blackwell, et al.[38] Other sources used were the compilations of Bridges and Kornblith[39] and of May, Richter and Wichelmann.[40] Values reported by Corliss and Tech[41] were used as a last resort, and were adjusted using their correction formula[42] and finally readjusting their data in a least squares sense to the more accurate data sources. For Ni, values for lines not tabulated in Fuhr's compilation were taken from Corliss,[43] again correcting to agree with the better data.

Plots of $\log(I\lambda^2/gf)$ versus E_u for the six possible reactant combinations are given in Figs. 22-27.[44] The three plots for nickel are very similar. Each shows a striking difference between the low lying quintet levels (E_u less than 30,000 cm^{-1}), for which the temperatures are 600 to 700 K, and the higher, predominantly triplet, energy levels. Note the value of 3600 K for the higher temperature with Ar^* as compared to the 15,000 to 16,000 K values for Ne^* and He^*. This is because of

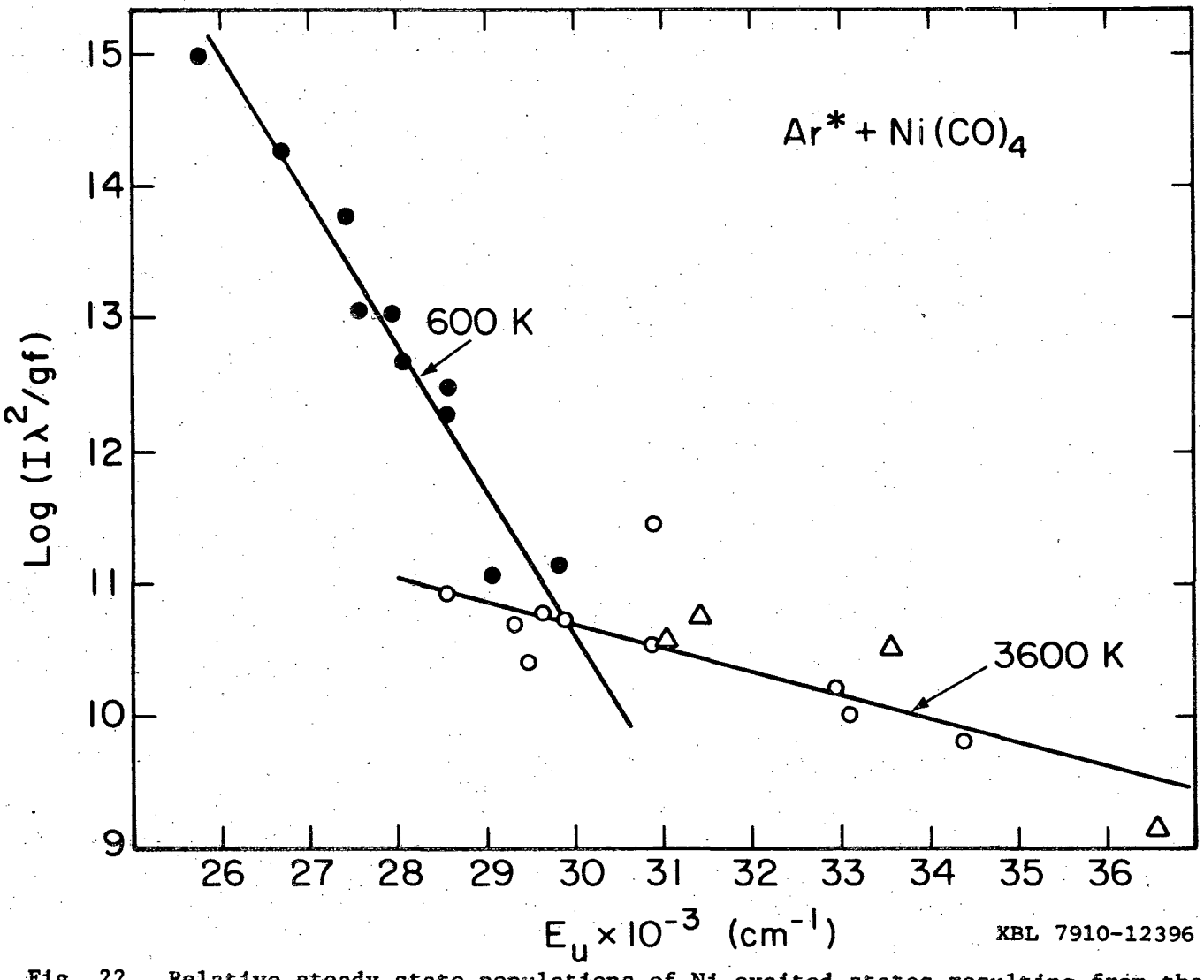

Fig. 22. Relative steady state populations of Ni excited states resulting from the $Ar^* + Ni(CO)_4$ reaction, plotted versus the energy of the emitting state. Spin multiplicities are quintets (solid points), triplets (open circles) and singlets (open triangles).

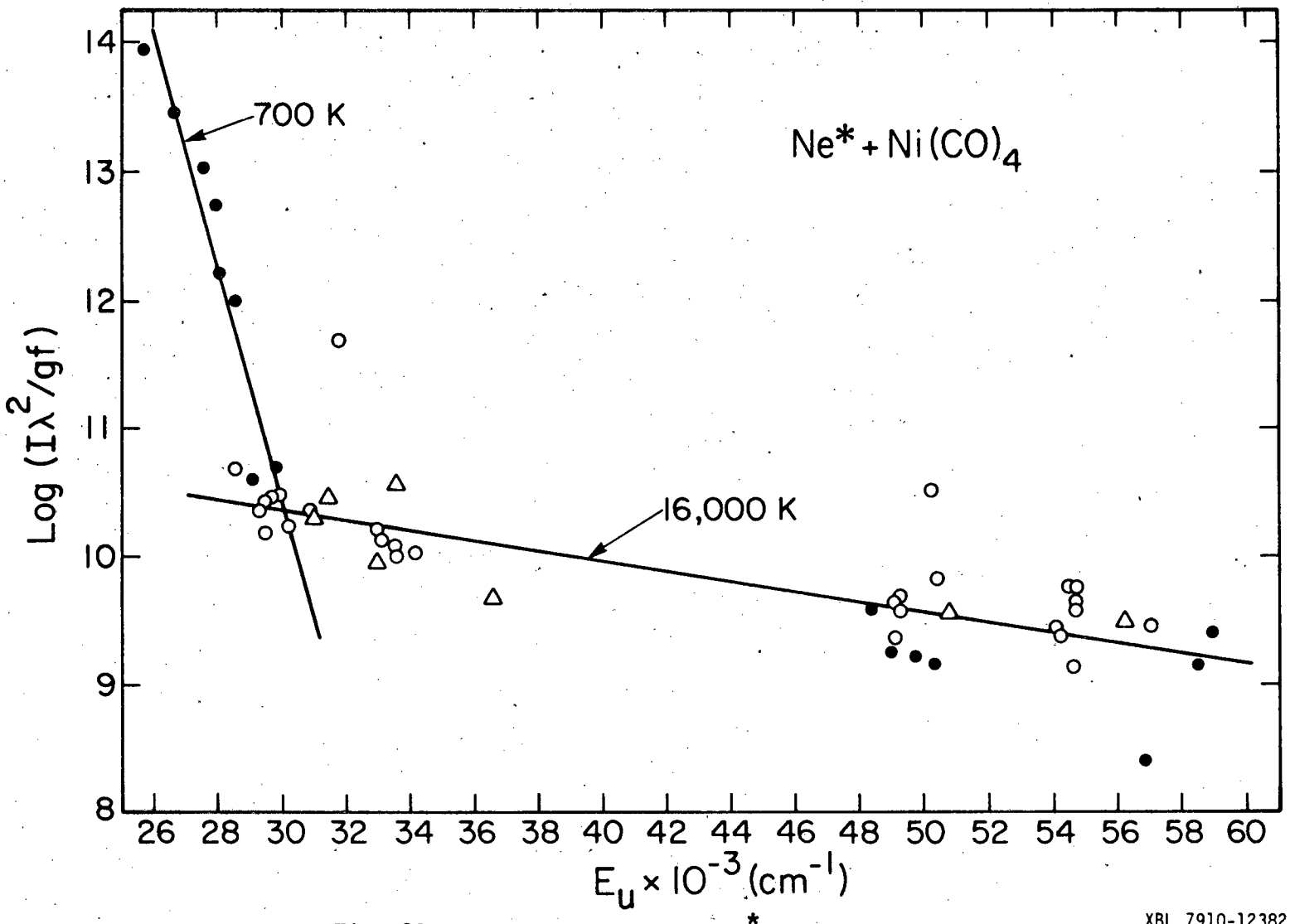

Fig. 23. As Fig. 22, except Ne^{*} + $Ni(CO)_4$.

XBL 7910-12382

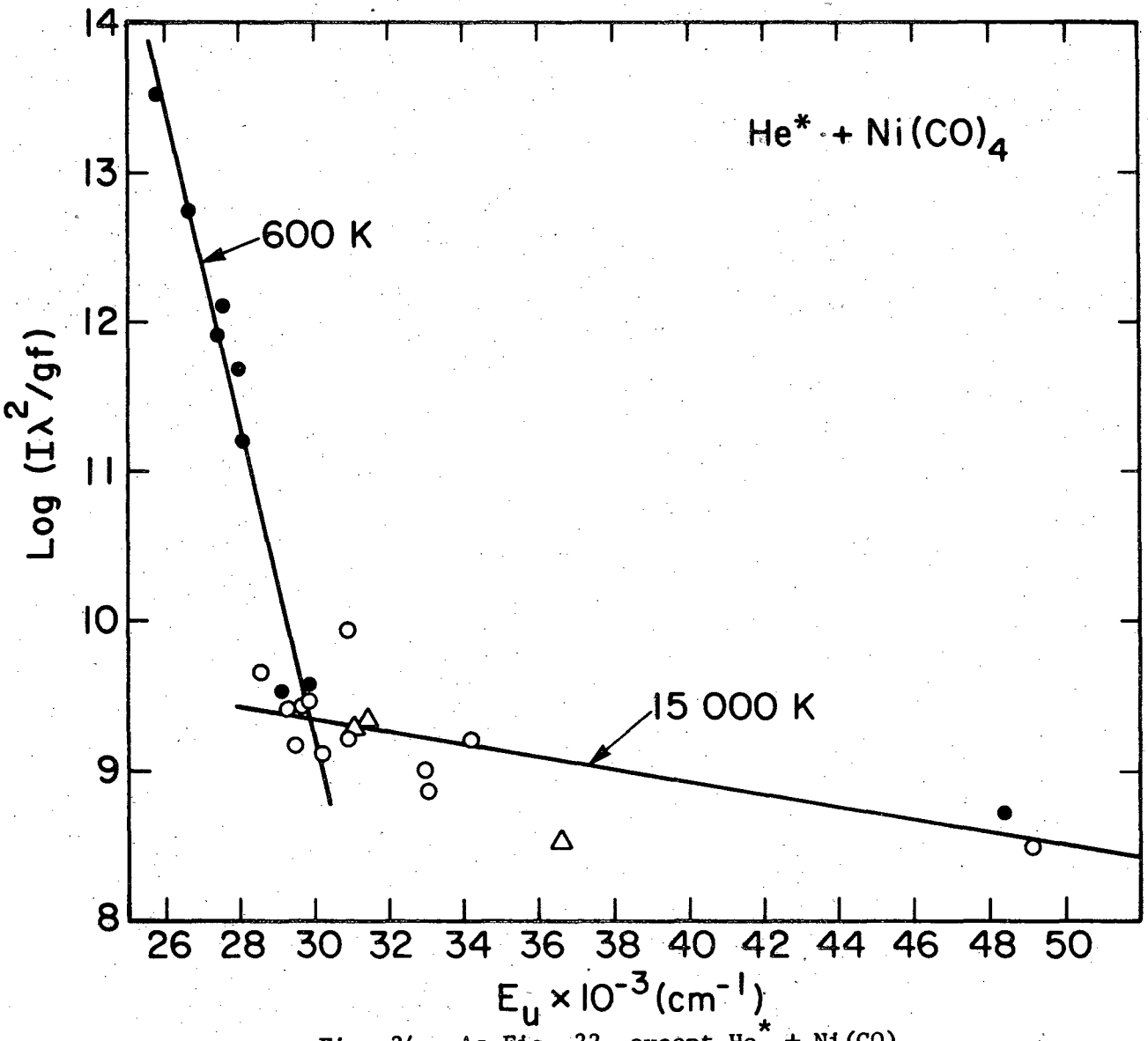

Fig. 24. As Fig. 22, except He^{*} + $Ni(CO)_4$. XBL 7910-12384

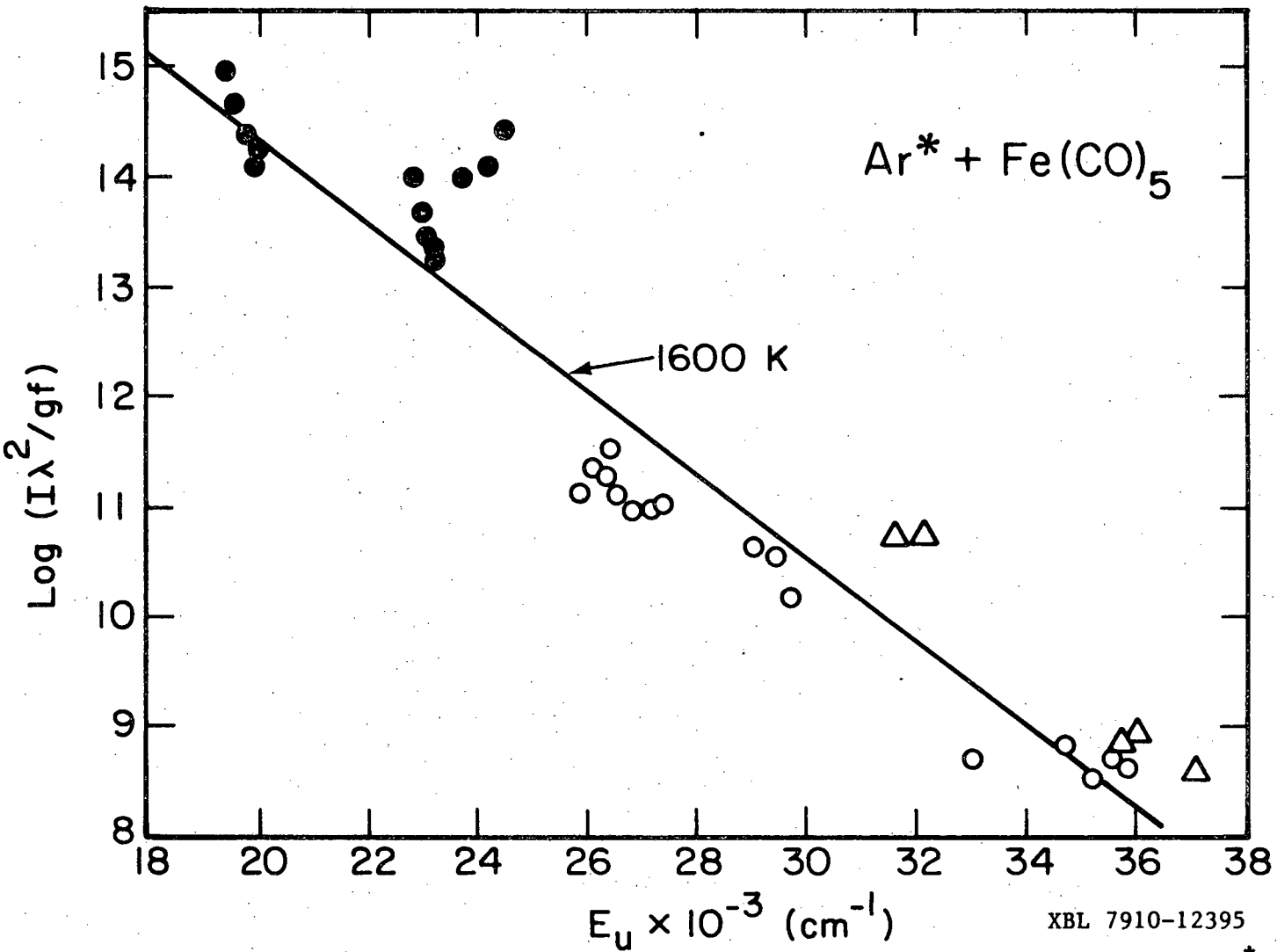

Fig. 25. Relative steady state populations of Fe excited states resulting from the Ar^* + $Fe(CO)_5$ reaction, plotted versus the energy of the emitting state. Spin multiplicities are septets (solid points), quintets (open circles), triplets (open triangles) and singlets (open squares).

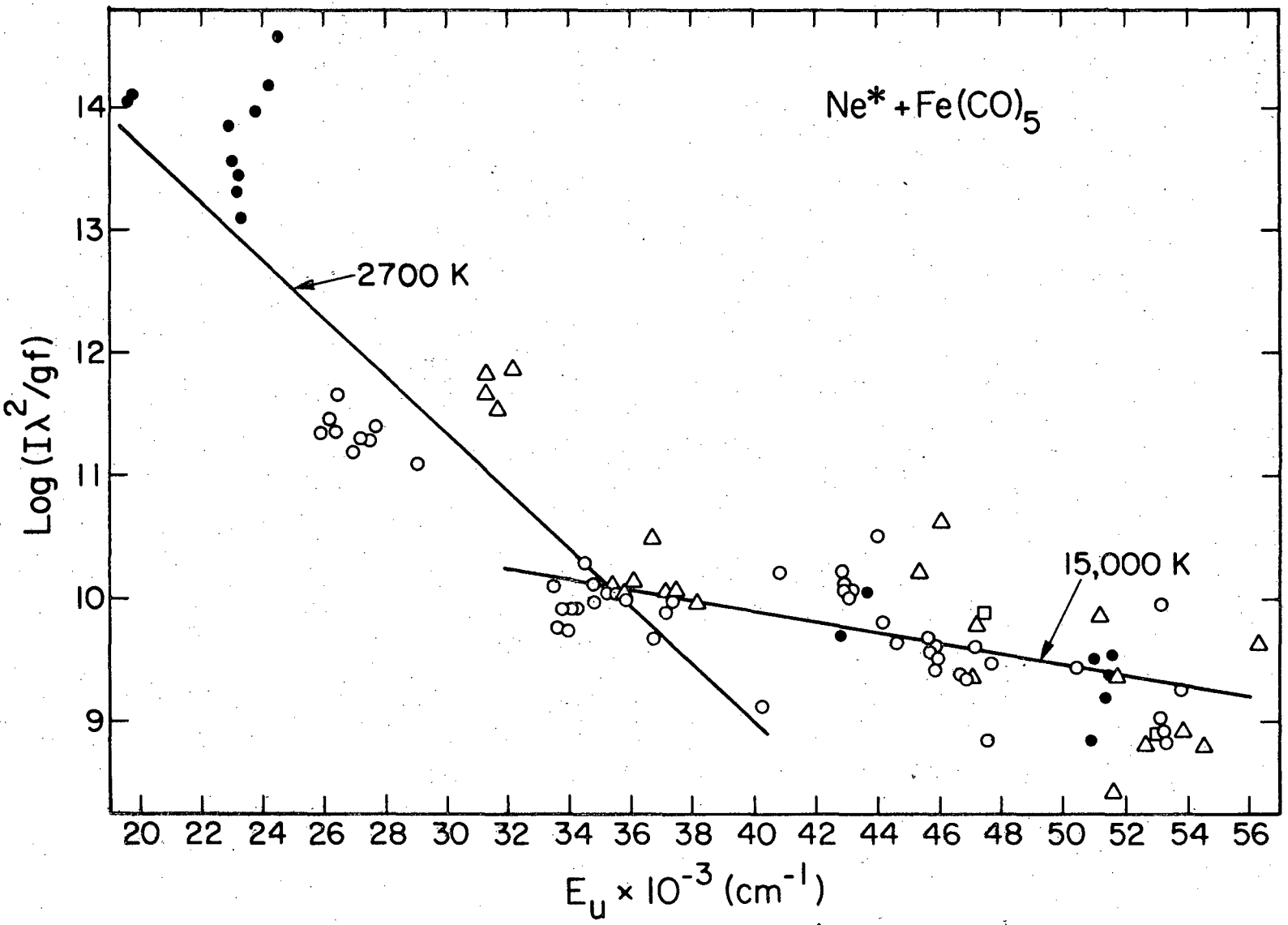

Fig. 26. As Fig. 25, except $Ne^{*} + Fe(CO)_5$.

XBL 7910-12383

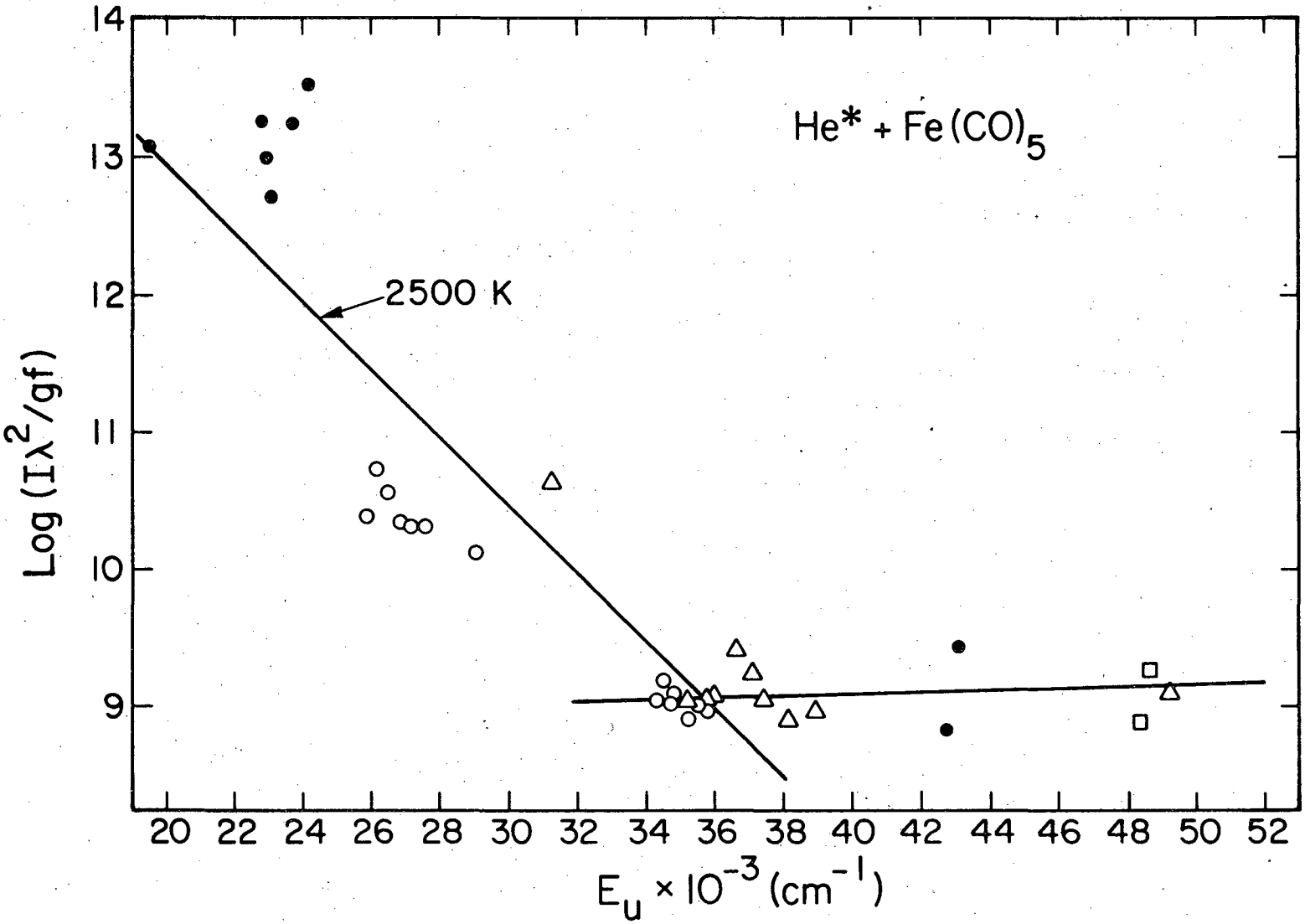

Fig. 27. As Fig. 25, except $He^{*} + Fe(CO)_5$.

the limited energy content of Ar^* and the choice of fitting the higher energy data of Ne^* and He^* to a single temperature. If this family of singlets and triplets with $E_u < 37{,}000\ cm^{-1}$ were treated separately for Ne^* and He^*, results nearer 3600 K would be obtained. Even though the energy of He^* is greater than Ne^*, fewer high energy E_u points appear in the He^* plot. The difference is probably due to the feebleness of the $He^* + Ni(CO)_4$ flame as mentioned in the experimental section, rather than any inherent difference in the reaction mechanism. The log(gf) values for the newly observed Ni lines (Table IX) were obtained from measured intensities and the least squares lines for the low temperature quintet levels.

For Fe, the data were also analyzed in terms of two temperatures, with the break points less obvious than for Ni. The high energy data for He^* actually show a slight negative temperature due to sparse high energy data points.

The temperature analyses yield the conclusion that the carbonyl dissociation is a non-equilibrium process and cannot be simply related to one temperature. In contrast, arc excitation of Fe and Ni is thermal in nature, caused by electrons, and the resulting distributions can be characterized by a single temperature. The Ni and Fe excitations caused by dissociating energized carbonyl molecules is kinetic in nature, which is not surprising since they are caused by a single, bimolecular transfer of energy. The experimental time-scale is the radiative lifetime of the metal atoms, which ranges from 10^{-3} to 10^{-8} sec. Even 10^{-8} sec is much longer than typical intramolecular energy transfer times and bond

breakage times, which are on the order of 10^{-13} sec, a typical vibrational period. One would prefer to think that the dissociation is much faster than any radiative lifetimes, and the metal atom emissions are in disequilibrium due to kinetic features of the energy transfer process. It is possible that the dissociation is much slower, in which collisions with other carbonyls or the background rare gas do not quench the dissociation process.

The appearance of two or more temperatures in steady-state population plots does not necessarily imply two or more dissociation mechanisms. Various atomic states can be formed at the same rate, but develop different populations due to differences in spontaneous emission rates. This is especially evident for the low-energy Ni quintets, where spin selection rules greatly decrease their emission rates. This feature of population plots has not been fully appreciated by prior investigators.

The relative rates of formation of various metal states, as calculated by equation (7), should be more illuminating. These plots for Ar^* and Ne^* with $Ni(CO)_4$ and $Fe(CO)_5$ are shown in Figs. 28-31. In general, the rate of formation of various levels decreases monotonically with increasing energy for both Fe and Ni. The lowest septet levels of Fe show a definite J-dependence in their rate of formation. The higher J values lie lower in energy and are formed at apparently greater rates with increasing J. These levels have long radiative lifetimes ($\sim 10^{-4}$ sec) and the J-dependence may be the result of collisional relaxation to lower fine structure levels (higher J values) of the same term.

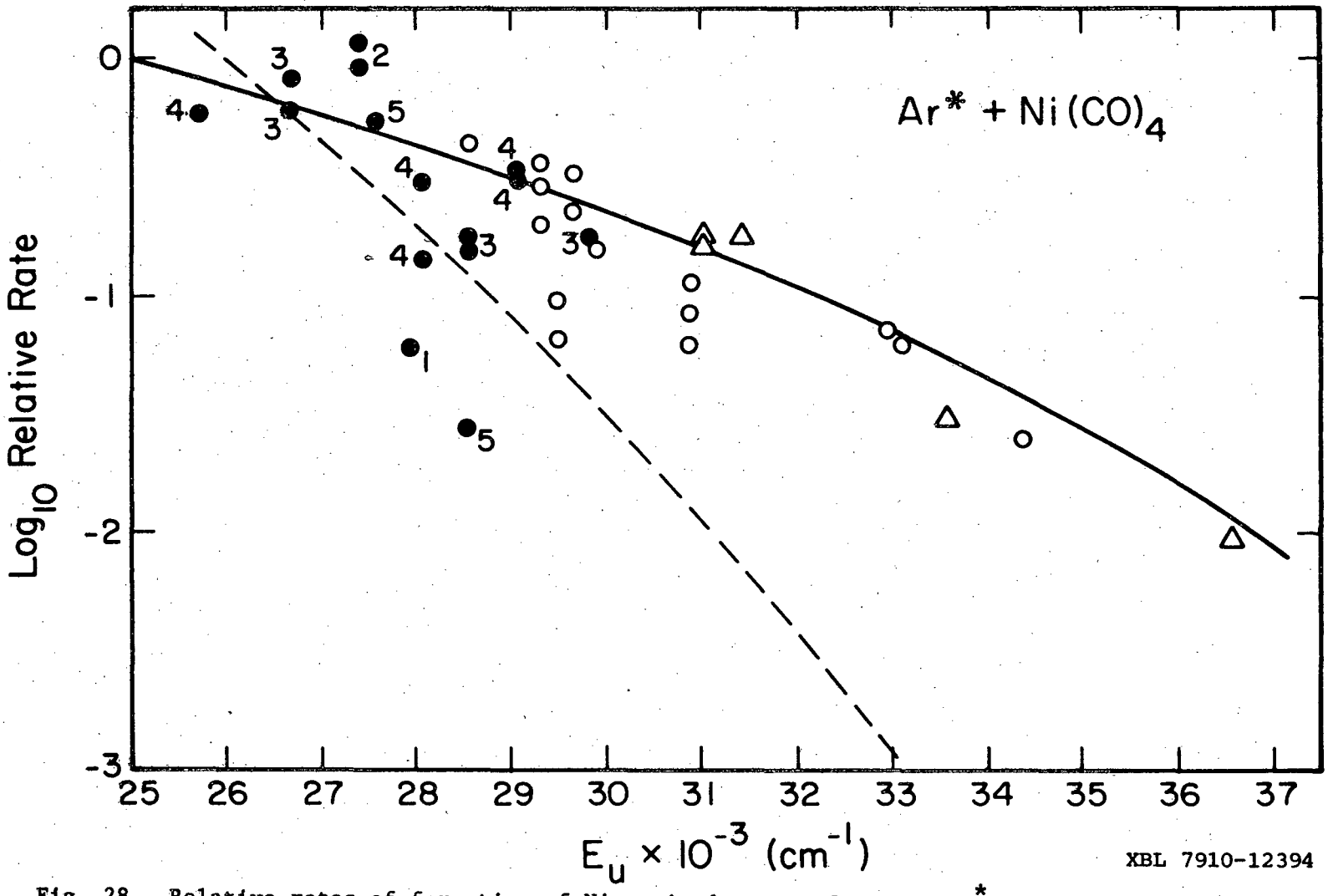

Fig. 28. Relative rates of formation of Ni excited states from the Ar^* + $Ni(CO)_4$ reaction plotted versus the energy of the emitting state. Spin multiplicities are denoted as in Fig. 22. The J values of the low-lying quintet states are also shown. The solid and dashed curves are two predictions of different statistical models described in the text.

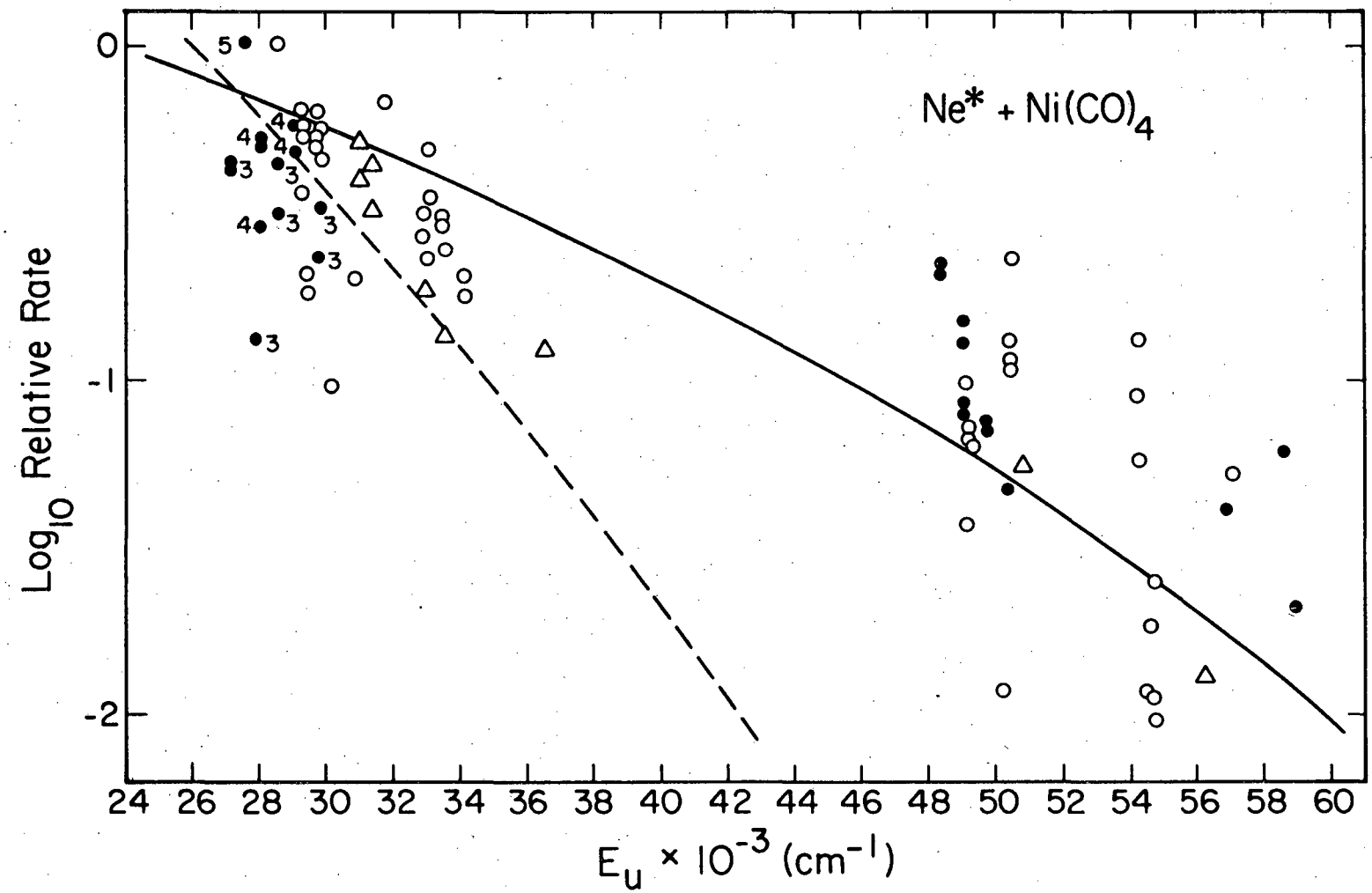

Fig. 29. As Fig. 28, except $Ne^{*} + Ni(CO)_4$.

XBL 7910-12386

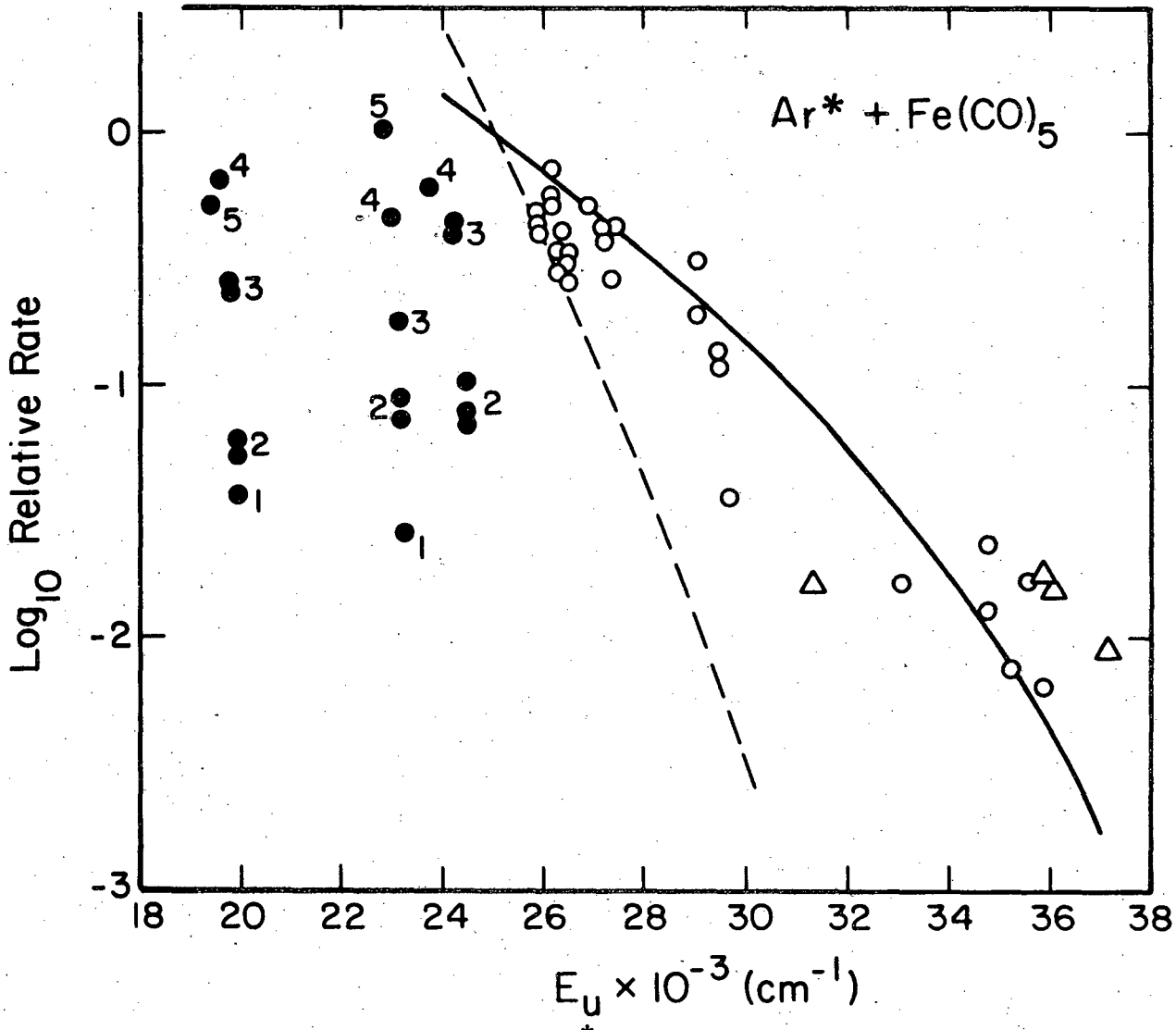

Fig. 30. As Fig. 28, except $Ar^* + Fe(CO)_5$. Spin multiplicities denoted as in Fig. 25. XBL 7910-12393

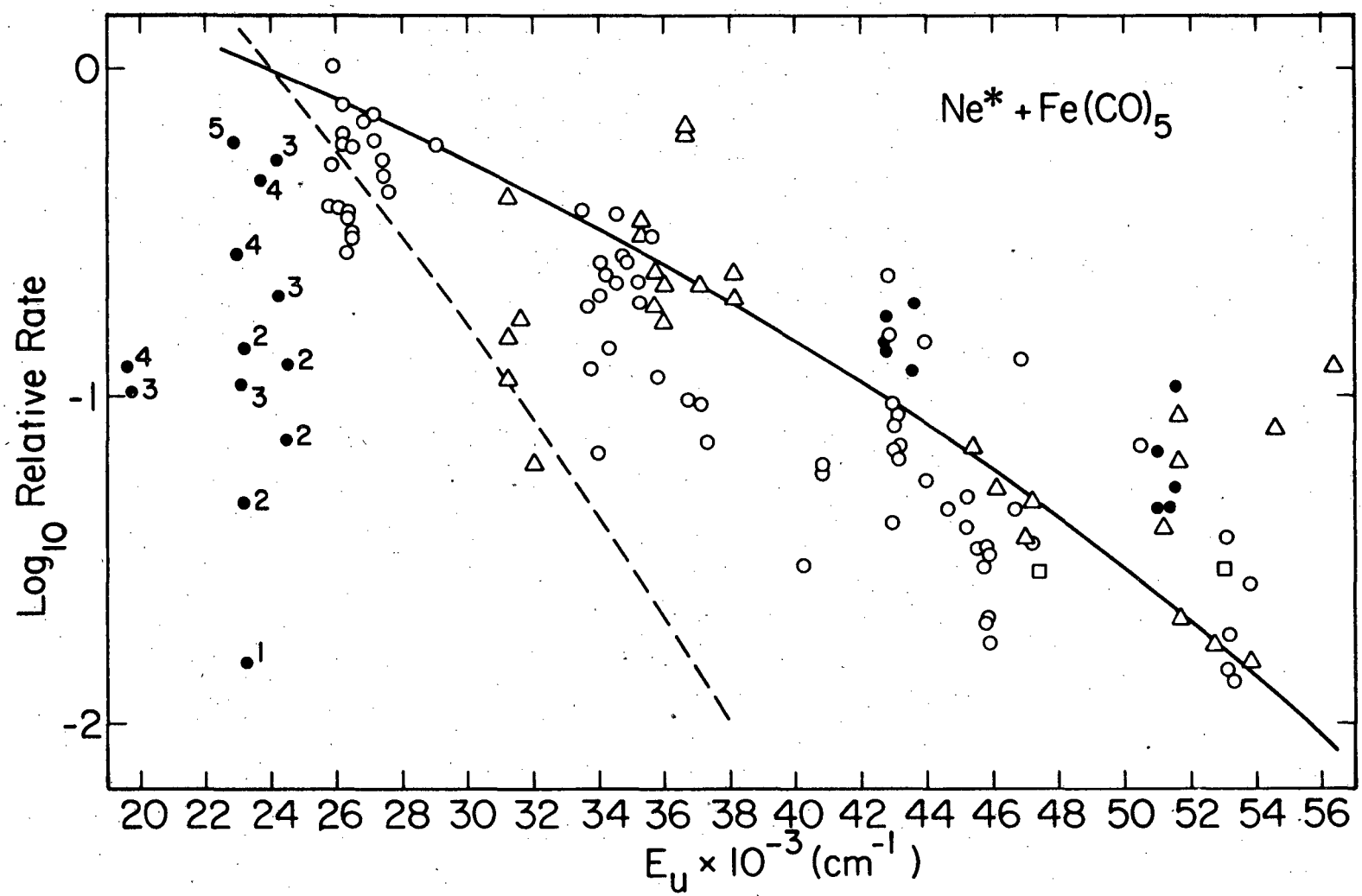

Fig. 31. As Fig. 30, except Ne^{*} + $Fe(CO)_5$.

XBL 7910-12385

A J-changing deactivation cross-section on the order of 1 $Å^2$ would be sufficient for collisional relaxation to compete with radiative relaxation. For ground state (a ^5D) Fe, Callear and Oldman[45] measured a cross-section of 10^{-4} $Å^2$ for the J = 3 to 4 deactivation by Ar. This process is exothermic by 416 cm^{-1}, while the Fe septet levels are spaced by 100 - 200 cm^{-1}. Also, the ground state has a $3d^64s^2$ configuration, while the septets are $3d^64s4p$. A lot of differences exist, but one would not expect the difference to be four orders of magnitude. J-changing collisions with Ar are believed to be unimportant.

Preliminary molecular beam results of Ar^* + $Fe(CO)_5$ by Kobovitch and Krenos[33] yield Fe atom emissions. They were able to resolve a set of four septet transitions and the results are given in Table X. They normalized one of their unresolved quintet set intensities to agree with our data, and in general their overall quintet intensities agree well with ours. Examination of the table indicates our high J $^7F^o$ components are excited much more strongly than the beam results. This could be due to ΔJ scrambling from collisions of the $^7F^o$ atoms with $Fe(CO)_5$. Pressure studies need to be done. More puzzling is the fact that their overall septet intensities are lower than ours. A likely explanation is that since they are using molecular beams with rapid velocities, the long-lived septets may flow past the observation region without radiating, thereby reducing the overall septet intensities.

The low-lying Ni quintet states also show a J-dependence in their rate of formation, but the effect is not as marked.

Absolute bimolecular rate constants for the stronger emitting states of Fe in the reaction $Ar^* + Fe(CO)_5$ have been measured. The method consists of comparing intensities to that of the 7602 Å Kr line. The method is described in Appendix B. The concentrations of Kr and $Fe(CO)_5$ were measured by direct pressure measurements. The calculated rate constants are listed in Table XI. The rate constants are in the range 5×10^{-13} to 5×10^{-15} cm^3 $molecule^{-1}$ sec^{-1}, and the sum yields the partial quenching rate constant for $Ar^* + Fe(CO)_5$; and is estimated to be 6×10^{-12} cm^3 $molecule^{-1}$ sec^{-1}. This rate constant does not include production of dark products such as ground state atoms.

G. A Statistical Model

A statistical model has been developed that successfully predicts the observed rate distributions in Ni and Fe. During the collision, the metastable rare gas atom imparts its energy, E^*, to the metal carbonyl and departs. The energy is randomized within the carbonyl and when an energy greater than the metal-carbon bond energy is located in any of those bonds, a carbon monoxide molecule breaks loose. The energy available for product electronic, vibrational, rotational, and translational excitation, E_a, is given by

$$E_a = E^* - E_D \tag{8}$$

where E_D is the energy required to break the carbonyl into the metal atom and the free CO molecules.

Subtracting the electronic excitation of the metal atom, E_{M^*} yields the energy available to the various vibrational, rotational and translational modes of the products, E, given by

$$E = E_a - E_M^* \tag{9}$$

It is now postulated that the rate of formation of a certain metal atom state M^* is given by

$$\text{rate of formation of } M^* \propto \rho(E) \tag{10}$$

where $\rho(E)$ is the density of states for the appropriate degrees of freedom of the products at the energy E.

Equation (10) requires a little discussion. E_a is divided between electronic excitation of the metal atom, E_M^*, and all other excitations, E. The rate of excitation of the metal atom is statistically more probable if there are more states in which to accomodate E, hence the rate should depend on the density of states. A direct proportionality is postulated.

How is $\rho(E)$ calculated? The method of attack using partition functions and Laplace transforms, is reviewed by Forst.[46] Some of the useful relations are outlined below.

The quantum mechanical partition function Q, is given by

$$Q = \sum_E g(E)\, e^{-E/kT} \tag{11}$$

where g(E) is the degeneracy of the state of energy E. Also

$$g(E) = \rho(E)\, dE \tag{12}$$

where $\rho(E)$ is density of states per unit energy at energy E. E is always taken to be the energy in excess of the zero-point energy.

Substituting Eq. (12) into Eq. (11) and changing the sum to an integral yields the semiclassical partition function

$$Q = \int_0^\infty \rho(E)\, e^{-E/kT}\, dE. \tag{13}$$

$\rho(E)$ is assumed to be a smooth, continuous function of E. Of course, in actuality it isn't, and the approximation becomes less valid as the energy spacings increase.

Substituting $s = 1/kT$ into Eq. (13) yields

$$Q = \int_0^\infty \rho(E)\, e^{-Es}\, dE \equiv L\{\rho(E)\} \tag{14}$$

The partition function is seen to be the Laplace transform of the density of states. The inverse operation also holds true

$$\rho(E) = L^{-1}\{Q\} \tag{15}$$

i.e. the density of states is given by the inverse Laplace transorm of the semiclassical partition function.

Suppose there are two independent systems, 1 and 2. Then it holds true that

$$Q_1(s) = L\{\rho_1(E)\} \qquad Q_2(s) = L\{\rho_2(E)\}. \tag{16}$$

The convolution theorem then states that

$$\begin{aligned} L^{-1}\{Q_1(s)Q_2(s)\} &= \int_0^E \rho_1(x)\rho_2(E-x)\,dx \qquad \text{or} \\ &= \int_0^E \rho_1(E-x)\rho_2(x)\,dx. \end{aligned} \tag{17}$$

But $Q_1(s)Q_2(s) = Q_{1,2}(s)$, the partition function for the combined system; and $L^{-1}\{Q_{1,2}(s)\}$ is $\rho_{1,2}(E)$, the density of states for the combined system. Therefore

$$\rho_{1,2}(E) = \int_0^E \rho_1(x)\rho_2(E-x)\,dx \qquad \text{or}$$
$$= \int_0^E \rho_1(E-x)\rho_2(x)\,dx \tag{18}$$

i.e., if the partition functions are separable, the density of states of the combined system is related by convolution to the densities of states of the separated systems.

Now the relevant degrees of freedom and their corresponding partition functions can be chosen. Then $\rho(E)$ for the system is easily calculated with the formulas above.

The most logical first choice is that all degrees of freedom are available to the products. The available degrees of freedom and their partition functions are

(i) 3 translational degrees of freedom to the metal atom

$$q_t = \frac{(2\pi mkT)^{3/2}V}{h^3} = K_1(kT)^{3/2} = K_1 s^{-3/2}. \tag{19}$$

(ii) 3 translational degrees of freedom to each CO

$$q_t = K_2 s^{-3/2}. \tag{20}$$

(iii) The CO's can vibrate as harmonic oscillators (anharmonicity will be put into the theory later)

$$q_v = \frac{kT}{h\nu_o} = K_3 s^{-1}. \tag{21}$$

This is just the semiclassical partition function found by changing the sum in equation (4) to an integral.

(iv) The CO's can rotate in 3 dimensions

$$q_r = \frac{8\pi^2 IkT}{h^2} = K_4 s^{-1}. \tag{22}$$

(v) CO is not electronically excited or dissociated.

All the degrees of freedom are treated as being independent, thus the total partition function for the system is just the product of the partition functions from the individual parts. For $Ni(CO)_4$

$$\begin{aligned} q_{total} &= (K_1 s^{-3/2})(K_2 s^{-3/2})^4 (K_3 s^{-1})^4 (K_4 s^{-1})^4 \\ &= K_5 s^{-15.5}. \end{aligned} \tag{23}$$

A useful relation is that $L^{-1}\{s^{-[n+(1/2)]}\} = \frac{2^n E^{n-(1/2)}}{1\cdot3\cdot5\cdots(2n-1)\sqrt{\pi}} (n=1,2,\cdots)$.

Thus
$$\begin{aligned} \rho_{total} &= L^{-1}\{q_{total}\} \\ &= L^{-1}\{K_5 s^{-15.5}\} \\ &= K_5 L^{-1}\{s^{-15.5}\} \\ &= \frac{K_5 \cdot 2^{15} E^{14.5}}{1\cdot3\cdot5\cdots 27\cdot29\cdot\sqrt{\pi}} \\ &= K_6 E^{14.5} \end{aligned} \tag{24}$$

Or
$$\boxed{\rho(E) \propto E^{14.5} \qquad Ni(CO)_4} \tag{25}$$

Similarly for $Fe(CO)_5$

$$q_{total} = (K_1' s^{-3/2})(K_2 s^{-3/2})^5(K_3 s^{-1})^5(K_4 s^{-1})^5$$

$$= K_5' s^{-19}. \qquad (26)$$

$L^{-1}\{s^{-n}\} = \frac{E^{n-1}}{(n-1)!}$ $(n = 1,2,\cdots)$, therefore

$$\rho_{total} = L^{-1}\{K_5' s^{-19}\}$$

$$= \frac{K_5' E^{18}}{18!}$$

$$= K_6' E^{18}. \qquad (27)$$

Or $\boxed{\rho(E) \propto E^{18} \quad Fe(CO)_5}$.

The derivations of $\rho(E)$ can be altered to include anharmonicity in the CO vibrations. The CO vibrational constants given by Herzberg[26] are used to calculate the vibrational energies. $\rho(E)$ at the energy between two vibrational levels is simply the reciprocal of the energy difference between these two levels; and to bring $\rho(E)$ into more convenient numbers the result is multiplied by 2500 so that $\rho(E)$ is defined as the number of vibrational states per 2500 cm^{-1}. The results are given in Table XII.

A simple expression for $\rho_v(E)$ that was found to work well was

$$\rho_v(E) = be^{mE} \qquad (28)$$

The numerical $\rho_v(E)$ from Table XII is least squares fitted to the above equation. The results of several fits are shown in Table XIII.

From $\rho_v(E)$, the anharmonic partition function can be calculated

$$q_v = L\{\rho_v(E)\}$$

$$= bL\{e^{mE}\}$$

$$= \frac{b}{s - m} . \tag{29}$$

The partition functions can be multiplied as before but the inverse Laplace transform is not known. The better way to get $\rho_{total}(E)$ seems to be to get $\rho_{translation\text{-}rotation}$ and $\rho_{vibration}$ separately, and obtain ρ_{total} by convolution. For $Ni(CO)_4$

$$q_{trans\text{-}rot} = (K_1 s^{-3/2}) (K_2 s^{-3/2})^4 (K_4 s^{-1})^4$$

$$= K_5 s^{-11.5} \tag{30}$$

$$\rho_{trans\text{-}rot}(E) = L^{-1} \{K_5 s^{-11.5}\}$$

$$= K_6 E^{10.5} \tag{31}$$

$$q_{vib} = b^4 \left(\frac{1}{s-m}\right)^4 \tag{32}$$

$$\rho_{vib}(E) = L^{-1} \left\{b^4 \left(\frac{1}{s-m}\right)^4\right\}$$

$$= K_7 E^3 e^{mE} . \tag{33}$$

Now the convolution integral can be set up

$$\rho_{total}(E) = \int_o^E \rho_{vib}(E-x) \rho_{trans\text{-}rot}(x) \, dx \tag{34}$$

$$= \int_o^E K_7 (E-x)^3 e^{m(E-x)} K_6 x^{10.5} \, dx. \tag{35}$$

Expand $(E-x)^3 = E^3 - 3E^2x + 3Ex^2 - x^3$ and since $e^{m(E-x)} = e^{mE}e^{-mx}$, e^{mE} can be taken out of the integral

$$\rho(E) = K_6K_7\, e^{mE}\left[E^3\int_o^E e^{-mx}\, x^{10.5}dx - 3E^2\int_o^E e^{-mx}\, x^{11.5}dx + 3E\int_o^E e^{-mx}\, x^{12.5}dx - \int_o^E e^{-mx}\, x^{13.5}dx\right]. \tag{36}$$

Expand e^{-mx} in a power series and keep the first three terms, i.e. $e^{-mx} = 1 - mx + \frac{m^2x^2}{2}$

$$\rho(E) = K_6K_7\, e^{mE}\left[E^3\int_o^E x^{10.5}dx - E^3m\int_o^E x^{11.5}dx + \frac{E^3m^2}{2}\int_o^E x^{12.5}dx - 3E^2\int_o^E x^{11.5}dx + 3E^2m\int_o^E x^{12.5}dx - \frac{3E^2m^2}{2}\int_o^E x^{13.5}dx + 3E\int_o^E x^{12.5}dx - 3Em\int_o^E x^{13.5}dx + \frac{3Em^2}{2}\int_o^E x^{14.5}dx - \int_o^E x^{13.5}dx + m\int_o^E x^{14.5}dx - \frac{m^2}{2}\int_o^E x^{15.5}dx\right]. \tag{37}$$

$$\rho(E) = K_6K_7\, e^{mE}\left[\frac{E^{14.5}}{11.5} - \frac{mE^{15.5}}{12.5} + \frac{m^2E^{16.5}}{27} - \frac{3E^{14.5}}{12.5} + \frac{3mE^{15.5}}{13.5} - \frac{3m^2E^{16.5}}{29} + \frac{3E^{14.5}}{13.5} - \frac{3mE^{15.5}}{14.5} + \frac{3m^2E^{16.5}}{31} - \frac{E^{14.5}}{14.5} + \frac{mE^{15.5}}{15.5} - \frac{m^2E^{16.5}}{33}\right]. \tag{38}$$

$$\rho(E) = K_6K_7\, e^{mE}\left[2.132\times10^{-4}E^{14.5} - m\cdot1.582\times10^{-4}E^{15.5} + m^2\cdot5.992\times10^{-5}E^{16.5}\right]. \tag{39}$$

$$\boxed{\rho(E) \propto e^{mE}\,[E^{14.5} - 0.7420mE^{15.5} + 0.2811m^2E^{16.5}]} \tag{40}$$

$Ni(CO)_4$ All degrees of freedom open

For $Fe(CO)_5$

$$q_{trans\text{-}rot} = (K_1' \, s^{-3/2})(K_2 \, s^{-3/2})(K_4 \, s^{-1})^5$$

$$= K_5' s^{-14}. \tag{41}$$

$$\rho_{trans\text{-}rot}(E) = L^{-1} \{K_5' \, s^{-14}\}$$

$$= K_6' \, E^{13}. \tag{42}$$

$$q_{vib} = b^5 \left(\frac{1}{s-m}\right)^5. \tag{43}$$

$$\rho_{vib}(E) = L^{-1} \left\{b^5 \left(\frac{1}{s-m}\right)^5\right\}$$

$$= K_7' \, E^4 \, e^{mE}. \tag{44}$$

Again, the convolution integral can be set up

$$\rho_{total}(E) = \int_o^E \rho_{vib}(E-x) \, \rho_{trans\text{-}rot}(x) \, dx \tag{45}$$

$$= \int_o^E K_7' \, (E-x)^4 \, e^{m(E-x)} \, K_6' \, x^{14} \, dx. \tag{46}$$

Expand $(E-x)^4 = E^4 - 4E^3x + 6E^2x^2 - 4E\,x^3 + x^4$ and take e^{mE} out of the integral

$$\rho(E) = K_6'K_7' \, e^{mE} \left[E^4 \int_o^E e^{-mx} x^{13} dx - 4E^3 \int_o^E e^{-mx} x^{14} dx \right.$$

$$\left. + 6E^2 \int_o^E e^{-mx} \, x^{15} dx - 4E \int_o^E e^{-mx} \, x^{16} dx + \int_o^E e^{-mx} \, x^{17} dx\right]. \tag{47}$$

Again expand e^{-mx} out to three terms

$$\rho(E) = K_6'K_7' \, e^{mE} \left[E^4 \int_o^E x^{13}dx - E^4 m \int_o^E x^{14}dx + \frac{E^4 m^2}{2} x^{15}dx \right.$$
$$- 4E^3 \int_o^E x^{14}dx + 4E^3 m \int_o^E x^{15}dx - \frac{4E^3 m^2}{2} \int_o^E x^{16}dx$$
$$+ 6E^2 \int_o^E x^{15}dx - 6E^2 m \int_o^E x^{16}dx + \frac{6E^2 m^2}{2} \int_o^E x^{17}dx$$
$$- 4E \int_o^E x^{16}dx + 4Em \int_o^E x^{17}dx - \frac{4Em^2}{2} \int_o^E x^{18}dx$$
$$\left. + \int_o^E x^{17}dx - m \int_o^E x^{18}dx + \frac{m^2}{2} \int_o^E x^{19}dx \right]. \qquad (48)$$

$$\rho(E) = K_6'K_7' \, e^{mE} \left[\frac{E^{18}}{14} - \frac{mE^{19}}{15} + \frac{m^2E^{20}}{32} - \frac{4E^{18}}{15} + \frac{m4E^{19}}{16} - \frac{m^24E^{20}}{34} \right.$$
$$+ \frac{6E^{18}}{16} - \frac{m6E^{19}}{17} + \frac{m^26E^{20}}{36} - \frac{4E^{18}}{17} + \frac{m4E^{19}}{18} - \frac{m^2E^{20}}{38}$$
$$\left. + \frac{E^{18}}{18} - \frac{mE^{19}}{19} + \frac{m^2E^{20}}{40} \right]. \qquad (49)$$

$$\rho(E) = K_6'K_7' \, e^{mE} \left[2.344\times10^{-5}E^{18} - m\cdot 1.720\times10^{-5}E^{19} + m^2 \cdot 6.450\times10^{-6}E^{20} \right]. \qquad (50)$$

$$\boxed{\rho(E) \propto e^{mE} \left[E^{18} - 0.7369mE^{19} + 0.2763m^2E^{20} \right]}$$
$$\boxed{Fe(CO)_5 \quad \text{All degrees of freedom open}} \qquad (51)$$

Equations (40) and (51), then, are the densities of states with anharmonic oscillators and all degrees of freedom. With the heats of formation for $Ni(CO)_4$[47] and $Fe(CO)_5$,[48] E_D can be calculated for the following processes:

$Ni(CO)_4(g) \rightarrow Ni(g) + 4CO(g)$ $\quad E_D = \Delta H^\circ_{298} = 140.8$ kcal/mole $= 49{,}200$ cm^{-1}.

$Fe(CO)_5(g) \rightarrow Fe(g) + 5CO(g)$ $\quad E_D = \Delta H^\circ_{298} = 138.5$ kcal/mole $= 48{,}400$ cm^{-1}.

The metastable rare gas energies are (See Table I.)

$$\text{Ar } (^3P_2) = 93144 \text{ cm}^{-1}$$
$$\text{Ne } (^3P_2) = 134043 \text{ cm}^{-1}$$
$$\text{He } (2^3S) = 159850 \text{ cm}^{-1}$$

E_a, as defined by equation (8), can be calculated for the six possible reactant pairs

$Ar^* + Ni(CO)_4$	$E_a = 43900 \text{ cm}^{-1}$
$Ne^* + Ni(CO)_4$	$E_a = 84800 \text{ cm}^{-1}$
$He^* + Ni(CO)_4$	$E_a = 110600 \text{ cm}^{-1}$
$Ar^* + Fe(CO)_5$	$E_a = 44700 \text{ cm}^{-1}$
$Ne^* + Fe(CO)_5$	$E_a = 85600 \text{ cm}^{-1}$
$He^* + Fe(CO)_5$	$E_a = 111400 \text{ cm}^{-1}$

Since the He^* rates were not plotted due to lack of sufficient high energy data, we will concentrate on Ar^* and Ne^*. For $Ar^* + Ni(CO)_4$ and $Ar^* + Fe(CO)_5$, E_a is about 44,000 cm^{-1}. Therefore the fit of $\rho_{vib}(E) = be^{mE}$ up to 50,000 cm^{-1} is used (see Table XIII) with $m = 7.94\times10^{-6}$. For $Ne^* + Ni(CO)_4$, the lowest experimentally observed Ni excitations were around 26,000 cm^{-1}, so that with $E_a = 85{,}000 \text{ cm}^{-1}$ the maximum CO excitation can be up to 59,000 cm^{-1}. Therefore the fit up to 60,000 cm^{-1} was used with $m = 8.70\times10^{-6}$. With $Ne^* + Ni(CO)_4$, the fit up to 83,000 cm^{-1} was used with $m = 1.30\times10^{-5}$ because Fe excitations as low as 19,000 cm^{-1} were observed.

Equation (40) is plotted as a function of E_M^* (i.e. E_u) as the dashed lines in Figs. 28 and 29 for $Ni(CO)_4$. These curves do not fit

the experimental $Ar^* + Ni(CO)_4$ and $Ne^* + Ni(CO)_4$ nickel atom rates well at all, falling off much to rapidly. Likewise, equation (51) is plotted in Figs. 30 and 31 for $Fe(CO)_5$, the dashed lines also not agreeing with experiment.

It is obvious that too many degrees of freedom are allowed to consolidate the energy E in the fragment products. Therefore a mechanism with fewer degrees of freedom was devised, and as will be seen, is also much more physically satisfying.

The assumptions used in calculating $\rho(E)$ for the new model are:

(i) Again, the CO molecules are treated as anharmonic oscillators in the same fashion as before.

(ii) CO is not electronically excited or dissociated, as before.

(iii) The exiting CO molecules are treated as <u>one-dimensional</u> translators. This is equivalent to saying that either the ligands dissociate simultaneously along the equilibrium metal-ligand bond direction or else they dissociate sequentially, but rapidly, without experiencing any rearrangment. In this respect, the model resembles an impulsive dissociation mechanism.

(iv) No torque can be exerted on the CO fragments if they dissociate radially. Hence, no rotational excitation of the CO fragments is assumed to occur.

(v) Finally, it is assumed that there is no translational excitation of the metal atom. This is insured by momentum conservation if all metal-ligand bond ruptures impart equal impulses to the metal.

With the above assumptions the appropriate partition functions are:

(i) For one-dimensional translators

$$q_t = \frac{a\sqrt{2\pi mkT}}{h} = K_1 s^{-1/2}. \tag{52}$$

(ii) For anharmonic CO molecules, as before

$$q_v = \frac{b}{s-m}. \tag{53}$$

For $Ni(CO)_4$

$$q_t = (K_1 s^{-1/2})^4$$

$$= K_2 s^{-2}. \tag{54}$$

$$\rho_t(E) = L^{-1}\{K_2 s^{-2}\}$$

$$= K_2 E. \tag{55}$$

$$q_v = b^4 \left(\frac{1}{s-m}\right)^4. \tag{56}$$

$$\rho_v(E) = L^{-1}\left\{b^4\left(\frac{1}{s-m}\right)^4\right\}$$

$$= K_3 E^3 e^{mE}. \tag{57}$$

The convolution integral can now be set up

$$\rho_{total}(E) = \int_o^E \rho_t(E-x)\rho_v(x)dx. \tag{58}$$

$$= \int_o^E K_2(E-x)K_3 x^3 e^{mx}dx. \tag{59}$$

$$= K_2K_3\left[E\int_o^E x^3 e^{mx}dx - \int_o^E x^4 e^{mx}dx\right]. \tag{60}$$

Expanding $e^{mx} = 1 + mx + \frac{m^2x^2}{2}$

$$\rho(E) = K_2K_3\left[E\int_o^E x^3dx + Em\int_o^E x^4dx + \frac{Em^2}{2}\int_o^E x^5dx - \int_o^E x_4dx - m\int_o^E x^5dx - \frac{m^2}{2}\int_o^E x^6dx\right]. \quad (61)$$

$$\rho(E) = K_2K_3\,[0.05\,E^5 + m \cdot 3.333\times10^{-2}\,E^6 + m^2 \cdot 1.190\times10^{-2}E^7]. \quad (62)$$

$$\rho(E) \propto E^5 + 0.6667\ mE^6 + 0.2381\ m^2E^7 \quad (63)$$

$Ni(CO)_4$ Restricted degrees of freedom

For $Fe(CO)_5$

$$q_t = (K_1\ s^{-1/2})^5$$

$$= K_2'\ s^{-5/2}. \quad (64)$$

$$\rho_t(E) = L^{-1}\{K_2'\ s^{-5/2}\}$$

$$= K_2'\ E^{3/2}. \quad (65)$$

$$q_v = b^5\left(\frac{1}{s-m}\right)^5. \quad (66)$$

$$\rho_v(E) = L^{-1}\ \{b^5\left(\frac{1}{s-m}\right)^5\}$$

$$= K_3'\ E^4\ e^{mE}. \quad (67)$$

It is mathematically more convenient to set up the convolution integral as follows for $Fe(CO)_5$

$$\rho_{total}(E) = \int_o^E \rho_v(E-x)\ \rho_t(x)dx \tag{68}$$

$$= \int_o^E K_3'\ (E-x)^4\ e^{m(E-x)}\ K_2'\ x^{3/2}\ dx. \tag{69}$$

Again, expanding $(E-x)^4$ and e^{-mx} and taking e^{mE} out of the integral

$$\rho(E) = K_2'K_3'\ e^{mE}\left[E^4\int_o^E x^{1.5}dx - 4E^3\int_o^E x^{2.5}dx + 6E^2\int_o^E x^{3.5}dx\right.$$
$$- 4E\int_o^E x^{4.5}dx + \int_o^E x^{5.5}dx - mE^4\int_o^E x^{2.5}dx + m4E^3\int_o^E x^{3.5}dx - m6E^2\int_o^E x^{4.5}dx$$
$$+ m4E\int_o^E x^{5.5}dx - m\int_o^E x^{6.5}dx + \frac{m^2E^4}{2}\int_o^E x^{3.5}dx - \frac{m^2 4E^3}{2}\int_o^E x^{4.5}dx$$
$$\left. + \frac{m^2 6E^2}{2}\int_o^E x^{5.5}dx - \frac{m^2 4E}{2}\int_o^E x^{6.5}dx + \frac{m^2}{2}\int_o^E x^{7.5}dx\right]. \tag{70}$$

$$\rho(E) = K_2'K_3'\ e^{mE}\ [1.705\times10^{-2}E^{6.5} - m\cdot5.683\times10^{-3}E^{7.5} + m^2\cdot1.170\times10^{-3}E^{8.5}]. \tag{71}$$

$$\boxed{\rho(E) \propto e^{mE}\ [E^{6.5} - 0.3333\,mE^{7.5} + 0.06862\,m^2E^{8.5}]} \tag{72}$$

$Fe(CO)_5$ Restricted degrees of freedom

With the same values of m used as before, equation (63) is plotted as a function of E_M^* (E_u) as the solid lines in Figs. 28 and 29 for $Ni(CO)_4$. Likewise, equation (72) is plotted in Figs. 30 and 31 for $Fe(CO)_5$ as the solid lines.

Not only is the model of one-dimensionally translating, vibrating, non-rotating exiting CO ligands physically satisfying, but it also agrees quite well with experimentally observed rates of formation of excited metal states. Of all the possible models that restrict the degrees of freedom, this is the only one that reproduces the experimental data and at the same time gives a real, intuitive feel for the metal carbonyl dissociation mechanism.

H. Discussion

The energy balance between the metastable rare gas and the excited metal atom is worth some discussion. As mentioned in the statistical theory section, it takes about 49,000 cm^{-1} to dissociate both $Ni(CO)_4$ and $Fe(CO)_5$ to the free metal atom and carbon monoxide molecules. Considering Ar^* (E = 93144 cm^{-1}) as the energy donor, this leaves 44,000 cm^{-1} as an upper limit to the metal excitation. Examination of the population (Figs. 22 and 25) and rate (Figs. 28 and 30) plots for Ar^* show experimentally observed metal excitations up to about 37,000 cm^{-1}. Metal states are probably excited up to the 44,000 cm^{-1} limit, but with rates too low to be experimentally detected. Considering Ne^* (E = 134,043 cm^{-1}) as the energy donor, metal states up to 85,000 cm^{-1} may be observed. Examination of the population (Figs. 23 and 26) and rate (Figs. 29 and 31) plots for Ne^* show many higher energy excitations not observed with Ar^*. Excitations near the ionization limits of Ni (61579 cm^{-1}) and Fe(63700 cm^{-1}) are experimentally observed, and it is energetically possible that a dissociative ionization process can occur with Ne^* and He^*, e.g.

$$Ne^* + Ni(CO)_4 \rightarrow [Ni(CO)_4]^{\ddagger} \rightarrow Ni^+ + 4CO + e^-.$$

Thus the major difference in the interaction of Ar^*, Ne^* or He^* with a metal carbonyl is simply the amount of energy that it deposits. Higher energy metastable excite higher energy metal atom states.

It is instructive to compare the collisional dissociation results with previous methods for dissociating metal carbonyls. Brennen and Kistiakowsky[49] observed metal atom emission from metal carbonyl–active nitrogen flames. They analyzed their Fe^* and Ni^* data in the same way, comparing populations and rates. Two important differences exist between their results and this work. First, they show that reaction with active nitrogen proceeds via a sequential degradation

$$M(CO)_n + N \rightarrow M(CO)_{n-1} + NCO$$

until the metal atom is liberated. Metal excitation then proceeds according to

$$M + N_2^*(A^3\Sigma) \rightarrow M^* + N_2.$$

Secondly, although the energy of N_2^* is roughly half that of Ar^* (and even less than that of Ne^* or He^*), their metal excitations include high energy states of Fe and Ni which are not observed in the Ar^* flames due to different degradation mechanisms. In common with this work, Brennen and Kistiakowsky found anomalous J-dependent behavior in the emission rates of the low-lying, long-lived states, similar to that discussed previously. They attribute this behavior to collisional relaxation being in significant competition with radiative relaxation. For N_2, the Fe ground state $J = 3$ to $J = 4$ collisional deactivation rate constant[45] is two orders of magnitude greater then for Ar, lending plau-

sibility to their argument. In constrast, our buffer gas was always a rare gas, and we do not populate high energy states with Ar^* which can populate these long-lived states by radiative cascade as was the case for Brennen and Kistiakowsky. As mentioned before, the metal carbonyl itself may cause collisional ΔJ transitions in the metal atoms. Experiments to test this need to be done in the futre.

Metal carbonyls and organometallics have been subjected to low pressure rare gas discharges for the purpose of producing atomic metal vapor lasers.[50,51] The results of our experiments should be of value in understanding the mechanisms producing lasing action in these systems.

Metal carbonyls have been dissociated by flash photolysis[45,52] and by eximer laser photodissociation.[53,54] Of particular interest are the results found by Karny, Naaman and Zare,[54] that KrF 249 nm laser photolysis of $Fe(CO)_5$ produces Fe^* via multiphoton dissociation, two photons being used because of the quadratic dependence on laser power. The J-state distribution is neither uniform nor statistical. At very high rare gas buffer pressures (300 torr), they found J levels not observed from photolysis of low pressure (5 mtorr) pure carbonyl. At higher pressures they actually saw higher energy (lower J) levels of a given term populated, probably caused by collisional activation. Also, they did not see any appreciable high-spin septet excitation of Fe.

What is the nature of the molecular excited state or states from which these molecules dissociate? While any of the metastable rare gases studied here have sufficient energy to ionize the carbonyls (which have ionization potentials[55] of about 8.5 eV), there is no evidence that Penning ionization occurs. If it does occur, it produces products

which do not luminesce, and it is clearly in competition with the favorable collisional dissociation mechanism channel which is observed.

In contrast to the multiphoton photolysis, the metastable transfers all of its very large energy at once. The data appear no sooner than a few tens of nanoseconds later. During this time, dissociation occurs. But is it via a sequential metal-ligand bond rupture, a simultaneous bond rupture, or something in between, such as the rupture of one bond clearly separated in time from the rupture of perhaps a subset of bonds? If has been shown[52,56] that species such as $Fe(CO)_4$ and $Ni(CO)_3$ do exist, and that they can be photochemically produced from excited states of the normal carbonyls which lie fairly low ($\leqslant$ 6 eV) in energy. These excited states are connected to the ground state via optical selection rules which need not be followed by collisional electronic energy exchange processes.

As described before, the energy transfer from a metastable rare gas may be thought of as a two-electron energy exchange process : here the carbonyl donates an electron from a high-energy filled M.O. to the metastable hole (e.g the 3p vacancy in Ar^*), followed by transfer of the excited rare gas electron into an unoccupied M.O. on the carbonyl. If the electron lands in an unbound, continuum M.O. of the carbonyl, Penning ionization results; otherwise the carbonyl is left in a neutral, but highly excited state. To apply this mechanism, the electronic structure of the carbonyl must be considered.

Ab initio calculations[57] have lead to the following description of metal carbonyl bonding. First, let us consider $Ni(CO)_4$. The first conceptual step in the formation of $Ni(CO)_4$ from Ni and CO is the atomic

promotion of Ni to the so-called atomic valence state

$$Ni(a\ ^3F,\ 3d^8 4s^2) \rightarrow Ni(a\ ^1S,\ 3d^{10}),$$

followed by tetrahedral complexation with CO. Free CO has the valence configuration $3\sigma^2\ 4\sigma^2\ 1\pi^4\ 5\sigma^2$. On forming the molecular orbitals of $Ni(CO)_4$, the effects of σ-donation from CO to Ni and π-back-donation from Ni to CO must be considered. From the population analysis of Baerends and Ros (who performed a discrete variational $X\alpha$ calculation which agreed with photoelectron data), one finds the molecular configuration

$$Ni[3d^{8.13}4p^{0.88}](CO[3\sigma^2\ 4\sigma^2\ 1\pi^4\ 5\sigma^{1.84}\ 2\pi^{0.44}])_4$$

where the 4p population of 0.88 is due to 5σ CO donation and the 2π population of 0.44 per ligand is due to Ni 3d back-donation to the previously empty π orbital. The highest occupied M.O.'s of $Ni(CO)_4$ are the $9t_2$ (composed of 3d and 2π orbitals) and 2e (which is 3d in character). Note that Ni is now formally short one electron, and the 4s orbital of Ni is empty).

Now consider a collision with the metastable rare gas. The electron that will ultimately fill the rare gas vacancy will come from the $9t_2$ orbital of $Ni(CO)_4$. This orbital is the highest occupied orbital, and is also spatially the outermost orbital. Whether this electron is 3d or 2π in parentage is irrelevant, since charge will flow back to the metal during dissociation to yield neutral species, i.e., this is what is observed experimentally. The electron transferred from the metastable will land in a metal orbital due to the positive effective charge in Ni.

This orbital could be either the 4s vacancy or the 3d, especially if the $9t_2$ orbital lost 3d character. Whatever its nature, this metal orbital is clearly metal-ligand antibonding, having been empty in the free carbonyl. The result of this electron rearrangement will be to place the carbonyl in a state of high potential energy with the important π back-bonding framework destroyed. The metal-ligand interactions would all become repulsive.

Note that subsequent to dissociation, it is experimentally observed that Ni is left in the $3d^9 4p$ or $3d^8 4s4p$ configurations. These are just the configurations that are predicted from the above discussion. Intraatomic relaxation during dissociation can possibly form the ground-state $3d^8 4s^2$ and low-lying $3d^9 4s$ configurations of Ni by charge flow away from Ni(4p) back to the CO(5σ) orbitals from which it came. The $3d^{10}$ configuration would appear to be of little importance.

Similar arguments can be applied to $Fe(CO)_5$. Population analysis in $Fe(CO)_5$ shows the CO 2π orbitals gaining 2.64 electrons from the $3d^8$ valence state configuration of Fe, while σ donation populates not only the Fe 4p orbital but also the 4s to some extent. The populations in $Fe(CO)_5$ are thus

$$Fe[\,3d^{6.22}\,4s^{0.085}\,4p^{0.71}\,](CO[3\sigma^2\,4\sigma^2\,1\pi^4\,5\sigma^{1.72}\,2\pi^{0.53}])_5.$$

Analogous to $N(CO)_4$, one would expect the $3d^7 4p$ and $3d^6 4s4p$ configurations to be important. The experimental observation that only the $3d^6 4s4p$ configuration is observed to any extent is apparently kinetic in origin, since terms arising from $3d^7 4p$ are considerably higher in

energy than those from $3d^6 4s4p$.

Photochemical excitation is quite different from this picture. The strongly allowed optical transitions[58] of these carbonyls are primarily d to d metal excitations followed at higher energy by charge transfer bands of metal to ligand charge flow. The bands pumped by eximer laser excitation at 249 nm or at 193 nm are d to π^* charge transfer bands. Due to the $3d_{z2}$ orbitals unique role in $Fe(CO)_5$, these excitations will influence the axial carbonyls and lead to $Fe(CO)_4$, as observed. This flow of charge is in the opposite sense from that proposed for the metastable rare gas excitations which effectively transfer charge from the ligands to the metal.

This spin unpairing which is observed is not surprising because the process is in essence a reversal of the carbonyl synthesis, which involves a facile spin pairing. Spin-orbit coupling during dissociation must be strong.

Thus, the two models for dissociation of metal carbonyls by metastable rare gas atoms give predictions that agree well with experiment. The restricted statistical model provides the energy distributions and gives physical insight into the kinematics of the dissociation mechanism. The two electron exchange mechanism does well in predicting the electron configurations observed in the free metal atoms resulting from Ar^*—metal carbonyl collisions.

The results of this work have opened up many possible experiments for the future, particularly in the area of metal atom and cluster chemistry. Here is a way to produce translationally cool metal atoms in a simple flow environment. By adding a third reagent, chemistry of ground

as well as excited metal atoms is possible. An example of this pursuit is the addition of Cl_2 to an $Ar^* + Ni(CO)_4$ flame. A molecular band emission is observed, attributed to the reaction $Ni^* + Cl_2 \rightarrow NiCl^* + Cl$. Our laboratory is currently studying reactions like these, both with the chemiluminescence apparatus and a newly completed quadrupole mass spectrometer apparatus. In addition, it may be possible to easily create and study gas phase metal clusters, using reactions such as

$$He^* + Fe_3(CO)_{12} \rightarrow He + Fe_3 + 12\,CO.$$

These possibilities are also being investigated in our laboratory.

Also, molecular beam scattering experiments between metal carbonyls and metastable rare gas atoms would be beneficial, helping to determine the interaction potentials and dissociation kinematics involved.

Finally, this work may hopefully encourage more ab initio studies of metal carbonyls, particularly lacking are calculations of highly excited states in the 9-20 eV metastable energy range.

I. Conclusions

The conclusions that can be drawn from the studies of collisional dissociation of metal carbonyls by metastable rare gases can be summarized as follows.

(1) The atomic emissions are due to a single bimolecular energy transfer.

(2) The atomic spectra are quite different from the arc. High-spin states are highly excited, as evidenced by the observation of previously unobserved Ni lines.

(3) The metal atoms formed are not electronically equilibrated.

(4) A statistical model, in which all the CO ligands leave the metal atom radially, gives good agreement with experimental data. This suggests that energy is easily randomized in the energized carbonyl molecule.

(5) M.O. arguments with a two-electron exchange mechanism give a plausible explanation for formation of repulsive excited states.

(6) Differences in photolysis and collisional dissociation are observed and expected. Greater high-spin excitation in collisional dissociation is not surprising, due to the triplet character of the metastable rare gas in comparison to the spinless photon.

(7) A method is available for generation of ground and excited state metal gas atoms and clusters in simple environments. A wealth of new information on gas phase transition metal chemistry should become available in the future.

REFERENCES

1. (a) A. Fontijn, Prog. React. Kinet. 6, 75 (1971); (b) Pure Appl. Chem. 39, 287 (1974).

2. D. H. Stedman and D. W. Setser, Prog. React. Kinet. 6, 193 (1972).

3. R. M. St. John, in "Methods of Experimental Physics", L. Marton, ed., Academic Press (1969) p. 27.

4. G. A. Rutgers and J. C. DeVos, Physica 20, 715 (1954).

5. (a) P. D. Foote and F. L. Mohler, Phys. Rev. 26, 195 (1925); (b) F. L. Mohler, P. D. Foote and R. L. Chenault, Phys. Rev. 27, 37 (1926).

6. J. Franck, as quoted in B. Gudden, "Lichtelektrische Erscheinungen", Chap. 14, p. 226, Julius Springer, Berlin (1928).

7. F. L. Arnot and J. C. Milligan, Proc. Roy. Soc. (London) A153, 359 (1936).

8. J. A. Hornbeck and J. P. Molnar, Phys. Rev. 84, 621 (1951)

9. A. A. Kruithof and F. M. Penning, Physica 4, 430 (1937).

10. (a) W. J. Miller, Oxidation and Combustion Reviews 3, 97 (1968); (b) H. F. Calcote and W. J. Miller, "Chemical Reactions under Plasma Conditions" M. Venugopalan, ed., Interscience, N. Y. (1971); (c) H. F. Calcote, "AGARD Conference Proceedings", No. 8, p. 1. Technical Editing and Reproduction, Ltd., London (1965).

11. W. L. Fite and P. Irving, J. Chem. Phys. 56, 4227 (1972).

12. H. Haberland, Y. T. Lee and P. E. Siska, Lawrence Berkeley Laboratory Report LBL-8959 and also to be published as a chapter in "The Excited State in Chemical Physics, Part 2", J. Wm. McGowan, ed., Wiley-Interscience, N. Y.

13. A. Niehaus, Ber. Bunsenges Phys. Chem. 77, 632 (1973).

14. W. H. Miller, Chem. Phys. Lett. 4, 627 (1970).

15. J. C. Bellum and T. F. George, J. Chem. Phys. 68, 134 (1978).

16. A. P. Hickman, A. D. Isaacson and W. H. Miller, J. Chem. Phys. 66, 1483 (1977).

17. W. H. Miller, C. A. Slocomb and H. F. Schaefer III, J. Chem. Phys. 56, 1347 (1972).

18. W. H. Miller, J. Chem. Phys. 52, 3563 (1970).

19. (a) H. Totop and A. Niehaus, Z. Physik 215, 395 (1968);
(b) H. Hotop and A. Niehaus, Z. Physik 228, 68 (1969);
(c) H. Totop and A. Niehaus, Z. Physik 238, 452 (1970);
(d) V. Fuchs and A. Niehaus, Phys. Rev. Lett. 21, 1136 (1968).

20. (a) V. Čermák, Collect. czechoslov. chem. Commun. 33, 2739 (1968); (b) V. Čermák and Z. Herman, Chem. Phys. Lett. 2, 359 (1968).

21. C. E. Moore, Natl. Stand. Ref. Data Ser. Natl. Bur. Stand. 35 (1971).

22. A. Dalgarno and A. E. Kingston, Proc. Roy. Soc. (London) A259, 424 (1961). This work contains the polarizabilities of all the rare gases.

23. (a) K. V. Subbaram, J. A. Coxon and W. E. Jones, Can. J. Phys. 54, 1535 (1976). (b) J. A. Coxon, W. E. Jones and K. V. Subbaram, Can. J. Phys. 55, 254 (1977).

24. J. H. Goble, D. C. Hartman and J. S. Winn, J. Chem. Phys. 66, 363 (1977).

25. J. H. Goble, D. C. Hartman and J. S. Winn, J. Chem. Phys. 67, 4206 (1977).

26. K. P. Huber and G. H. Herzberg, "Constants of Diatomic Molecules" Van Nostrand (1979).

27. W. L. Wiese, M. W. Smith and B. M. Miles, Natl. Bur. Stand. U. S. Circ. 22 (1969).

28. L. A. Riseberg, W. F. Parks and L. D. Schearer, Phys. Rev. A 8, 1962 (1973).

29. Z. Herman and V. Čermák, Nature 199, 588 (1963).

30. H. Totop and A. Niehaus, Chem. Phys. Lett. 8, 497 (1971).

31. T. Ebding and A. Niehaus, Z. Phys. 270, 43 (1974).

32. H. Morgner, Doktorarbeit, Universitat Freiburg (1976).

33. J. Krenos and J. Kobovitch, private communication.

34. W. F. Meggers, C. H. Corliss and B. F. Scribner, Natl. Bur. Stand. U. S. Monogr. 32, Part 1 (1961).

35. (a) A. N. Zaidel', V. K. Prokof'ev, S. M. Raiskii, V. A. Slavnyi and E. Ya. Schreider, "Tables of Spectral Lines", IFI/Plenum (1970); (b) M.I.T. Wavelength Tables, Technology Press (Cambridge Mass.) (1939); (c) Bibliography on Atomic Transition Probabilities (1914 through Oct. 1977) NBS Special Publication 505. References for Ni therein.

36. R. Mavrodineanu and H. Boiteux, "Flame Spectroscopy", John Wiley (1965) p. 515.

37. J. R. Fuhr, private communication.

38. (a) D. E. Blackwell, P. A. Ibbetson, A. D. Petford and R. B. Willis, Mon. Not. R. Astron Soc. 177, 219 (1976); (b) D. E. Blackwell, P. A. Ibbetson, A. D. Petford and M. J. Shallis, Mon. Not. R. Astron. Soc. 186, 633 (1979). (c) D. E. Blackwell, A. D. Petford and M. J. Shallis, Mon. Not. R. Astron. Soc. 186, 657 (1979).

39. J. M. Bridges and R. L. Kornblith, Astrophys. J. 192, 793 (1974).

40. M. May, J. Richter and J. Wichelmann, Astron. Astrophys. Suppl. Ser. 18, 405 (1974).

41. C. H. Corliss and J. L. Tech, Nat. Bur. Stand. (U.S.) Monogr. 108 (1968).

42. C. H. Corliss and J. L. Tech, J. Res. Nat. Bur. Stand. (U.S.) 80A, 787 (1976).

43. C. H. Corliss, J. Res. Nat. Bur. Stand.(U.S.) 69A, 87 (1965).

44. If I were measured in units of power (photon counts/sec multiplied by $h\nu$), then one would plot log $(I\lambda^3/gf)$.

45. A. B. Callear and R. J. Oldman, Trans. Faraday Soc. 63, 2888 (1967).

46. W. Forst, Chem. Rev. 71, 339 (1971).

47. A. K. Fischer, F. A. Cotton and G. Wilkinson, J. Am. Chem. Soc. 79, 2044 (1957).

48. F. A. Cotton, A. K. Fischer and G. Wilkinson, J. Am. Chem. Soc. 81, 800 (1959).

49. W. R. Brennen and G. B. Kistiakowsky, J. Chem. Phys. 44, 2695 (1966).

50. D. W. Trainer and S. A. Mani, J. Chem. Phys. 68, 5481 (1978).

51. M. S. Chou and T. A. Cool, J. Appl. Phys. 47, 1055 (1976).

52. A. B. Callear, Proc. Roy. Soc. A265, 71, 88 (1961).

53. D. W. Trainer and S. A. Mani, Appl. Phys. Letters 33, 31 (1978).

54. Z. Karny, R. Naaman and R. N. Zare, Chem. Phys. Lett. 59, 33 (1978).

55. R. E. Winters and R. W. Kiser, Inorg. Chem. 3, 699 (1964).

56. M. Poliakoff and J. J. Turner, J. Chem. Soc. Faraday II. 70, 93 (1974).

57. E. J. Baerends and P. Ros, Molec. Phys. 30, 1735 (1975) and references therein.

58. M. Dartiguenave, Y. Dartiguenave and H. B. Gray, Bull. Soc. Chim. 12, 4223 (1969).

59. V. V. Ivanov, "Transfer of Radiation in Spectral Lines", U. S. Natl. Bur. Stand. special Publication 385 (1973) p. 27.

60. L. A. Gundel, D. W. Setser, M.A.A. Clyne, J. A. Coxon and W. Nip, J. Chem. Phys. 64, 4390 (1976).

APPENDIX A

Atomic Absorption Measurements

Atomic absorption has been used to determine the number density of $Ar^*(^3P_2$ and $^3P_o)$ atoms and $Ca(^1S_o)$ atoms. An outline of the relations used follows.

The absorption coefficient for a Doppler line shape is given by

$$K_{ik}(\nu) = \frac{c^2}{8\pi^{3/2}\,\nu_{ik}^2}\,\frac{g_k}{g_i}\,\frac{A_{ki}}{\Delta\nu_D}\,e^{-x^2} \qquad (1)$$

where $K_{ik}(\nu)$ is in cm^2, C is the speed of light, ν_{ik} is the line center frequency of the transition from lower state i to upper state k in sec^{-1}, g_i is the degeneracy of the lower state, g_k is the degeneracy of the upper state, A_{ki} is the Einstein coefficient for spontaneous emission in sec^{-1}, $x = (\nu - \nu_{ik})/\Delta\nu_D$ and $\Delta\nu_D$ is the Doppler width of the line (half-width at half max).

The Doppler half-width at half maximum for a Maxwellian gas is given by

$$\Delta\nu_D = \frac{\nu_o}{c}\sqrt{\frac{2kT\ln 2}{m}}\,. \qquad (2)$$

Substituting all the constants and converting m to atomic (or molecular) weight yields

$$\Delta\nu_D = 3.58115 \times 10^{-7}\sqrt{\frac{T}{M}}\,\nu_o \qquad (3)$$

where T is measured in K and M in g/mole.

As discussed by Ivanov,[59] for gases at moderate to low pressures and near or above room temperature, the Doppler profile of equation (1) is the representation of the line shape particularly around the central part of the line. It is valid if the quantity $(\Delta\nu_R + \Delta\nu_C)/\Delta\nu_D$ is small, where $\Delta\nu_C$ is the collisional linewidth (small at moderate pressures) and $\Delta\nu_R$ is the natural line width given by

$$\Delta\nu_R \doteq A_{ki}/4\pi \qquad (4)$$

where $\Delta\nu_R$ is the half-width at half maximum in sec^{-1}.

The Doppler absorption coefficients at the line center $(\nu-\nu_{ik})$ can now be calculated for $Ca(^1S_o)$ atoms and $Ar^*(^3P_2)$ atoms.

(i) Absorption of the 4226.73 Å resonance line by ground state ^1S_o Ca atoms.

The relevant data[27] are:

Transition : $^1S \rightarrow {}^1P^o$

$E_i = 0\ cm^{-1}$ $\quad E_k = 23652\ cm^{-1}$

$g_i = 1$ $\quad g_k = 3$

$A_{ki} = 2.18 \times 10^8\ sec^{-1}$

$\nu_{ik} = 23652\ cm^{-1} = 7.10 \times 10^{14}\ sec^{-1}$

$\Delta\nu_D\ (298°K) = 2.31 \times 10^{-2}\ cm^{-1} = 6.93 \times 10^8\ sec^{-1}$

$\Delta\nu_R \doteq 2.18 \times 10^8/4\pi \doteq 1.73 \times 10^7\ sec^{-1}$

Substituting into equation (1) with x = 0 yields the absorption coefficient at the line-center

$$\boxed{\begin{array}{l} K_{ik}\ (\nu = \nu_{ik}) = 3.78 \times 10^{-11}\ cm^2 \\ \text{Ca } 4226.73\ \text{Å line} \end{array}} \qquad (5)$$

(ii) Absorption of the 8115.31 Å line by $Ar^*(^3P_2)$ atoms

The relevant data[27] are:

Transition: $4s\,[\frac{3}{2}]^o \rightarrow 4p\,[\frac{5}{2}]$ (jℓ-coupling notation)

$E_i = 93144\ cm^{-1}$ $\quad E_k = 105463\ cm^{-1}$

$g_i = 5$ $\quad g_k = 7$

$A_{ki} = 3.66 \times 10^7\ sec^{-1}$

$\nu_{ik} = 12319\ cm^{-1} = 3.70 \times 10^{14}\ sec^{-1}$

$\Delta\nu_D(298°K) = 1.20 \times 10^{-2}\ cm^{-1} = 3.60 \times 10^8\ sec^{-1}$

$\Delta\nu_R \doteq 3.66 \times 10^7/4\pi \doteq 2.91 \times 10^6\ sec^{-1}$

Substituting into equation (1)

$$\boxed{\begin{array}{l} K_{ik}\ (\nu = \nu_{ik}) = 2.10 \times 10^{-11}\ cm^2 \\ \text{Ar } 8115.31\ \text{Å line} \end{array}} \qquad (6)$$

The number density of the absorbing atom can be calculated using the Beer's law relationship

$$\ln\left(\frac{I_o}{I}\right) = K_{ik} \cdot n_i \cdot x_i \qquad (7)$$

where I_o is the transmitted lamp intensity at ν_{ik} with no absorbing species present, I is the transmitted lamp intensity at ν_{ik} with the absorbing species present, x_i is the path length of absorption in cm and n_i is the number density of the absorbing species in cm^{-3}.

For Ca absorption, a calcium hollow cathode lamp (Hamamatsu) which strongly emitted the 4226.73 Å resonance line was used. For Ar^* absorption, an argon discharge lamp (Oriel) was used, with a strong 8115.31 Å emission. The lamp linewidths, measured with the monochromator, are about 0.05 Å; this value being an upper bound to the true linewidth.

APPENDIX B

Ar^* Rate Constant Measurements

A method[60] for obtaining absolute thermal rate constants for the reactions with $Ar^*(^3P_2)$ will be outlined below. It involves measuring the intensity of the 7602 Å Kr line and comparing it to the intensity for the reaction of interest.

For the following reaction

$$Ar^*(^3P_2) + Kr(^1S_o) \rightarrow Kr^*(5p[\tfrac{3}{2}]_{2,1}) + Ar(^1S_o)$$

the total quenching rate constant has been measured to be 6.2×10^{-12} $cm^3/molec \cdot sec$, with the branching ratios being 88% $5p[\frac{3}{2}]_2$ and 12% $5p[\frac{3}{2}]_1$.

The experimentally monitored 7602 Å line radiates from the $5p[\frac{3}{2}]_2$ level. The 8190 Å Kr line also radiates from this level, and the branching ratio for emission of the 7602 Å line ($\frac{A_{7602}}{A_{7602}+A_{8190}}$, where A is the Einstein coefficient for spontaneous emission) is measured to be 0.765. Therefore

$$\text{Int. Kr 7602 Å line} = Q \times 0.765 \times 0.88 \times 6.2\times10^{-12}[Kr][Ar^*, {}^3P_2]$$
$$= Q \times 4.2\times10^{-12}[Kr][Ar^*, {}^3P_2] \qquad (1)$$

where Q is a constant that reflects the fact that the spectrometer slit samples only a small fraction of the total emission.

For a reaction of species X with $Ar^*(^3P_2)$ in which the unknown rate constant is k_x, it is true that

$$\text{Int. X} = Q(\frac{A}{\Sigma A})\, k_x[X][Ar^*, {}^3P_2] \qquad (2)$$

where $\frac{A}{\Sigma A}$ corrects the emission because of radiative branching.

If one measures the reactions Ar^* + Kr and Ar^* + X under identical conditions with $[Ar^*]$ constant, the same flow rates etc., then one is justified in dividing equation (2) by (1), yielding the following

$$k_x = \left(\frac{\text{Int. X}}{\text{Int. Kr 7602 Å}}\right)\left(\frac{\Sigma A}{A}\right)\left(\frac{[Kr]}{[X]}\right) \times 4.2\times10^{-12} \quad \frac{cm^3}{molec\cdot sec} \qquad (3)$$

where the intensities are of course corrected for spectrometer response. Equation (3) provides an easy way to measure absolute thermal rate constants for reactions with Ar^* ($^3P_2$) atoms.

ACKNOWLEDGMENTS

I would like to thank the University of California at Berkeley campus, its faculty and resources making it an institution of excellence for graduate study. Thanks to the community of Berkeley, a unique city that provided me with lots of entertainment. I will truly miss the Berkeley campus and the surrounding city.

Thanks to Professor John Winn, with an unbelievable mastery of almost every aspect of chemical physics, for his helpful guidance and stimulating research projects. Also for his patience when baby-sitting duties frequently kept me away from the laboratory.

Thanks to my fellow group members Brian, Dave, Henry, Jim, Sue and Will, whose jokes and humor made working in the lab fun. Thanks to Mr. George Weber, an excellent machinist who was always willing to help when I had a problem. Thanks to Dr. Jeffrey Fuhr for his help in obtaining oscillator strengths and Mr. Wesley Natzle for his preliminary calculations of the statistical model. Thanks to Professor Mahan's group for their generous loan of equipment.

Thanks to the two joys in my life, my wife Beth and my son Daniel, for their patience when I was working, reading or studying. I dedicate this thesis to my wife, Beth, who worked as hard as I did over the past four years. She gave me constant moral support when things weren't going well. When I made exciting discoveries in the

lab, she showed much interest and enthusiasm. While I was doing something I really enjoy, science, she was working hard at a job she disliked to supplement my meager income. I would like to tell her how much I appreciate her sacrifice.

This work was supported by the U. S. Department of Energy under contract W-7405-ENG-48.

Table I. The energies of the metastable rare gases.

Atom	L - S Term	Energy(cm^{-1})	Energy(eV)
He	$2\ ^1S$	166272	20.6
	$2\ ^3S$	159850	19.8
Ne	^3P_o	134820	16.7
	$^3P_2$	134043	16.6
Ar	^3P_o	94554	11.7
	$^3P_2$	93144	11.5
Kr	^3P_o	85192	10.5
	$^3P_2$	79973	9.9
Xe	^3P_o	76197	9.4
	$^3P_2$	67086	8.3

Table II. The most common reactions with metastable rare gas atoms, A^*.

Reaction	Classification
$A^* + B \rightarrow A + B^+ \text{ (or } B^{+*}) + e^-$	Penning Ionization
$A^* + B \rightarrow BA^+ \text{ (or } BA^{+*}) + e^-$	Associative Ionization
$A^* + B \rightarrow A + B^*$	Neutral Excitation
$A^* + B \rightarrow A + B' + B''$	Neutral Dissociation
$A^* + B \rightarrow A + B'^* + B''$	Excitive Neutral Dissociation

Table III. The energies[a] of species in the Ca + Ar^* system.

Species	Energy(cm^{-1})
Ca^+ (^2S)	101,473
Ar^* ($^3P_2$)	93,144
Ca^+ ($^2P^o_{3/2}$)	74,720
Ca^+ ($^2P^o_{1/2}$)	74,498
Ca^+ ($^2D_{5/2}$)	63,017
Ca^+($^2D_{3/2}$)	62,956
Ca^+(^2S)	49,306
Ca (^1S_o)	0
Ar(^1S_o)	0

a) relative to the ground state neutral atom. Values taken from Ref. 21.

Table IV. The spectral constants[a] for $BeAr^+$.

	$X^2\Sigma^+$	$A^2\Pi_r$
T_e	0	24576.5
ω_e	362.7	583.2[b]
$\omega_e x_e$	8.92	6.70[b]
$\omega_e y_e$	0.033	---
A_e	---	42.68
B_e	0.5271	0.6124
α_e	0.0145	0.0089
$10^5\gamma_e$	6.5	---
r_e(Å)	2.0855	1.9348
D_e(Thakkar)	4536	11,888
D_e(Ref. 23)	4112	11,464

a) Values in wavenumbers (cm^{-1}) from Ref. 23.

b) Value corrected from a calculation error in Ref. 23.

Table V. Observed frequencies in the CaAr $^{+2}\Pi \rightarrow {}^{2}\Sigma^{+}$ spectrum.

Vacuum wavenumber	Comment	
22562 ± 60	Strongest continuum band	
23792 ± 40	Continuum band	
24044 ± 10	Continuum band	
24226 ± 6	Continuum band	
24543 ± 3	Bound	Stronger bands
24598 ± 3	Bound	
24650 ± 3	Bound	
24695 ± 3	Bound	
24748 ± 3	Bound	
24800 ± 6	Bound	
24853 ± 6	Bound	
24886 ± 6	Bound	
24929 ± 6	Bound	
24973 ± 6	Bound	

Table VI. Observed and calculated[a] frequencies[b] for $CaAr^+$.

Observed	Calculated v' = 28	Calculated v' = 29	Calculated v' = 30	Calculated v' = 31	Type of Transition
22562 ± 60	22560	22625	22680	22720	Strongest continuum band
23792 ± 40	23750	23820	23880	23950	Continuum
24044 ± 10	24130	24100	24160	24230	Continuum
24226 ± 6					Continuum
24543 ± 3	24546	---	---	---	Bound
24598 ± 3	---	24600	---	---	Bound
24650 ± 3	---	---	24652	---	Bound
24695 ± 3	---	---	---	24701	Bound

a) Model potential parameters Z, ω_e, r_e for $X^2\Sigma^+$ = 1, 87, 2.8 and for $A\ ^2\Pi_{3/2}$ = 2, 200, 2.6.

b) Frequencies in vacuum wavenumbers.

Table VII. Assigned transitions and relative intensities of the major Fe lines from a pure Fe arc spectrum and the Ar^* + $Fe(CO)_5$ flame spectrum.

Upper State Configuration	Transition	I_{arc} [a]	I_{flame} [b]
$3d^6 4s^1 4p^1$	$z^7F^\circ_5 \rightarrow a^5D_4$	0.009	1.00
	$z^7D^\circ_4 \rightarrow a^5D_4$	0.003	0.63
	$z^5F^\circ_5 \rightarrow a^5D_4$	0.86	0.51
	$z^7F^\circ_4 \rightarrow a^5D_3$	0.009	0.44
	$z^7P^\circ_4 \rightarrow a^5D_4$	0.002	0.44
	$z^7D^\circ_5 \rightarrow a^5D_4$	<0.001	0.44
	$z^5D^\circ_4 \rightarrow a^5D_4$	0.60	0.36
	$z^5F^\circ_4 \rightarrow a^5D_3$	0.49	0.34
	$z^5F^\circ_3 \rightarrow z^5D_2$	0.34	0.34
	$z^5D^\circ_3 \rightarrow a^5D_3$	0.26	0.33
	$z^5D^\circ_3 \rightarrow a^5D_4$	0.57	0.14
$3d^7 4p^1$	$y^3F^\circ_4 \rightarrow a^3D_4$	0.43	0.014
	$z^5G^\circ_6 \rightarrow a^5F_5$	0.86	0.009
	$y^5D^\circ_4 \rightarrow a^5F_5$	0.71	0.009
	$y^5F^\circ_5 \rightarrow a^5F_5$	1.00	<0.002
	$y^5F^\circ_4 \rightarrow a^5F_4$	0.57	<0.002
	$y^5D^\circ_3 \rightarrow a^5F_4$	0.46	<0.002

[a] Intensities relative to strongest arc line at 3734.87 Å.

[b] Intensities relative to strongest flame line at 4375.93 Å.

Table VIII. Assigned transitions and relative intensities of the major Ni lines from a pure Ni arc spectrum and the Ar^* + $Ni(CO)_4$ flame spectrum.

Upper State Configuration	Transition	I_{arc} [a]	I_{flame} [b]
$3d^8 4s^1 4p^1$	$z^5D^\circ_4 \rightarrow a^3F_4$	<0.001	1.00
	$z^5G^\circ_5 \rightarrow a^3F_4$	0.016	0.88
	$z^5D^\circ_3 \rightarrow a^3F_4$	<0.001	0.70
	$z^5D^\circ_4 \rightarrow a^3D_3$	<0.001	0.58
	$z^5F^\circ_4 \rightarrow a^3D_3$	0.61	0.47
	$z^5D^\circ_3 \rightarrow a^3D_3$	<0.001	0.44
	$z^3G^\circ_5 \rightarrow a^3F_4$	0.13	0.19
	$z^5F^\circ_3 \rightarrow a^3D_2$	0.16	0.15
	$z^5G^\circ_4 \rightarrow a^3D_3$	0.016	0.14
	$y^3F^\circ_4 \rightarrow a^3D_3$	0.37	0.12
	$y^3D^\circ_3 \rightarrow a^3D_3$	0.43	0.08
	$y^1D^\circ_2 \rightarrow a^1D_2$	0.40	0.014
$3d^9 4p^1$	$z^3P^\circ_2 \rightarrow a^3D_3$	1.00	0.62
	$z^3F^\circ_4 \rightarrow a^3D_3$	1.00	0.40
	$z^3F^\circ_3 \rightarrow a^3D_2$	0.80	0.27
	$z^1F^\circ_3 \rightarrow a^1D_2$	0.80	0.24
	$z^1D^\circ_2 \rightarrow a^1D_1$	0.61	0.20
	$z^3D^\circ_2 \rightarrow a^2D_3$	0.59	0.18
	$z^3D^\circ_3 \rightarrow a^3D_3$	0.40	0.16
	$z^3P^\circ_1 \rightarrow a^3D_2$	0.67	0.13
	$z^1P^\circ_1 \rightarrow a^1D_2$	0.40	0.08
	$z^3F_2 \rightarrow a^3D_1$	0.61	<0.001

[a] Intensities relative to strongest arc lines at 3414.76 and 3524.54 Å.

[b] Intensities relative to strongest flame line at 3881.86 Å.

Table IX. Previously unreported Ni emission lines.

λ_{air}(Å)	Transition	log(gf)	$A_{ul}(sec^{-1})$
3876.97	$z^5D°_3 \rightarrow a^3D_2$	-4.70[a]	1.3×10^3
		-4.51[b]	2.0×10^3
3881.86	$z^5D°_4 \rightarrow a^3F_4$	-4.13[a]	3.6×10^3
		-4.19[b]	3.2×10^3
		-4.22[c]	3.0×10^3
4093.62	$z^5D°_4 \rightarrow a^3F_3$	-5.92[a]	5.3×10^2

[a] Value from Ar^* flame.
[b] Value from Ne^* flame.
[c] Value from He^* flame.

Table X. Comparison of intensities between this work and the preliminary molecular beam study of the reaction $Ar^* + Fe(CO)_5$.

λ (Å)	Transition	Corrected Intensities[a]	
		This Work	Kobovitch & Krenos
4375.9	$^7F^\circ_5 \rightarrow {}^5D_4$	4699	1260
4427.3	$^7F^\circ_4 \rightarrow {}^5D_3$	2088	1069
4461.7	$^7F^\circ_3 \rightarrow {}^5D_2$	805	677
4482.2	$^7F^\circ_2 \rightarrow {}^5D_1$	306	375

a) A set of $^5F^\circ \rightarrow {}^5D$ transitions was normalized to be equal in intensity to this works data. In general, Kobovitch and Krenos quintet intensities are comparable, but septet intensities are weaker. See text for an explanation.

Table XI. Rate constants for formation of excited Fe states from the reaction $Ar^* + Fe(CO)_5$.

State	J	E_u	k (cm^3 $molecule^{-1}$ sec^{-1})
$z\,^7D°$	5	19351	3.8×10^{-13}
	4	19562	4.8×10^{-13}
	3	19757	2.6×10^{-13}
	2	19913	4.2×10^{-14}
	1	20020	2.4×10^{-14}
$z\,^7F°$	6	22650	---
	5	22846	7.5×10^{-13}
	4	22997	3.4×10^{-13}
	3	23111	1.3×10^{-13}
	2	23193	5.7×10^{-14}
	1	23245	1.9×10^{-14}
	0	23270	---
$z\,^7P°$	4	23711	4.0×10^{-13}
	3	24181	2.2×10^{-13}
	2	24506	6.1×10^{-14}
$z\,^5D°$	4	25900	3.7×10^{-13}
	3	26140	4.6×10^{-13}
	2	26340	3.0×10^{-13}
	1	26479	2.3×10^{-13}
	0	26550	5.0×10^{-14}

Table XI. (continued)

State	J	E_u	k (cm^3 $molecule^{-1}$ sec^{-1})
$z\ ^5F°$	5	26875	---
	4	26167	2.5×10^{-13}
	3	27395	2.6×10^{-13}
	2	27560	---
	1	27666	1.4×10^{-13}
$z\ ^5P°$	3	29056	2.3×10^{-13}
	2	29469	1.0×10^{-13}
	1	29733	2.6×10^{-14}
$z\ ^5G°$	6	34844	---
	5	34782	1.4×10^{-14}
	4	35257	6.8×10^{-15}
	3	35612	7.6×10^{-15}
	2	35856	4.7×10^{-15}

Table XII. Density of states per 2500 cm^{-1} for CO X $^1\Sigma^+$.

v	E	E_M	$\rho_v(E)$	v	E	E_M	$\rho_v(E)$
0	0	1071.7	1.166	31	54466.8	55145.8	1.841
1	2143.3	3201.7	1.181	32	55824.8	56491.7	1.874
2	4260.0	5305.2	1.196	33	57158.5	57813.4	1.909
3	6350.4	7382.5	1.211	34	58468.2	59111.0	1.945
4	8414.5	9433.4	1.227	35	59753.7	60384.4	1.982
5	10452.2	11458.0	1.243	36	61015.1	61633.8	2.021
6	12463.8	13456.5	1.259	37	62252.4	62859.0	2.061
7	14449.2	15428.9	1.276	38	63465.6	64060.2	2.102
8	16408.5	17375.2	1.293	39	64654.7	65237.3	2.146
9	18341.9	19295.7	1.311	40	65819.8	66390.3	2.191
10	20249.4	21190.2	1.329	41	66960.7	57519.1	2.239
11	22131.0	23054.0	1.340	42	68077.4	68623.6	2.289
12	23986.9	24902.0	1.366	43	69169.8	69703.9	2.341
13	25817.1	26719.4	1.385	44	70237.9	70759.8	2.395
14	27621.7	28511.3	1.405	45	71281.7	71791.3	2.453
15	29400.9	30277.8	1.426	46	72300.9	72798.2	2.514
16	31154.6	32018.8	1.446	47	73295.5	73780.5	2.578
17	32883.0	33734.6	1.468	48	74265.4	74737.9	2.646
18	34586.2	34425.2	1.490	49	75210.3	75670.3	2.718
19	36264.2	37090.7	1.512	50	76130.2	76577.5	2.795
20	37917.1	38731.1	1.536	51	77024.8	77459.4	2.877
21	39545.0	40346.5	1.560	52	77893.9	78315.6	2.965
22	41148.0	41937.1	1.584	53	78737.2	79145.9	3.058
23	42726.2	43502.9	1.609	54	79554.6	79950.1	3.161
24	44279.6	45044.0	1.635	55	80345.6	80727.8	3.271
25	45808.4	46560.5	1.662	56	81110.0	81478.8	3.390
26	47312.5	48052.4	1.690	57	81847.5	82202.6	3.520
27	48792.2	49519.8	1.718	58	82557.7	82898.9	3.664
28	50247.4	50962.8	1.747	59	83240.1	83567.3	3.821
29	51678.2	52381.4	1.778	60	83894.4		
30	53084.6	53775.7	1.809				

Table XIII. Least squares fits of the numerical vibrational density of states of CO $X\,^1\Sigma^+$ to the function be^{mE}.

Maximum CO vibrational energy	Least squares parameters[a]
50,000 cm^{-1}	b = 1.133
	$m = 7.941 \times 10^{-6}$
	R = 0.9957
60,000 cm^{-1}	b = 1.117
	$m = 8.698 \times 10^{-6}$
	R = 0.9927
83,000 cm^{-1}	b = 0.9894
	$m = 1.303 \times 10^{-5}$
	R = 0.9599

a) R is the correlation coefficient for the least squares fit.

TECHNICAL INFORMATION DEPARTMENT
LAWRENCE BERKELEY LABORATORY
UNIVERSITY OF CALIFORNIA
BERKELEY, CALIFORNIA 94720